

UNIVERSITY OF CALIFORNIA

Los Angeles

The Compression of the Geo-Magnetosphere:

A Physical Model

and the Effects of Compression

A dissertation submitted in partial satisfaction of the

Requirements for the degree

Doctor of Philosophy

in Geophysics and Space Physics

by

Galen James Fowler

2005

The dissertation of Galen James Fowler is approved.

---

Larry R. Lyons

---

Mark B. Moldwin

---

Robert J. Strangeway

---

Chris T. Russell, Committee Chair

University of California, Los Angeles

2005

This dissertation is dedicated to my family and many loyal friends.

# TABLE OF CONTENTS

<b>List of Figures</b>	viii
<b>List of Tables</b>	xi
<b>Acknowledgements</b>	xii
<b>VITA</b>	xiii
<b>Publications and Presentations</b>	xiii
<b>ABSTRACT OF THE DISSERTATION</b>	xiv
<b>Chapter 1. Introduction</b>	1
Section 1.1. Background	1
Section 1.2. Data and Instrumentation	11
Section 1.3. Models	15
Section 1.4. Synopsis of thesis	17
Section 1.5. References	21
<b>Chapter 2. SI Predictions by Models</b>	25
Section 2.1. Introduction	25
Section 2.1.1. Description of the T89 Model	28
Section 2.1.2. Description of the T96 Model	29
Section 2.1.3. Description of the T01 Model	32
Section 2.1.4. Description of the MHD Model	34
Section 2.2. Standardized Compression	35
Section 2.2.1. Results from the T89 Model	36

Section 2.2.2. Results from the T96 Model .....	38
Section 2.2.3. Results from the T01 Model .....	40
Section 2.2.4. Standardized compression with MHD Model.....	43
Section 2.2.5. Summary of Results .....	45
Section 2.3. Varying Other Input Parameters .....	45
Section 2.4. Summary and Conclusions .....	49
Section 2.5. References .....	52
<b>Chapter 3. Comparison of Observations to Models .....</b>	<b>55</b>
Section 3.1. Introduction .....	55
Section 3.2. Qualitative Verification of the Standardized Compression .....	56
Section 3.3. Statistical Analysis of Observations and Model Predictions .....	62
Section 3.3.1. Statistical Results .....	63
Section 3.3.2. Discussion of Numerical Results .....	67
Section 3.4. Modifications to the T96 Model .....	69
Section 3.4.1. Statistical Results .....	71
Section 3.4.2. Discussion of Numerical Results .....	74
Section 3.5. Response Ratios.....	77
Section 3.6. Summary and Conclusions .....	82
Section 3.7. References .....	85
<b>Chapter 4. Analysis of SI Rise Times .....</b>	<b>87</b>
Section 4.1. Introduction .....	87
Section 4.2. Rise Times and Shock Speed .....	89

Section 4.2.1. Case Study: October 12, 2000	91
Section 4.2.2. Case Study: September 28, 1996	93
Section 4.2.3. Summary	96
Section 4.3. Geoeffective Length	97
Section 4.4. Summary and Conclusions	100
Section 4.5. References	102
<b>Chapter 5. ULF Wave Activity due to Magnetospheric Compression</b>	<b>103</b>
Section 5.1. Introduction	103
Section 5.2. Observations and Results	107
Section 5.2.1. Case Study: November 22, 1997	108
Section 5.2.2. Case Study: November 7, 1998	110
Section 5.2.3. Case Study: August 6, 1998	113
Section 5.2.4. Case Study: January 27, 2000	115
Section 5.2.5. Statistics of the Data Set	117
Section 5.3. Occurrence Rate	119
Section 5.4. Summary and Conclusions	123
Section 5.5. References	125
<b>Chapter 6. Summary and Conclusions</b>	<b>127</b>
Section 6.1. Summary	128
Section 6.1.1. Proposing the Potential Physical Models	128
Section 6.1.2. Choosing a Physical Model via Statistical Analysis	129
Section 6.1.3. SI Rise Time Dependence	131

Section 6.1.4. Energizing the Inner Magnetosphere .....	132
Section 6.2. Conclusions .....	133
Section 6.3. Recommendations for Future Work .....	134
Section 6.4. References .....	136
<b>Appendix 1. Density Intercalibration of Wind and ACE .....</b>	<b>138</b>
Section A.1. Introduction .....	138
Section A.2. SWEPAM Instrumentation .....	139
Section A.3. Data Analysis .....	140
Section A.4. Conclusion .....	149
Section A.5. References .....	150
<b>Appendix 2. Polar and Wind Data .....</b>	<b>152</b>
Polar MFE Magnetic Field Data .....	153
Wind SWE Solar Wind Data .....	154
Wind MFI Magnetic Field Data .....	155

## List of Figures

Figure 1.1. Interaction between solar wind and Earth's magnetic field	1
Figure 1.2. Polarization along magnetopause boundary	2
Figure 1.3. Simplified solution for magnetospheric compression	3
Figure 1.4. Coronal mass ejection	6
Figure 1.5. Co-rotating interaction region	7
Figure 1.6. Pressure balance	8
Figure 1.7. Magnetospheric compression in three dimensions	9
Figure 1.8. Polar orbits examined	11
Figure 2.1. <i>Araki</i> model	26
Figure 2.2. Physical model of magnetospheric compression in three dimensions	27
Figure 2.3. Standardized compression of T89 model, noon-midnight meridian	37
Figure 2.4. Standardized compression of T89 model, Y-Z planes	37
Figure 2.5. Standardized compression of T96 model, noon-midnight meridian	39
Figure 2.6. Standardized compression of T96 model, Y-Z planes	39
Figure 2.7. Standardized compression of T01 model, noon-midnight meridian	41
Figure 2.8. Standardized compression of T01 model, Y-Z planes	41
Figure 2.9. Standardized compression of MHD model, noon-midnight meridian	44
Figure 2.10. Standardized compression of MHD model, Y-Z planes	44
Figure 2.11. Standardized compression of T96 model, fixed dipole tilt	46
Figure 2.12. Standardized compression of T96 model, fixed southward IMF	47

Figure 2.13. Standardized compression of T96 model, fixed dipole tilt and IMF	.....49
Figure 3.1. Polar observations and standardized compression (T89, T96, & T01)	.....57
Figure 3.2. GOES observations and standardized compression of T89 model	.....59
Figure 3.3. GOES observations and standardized compression of T96 model	.....60
Figure 3.4. GOES observations and standardized compression of T01 model	.....61
Figure 3.5. Correlation fits of Polar and GOES with T89 predictions	.....64
Figure 3.6. Correlation fits of Polar and GOES with T96 predictions	.....66
Figure 3.7. Correlation fits of Polar and GOES with T01 predictions	.....67
Figure 3.8. Magnetospheric compression in three dimensions with currents	.....70
Figure 3.9. Flowchart of T96 model	.....71
Figure 3.10. Correlation fits of Polar and modified versions of T96 predictions	.....72
Figure 3.11. Correlation fits of GOES and modified versions of T96 predictions	.....73
Figure 3.12. Response ratio: Polar $\Delta B$ observations versus $\Delta\sqrt{P_{dyn}}$	.....78
Figure 3.13. Response ratio: Sorted by local time and IMF orientation	.....80
Figure 4.1. Time series plot of 10/12/00 SI with MHD simulations	.....92
Figure 4.2. Time series plot of 9/28/96 SI with MHD simulations	.....95
Figure 4.3. Geoeffective length from shock velocity versus inverse rise time	.....98
Figure 4.4. Geoeffective length sorted by local time and latitude	.....99
Figure 5.1. Generation mechanism of Pc 1-2 waves	.....104
Figure 5.2. Detrended and filtered Polar data for SI on November 22, 1997	.....109
Figure 5.3. Power spectral density function for November 22, 1997 event	.....109
Figure 5.4. Detrended and filtered Polar data for SI on November 7, 1998	.....110

Figure 5.5. Power spectral density function for November 7, 1998 event	.....111
Figure 5.6. Detrended and filtered Polar data for SI on August 6, 1998	.....113
Figure 5.7. Power spectral density function for August 6, 1998	.....114
Figure 5.8. Detrended and filtered Polar data for SI on January 27, 2000	.....115
Figure 5.9. Power spectral density function for January 27, 2000 event	.....116
Figure 5.10. Locator plot of wave growth events, equatorial plane	.....120
Figure 5.11. Locator plot of wave growth events, noon-midnight meridian	.....120
Figure 5.12. Pc 1-2 wave growth occurrence as a function of $K_p$	.....121
Figure 5.13. Pc 1-2 wave growth occurrence as a function of SI magnitude	.....122
Figure A.1. Logarithmic distribution of ACE and Wind solar wind speed	.....141
Figure A.2. Logarithmic distribution of ACE and Wind solar wind density	.....142
Figure A.3. Logarithmic distribution of ACE and Wind solar wind thermal speed	.....142
Figure A.4. Scatter plot of ACE and Wind solar wind density measurements	.....144
Figure A.5. Intercalibration plot ( $N_{Wind}/N_{ACE}$ )	.....145
Figure A.6. Spacecraft separation	.....148
Figure A.7. Intercalibration plot binned according to spacecraft separation	.....148

## List of Tables

Table 3.1. Numerical results from Figures 3.5 – 3.7 .....	68
Table 3.2. Numerical results from Figures 3.10 – 3.11 .....	75
Table 3.3. Numerical results from Figure 3.13 .....	81
Table 5.1. Wave characteristics for November 7, 1998 event .....	112
Table 5.2. Wave characteristics for August 6, 1998 event .....	114
Table 5.3. Wave characteristics for January 27, 2000 .....	117
Table 5.4. Wave characteristics for compressional events .....	118
Table A.1. Intercalibration ( $N_{\text{Wind}}/N_{\text{ACE}}$ ) function of ACE bulk and thermal speed .....	146

## Acknowledgements

First, I would like to thank Chris Russell for providing me with the guidance and insight to complete my dissertation. I would also like to thank him for giving me the opportunity to pursue my academic goals, which will ultimately help me achieve my lifetime and career goals.

I would also like to thank my committee members, Mark Moldwin, Bob Strangeway, and Larry Lyons for their feedback and scientific criticism that helped me to put together a project of such immense proportions. The rest of the IGPP faculty should also be thanked for their suggestions and instruction. Ray Walker thanks for the help preparing for the first oral exam. Jimmy Raeder thanks for helping me branch out my research with the modeling aspect.

My special thanks go to Tamitha Mulligan and Dave Berube who both helped me in innumerable ways. Portions of my analytical work would have stalled without their contributions at crucial times. Plus, they also helped me stay sane throughout this whole journey.

Thanks go to all my other academic peers and fellow indentured servants in IGPP. I would also like to extend this gratitude to all my other friends in the Earth and Space Sciences department at UCLA. I would also like to thank the IGPP computer support staff and the IGPP front office.

## VITA

June 19, 1969	Born, Iowa City, Iowa
1991	B. S., Accounting University of Colorado Boulder, Colorado
1991-1992	Accountant Polymedica Industries, Inc. Wheatridge, Colorado
1992-1993	Project Accountant Bramalea Urban Properties Denver, Colorado
1993-1998	Project Accountant University Corporation for Atmospheric Research Boulder, Colorado
1998	B. A., Physics/Astrophysics Cum Laude University of Colorado Boulder, Colorado
2001	M. S., Geophysics and Space Physics University of California, Los Angeles Los Angeles, California

## PUBLICATIONS AND PRESENTATIONS

Fowler, G. J. and C. T. Russell, Geomagnetic field response along the Polar orbit to rapid changes in the solar wind dynamic pressure, *J. Geophys. Res.*, 106, 18,943-18,956, 2001.

## ABSTRACT OF THE DISSERTATION

The Compression of the Geo-Magnetosphere:  
A Presentation of a Physical Model  
and the Effects of Compression

by

Galen James Fowler

Doctor of Philosophy in Geophysics and Space Physics

University of California, Los Angeles, 2005

Professor Chris T. Russell, Chair

This thesis presents the results from an investigation of magnetospheric compression. In this research we provide the space physics community with an accurate physical model of the magnetospheric response to dynamic pressure fronts traveling in the solar wind. We also solve the question about the mechanism controlling the dynamic nature of the observed compressional signals. Finally we address the problem of energizing the inner magnetosphere via compression.

In this venture, we first present predictions from several models that map out a standardized global change in geomagnetic field when a generic pressure front interacts

with the Earth's magnetosphere. These results all predict the presence of a depression region at high altitudes on the dayside where total fields decrease, and qualitative comparisons with Polar observations prove reasonable. We also use a more rigorous mathematical test to verify the result, which determines the most accurate representation of magnetospheric physics.

We use an MHD model to examine the time dependent ( $\partial/\partial t$ ) nature of observed changes in the geomagnetic field. We establish a connection between the speed of a solar wind structure and the duration of the compressional signal.

Finally, we discuss how magnetospheric compression can lead to an energy transfer from particles to waves. An energy exchange results in a post-compressional enhancement of transverse ULF wave power, and the occurrence rate of these observations exhibit a reliance on the magnitude of the compression.

## Chapter 1: Introduction

### 1.1 Background

*Chapman and Ferraro* first proposed a physical model in the 1930's that illustrates the advancing front of solar plasma draping around the Earth's magnetic field. Their theory treated the solar plasma as an unmagnetized superconducting gas, which could not penetrate the Earth's magnetic field [*Chapman and Ferraro*, 1931, 1932]. Thus, much like a rock in a stream diverts the flow of water, Earth's magnetic field redirects the flow of plasma. Shown in Figure 1.1 is their physical model which compresses the Earth's magnetic field and forms a cavity in the solar plasma. Along the

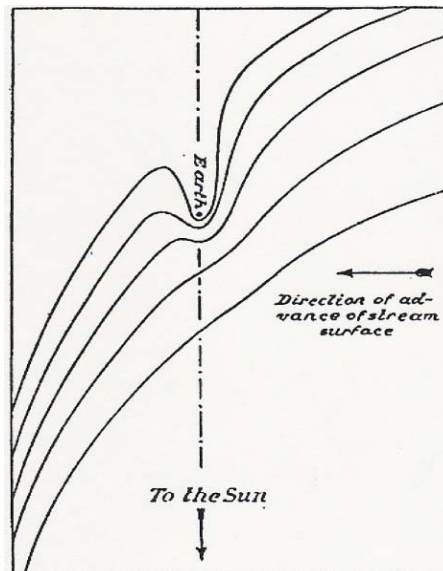


Figure 1.1: An illustration of the interaction between transitory solar plasma and Earth's magnetic field. The region around Earth presents an obstacle to the flow of non-magnetic plasma, which cannot penetrate the magnetic fields. As the solar plasma is diverted around the Earth, it compresses the magnetic fields and a cavity forms in the flow. Illustration from *Chapman and Ferraro* [1931].

boundary of the cavity is a shielding current, now referred to as the Chapman-Ferraro current, which terminates the Earth's magnetic field, keeping the solar plasma field-free. Shown in Figure 1.2 is their interpretation of the magnetopause (no longer held at present), which becomes positively charged on the morning side and negatively on the evening side. This polarization of the plasma stream was thought to produce a dawn-dusk electric field that permits solar plasma to fill the compressed cavity. Originally,

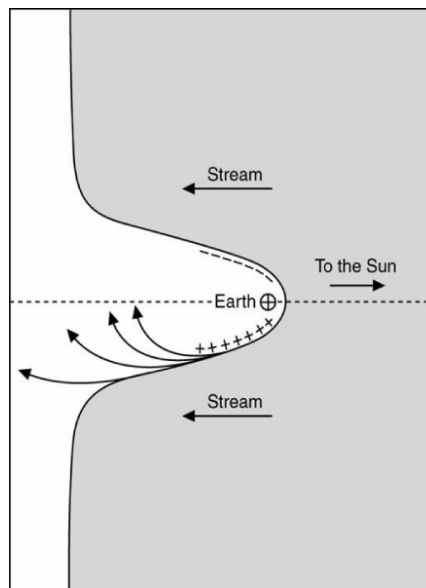


Figure 1.2: *Chapman and Ferraro* speculated that there must be polarization along the boundary of the cavity. Positive particles accumulate on the evening side and negative particles on the morning side. This charge separation generated a westward current thereby, which they observed in magnetic signatures at the Earth's surface. Illustration from *Chapman and Bartels* [1940].

*Chapman and Ferraro* assumed that particle flux into the magnetic cavity leads to a toroidal westward current that decreases the horizontal field component during the main phase of a substorm. This assumption was based on ground magnetometer measurements

of increases and subsequent decreases in the magnetic fields that were associated with the compression of the terrestrial field and the amplification of the ring current that followed [Chapman and Bartels, 1940].

The work done by *Chapman and Bartels* included a simplified model for the compression of the magnetosphere. Illustrated in Figure 1.3 is the theorized interaction between the Sun's plasma and the Earth's magnetic fields. They approximated the transient flow of ionized gas approaching the Earth as a superconducting planar front of infinite length that compresses the Earth's magnetic fields. This is mathematically equivalent to putting a mirror magnetic dipole at an equal distance on the other side of the plasma front. In this model the magnetic field goes to zero at the points labeled "Q". We

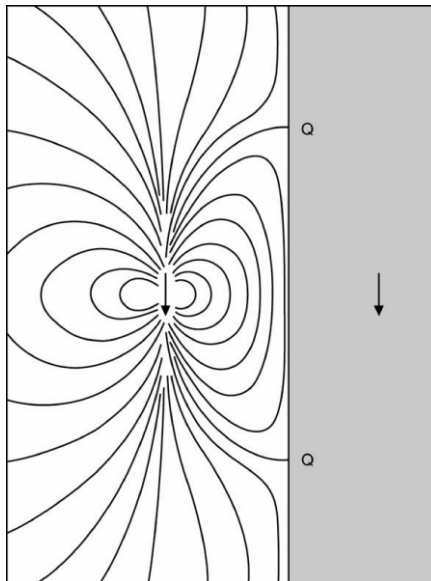


Figure 1.3: A simplified solution for magnetospheric compression. The boundary between the solar plasma and the Earth's magnetic field is an infinite superconducting plane. However, this solution breaks down when used to interpret the model suggested in Figures 1.1 and 1.2 because of the curvature along the cavity boundary. Illustration from *Chapman and Bartels* [1940].

now know that the solar wind flows continuously and is not transitory.

In the 1940's *Hoffmeister* [1943, 1944] reported on comet tails that were not entirely oriented in the radial direction away from the Sun. Spectral observations revealed a second comet tail extending roughly  $5^\circ$  away from the dust tail, which could not be attributed to the radiation pressure from the sun because of unusual kinks and sudden accelerations. In the 1950's *Biermann* [1951, 1957] found that the ion tail persisted even in the absence of solar flares. He interpreted their presence to "solar corpuscular radiation" that accelerated the ions. It was *Eugene Parker* [1958] who suggested that the solar corona streamed from the Sun, which he dubbed "solar wind". These facts were finally confirmed with solar wind measurements by Mariner 2 en route to Venus in 1962 [*Neugebauer and Snyder*, 1966]. Altogether these scientific contributions verified that the solar wind continuously interacts with the Earth's magnetic fields. Soon after, the presence of the magnetopause boundary was confirmed with the Explorer 10 spacecraft in 1961, followed by Explorer 12, which provided continual coverage of the magnetopause [*Cahill and Patel*, 1967].

Present day research concentrates on the importance of magnetospheric compression as a trigger to a variety of magnetospheric processes. Altering the geometry or magnitude of the Earth's magnetic fields affects the energy and distribution of magnetospheric particles. For example, the compressional event on September 24, 1998 was responsible for centrifugal acceleration that transports ionospheric particles to the plasma sheet [*Moore et al.*, 1999; *Russell et al.*, 1999; *Cladis et al.*, 2000]. Another topic

of great relevance is the study of substorms following sudden impulses [*Chao and Lepping, 1974; Kokubun, 1977*]. Other studies have investigated the solar wind dynamic pressure effects on the magnetosphere by looking at the magnetopause location as a function of changes in the solar wind dynamic pressure [*Sibeck, et al., 1991; Roelof and Sibeck, 1993*]. Other relevant topics include enhancement of ionospheric currents [*Zesta et al., 2000*] and energization of relativistic electrons [*Reeves et al., 1997*]. Finally, analogous to the ringing of a bell, the study of hydromagnetic cavity modes links magnetopause motions to field line resonance [*Warnecke et al., 1990*].

Commercial industries with space-based technology are concerned with the affects of magnetospheric compression on their spacecraft. Satellites that determine their orientation relative to the Earth's field may become disoriented when their sensors are confused by rapid changes in the geomagnetic field configuration or the magnetopause boundary is repositioned past the satellites. Power companies need to be concerned with sudden changes in the magnetic fields. If a large amplitude change in  $B$  occurs in a brief amount of time, Faraday's law ( $\partial \mathbf{B} / \partial t = -\nabla \times \mathbf{E}$ ) states that an electric field must be generated. In turn, this electric field drives ionospheric currents, creating fluctuations in the low altitude magnetic fields [*Schutz et al., 1974*]. Induced currents at low altitude will add to existing currents along electrical power lines when the current loop is completed through the conducting layer of the Earth. These currents can exceed the capacity of the transmission systems triggering transformer failures and outages.

This thesis examines the various physical processes related to magnetospheric compressions. First, we must understand what sudden impulses are and how they are

identified. An interplanetary shock traveling in the solar wind that propagates Earthward is large enough to engulf the magnetosphere upon encounter. Shown in Figures 1.4 and 1.5 are illustrations of two solar phenomena that generate interplanetary shocks, coronal mass ejections (CMEs) and co-rotating interaction regions (CIRs), respectively. A CME

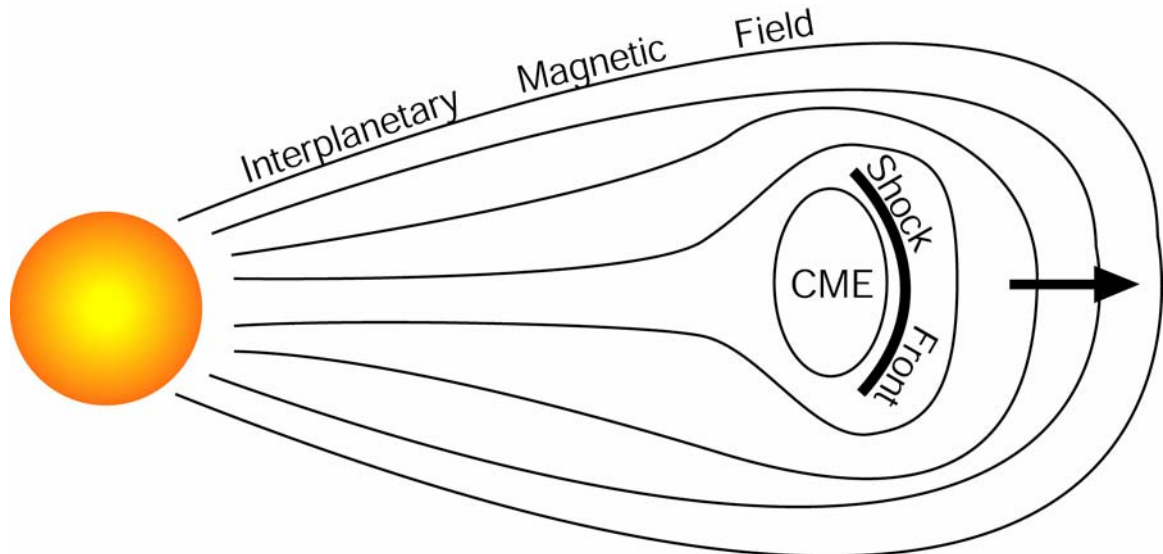


Figure 1.4: Illustration of a Coronal Mass Ejection (CME). High-density plasma traveling at high speed relative to the ambient medium will result in magnetosonic propagation produces a leading edge shock front.

consists of a high density plasma population that can travel at high speeds relative to the ambient medium, thereby producing a leading edge shock. A CIR produces a similar shock, but it results from fast streaming plasma flows being impeded by slower streams. The compression region is a high density region of plasma that generates a leading edge shock, and is trailed by a rarefaction region. In either case, a spacecraft orbiting in the solar wind that is passed by either type of shock will detect a step-function increase in solar wind speed, density, and temperature, as well as a rotation in the Interplanetary

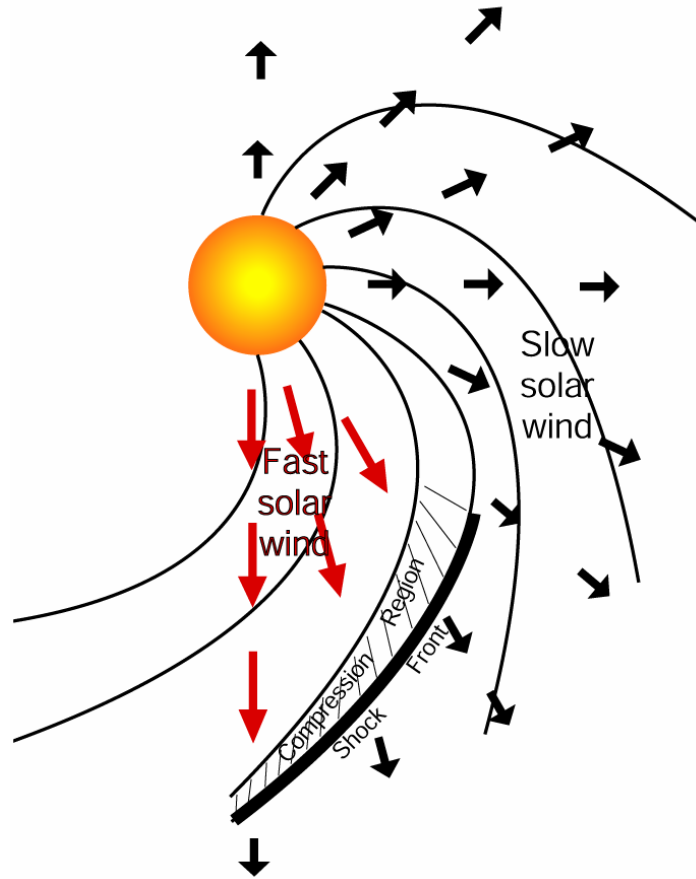


Figure 1.5: Illustration of a Co-rotating Interaction Region (CIR). Fast streaming plasma is impeded by slower ambient plasma. A pile-up of high-density plasma in the compression region travels at magnetosonic speed. A leading edge shock front will trigger magnetospheric compression upon reaching the Earth.

Magnetic Field (IMF). The observed jump in solar wind parameters can be compared to jump conditions of the Rankine-Hugoniot (RH) equations to show that they are shocks.

For this study, 54 of 62 compressional events have been previously classified as interplanetary shocks [Berdichevsky *et al.*, personal communication, 2001]. Events are labeled tangential discontinuities when the jump conditions do not satisfy the shock RH equations but the sum of the thermal and magnetic pressures are equal on either side of the discontinuity. Regardless of the classification of an observed solar wind structure, the

focus of this thesis is to investigate the effects of rapid changes in solar wind dynamic pressure on the magnetosphere as measured in the Earth's reference frame.

Solar plasma dynamic pressure ( $\rho v^2$ ) pushes against the magnetosphere continuously along the magnetopause boundary where a pressure balance exists with the geomagnetic pressure ( $B^2/2\mu_0$ ), as illustrated in Figure 1.6. The rapid change in dynamic pressure associated with a shock front is due to an increase in plasma density traveling at

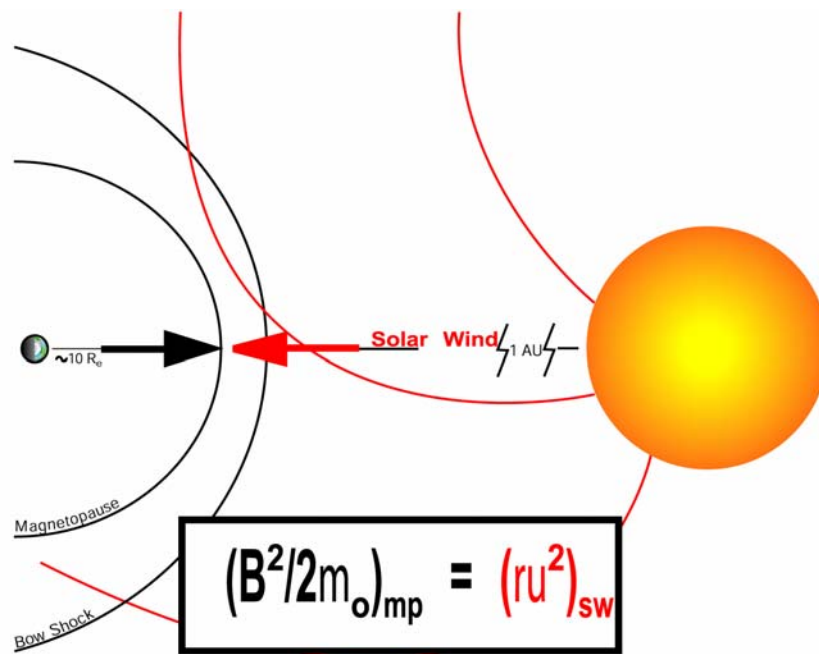


Figure 1.6: Illustration of the pressure balance along the magnetopause boundary between the solar wind dynamic pressure ( $\rho v^2$ ) and the geomagnetic pressure ( $B^2/2\mu_0$ ).

higher speeds. Although there is an increase in plasma temperature across an interplanetary shock front the dynamic pressure as measured in the Earth's frame dominates thermal pressure by several orders of magnitude. Thus, a shock front traveling

in the solar wind is preceded by low pressure plasma and trailed by high pressure plasma, which squeezes the tenuous magnetopause boundary inward as illustrated in Figure 1.7.

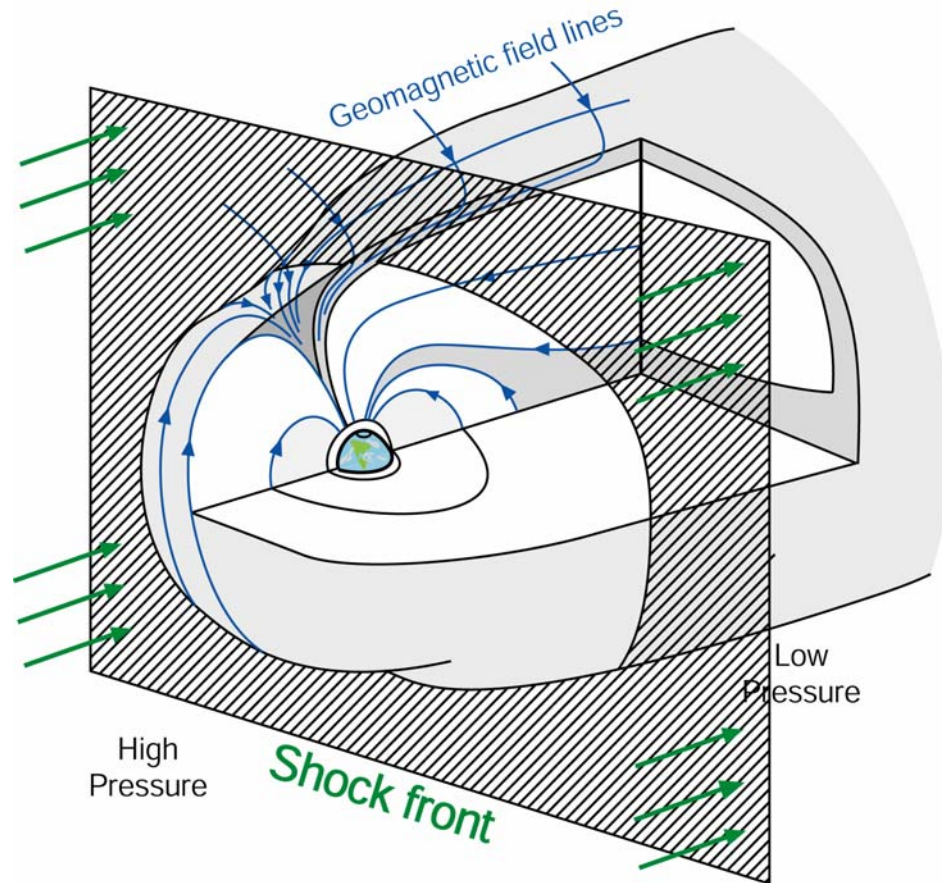


Figure 1.7: Illustration of magnetospheric compression. A shock front is preceded by slow moving low density plasma and trailed by fast moving high density plasma. This solar wind structure envelops the magnetosphere and propagates tailward while continuing to compress the magnetosphere.

The Earth's magnetosphere responds to the change in dynamic pressure with an amplification of magnetic field strength to maintain the pressure balance that deflects the solar wind. In various regions of the magnetosphere the field perturbations generate different changes in the magnetic field magnitude.

Once an interplanetary shock or dynamic pressure front encounters the magnetopause the magnitude of the geomagnetic field begins to change everywhere within the magnetosphere at the speed with which a compressional signal is transmitted to the point of observation. The propagation speed of the solar wind disturbance outside the magnetosphere exceeds the transmission speed. So, as the solar wind pressure enhancement continues to propagate along the outside of the magnetosphere the compressional signal continues to be communicated throughout the magnetosphere. Thus, the rise time of the magnetospheric response is much longer than the step-function increase seen by a spacecraft in the solar wind.

Most previous research on magnetospheric compression has been based on ground-based magnetometers [*Siscoe, et al., 1968; Ogilvie, et al., 1968; Verzariu, et al., 1972; Russell, et al., 1992; Russell and Ginsky, 1993; Russell et al, 1994a, 1994b*]. In the cases of space-based research, only particular regions of the magnetosphere have been studied [*Kokubun, 1983; Nagano and Araki, 1986; Rufenach, et al., 1992; Araki, 1995; Nakai, et al., 1991; Fairfield and Jones, 1996; Ostapenko and Maltsev, 1998*]. The research in this thesis is invaluable to the understanding of the topic because it is a statistical survey of the global magnetosphere, especially away from the equatorial region, filling in the regions not previously studied. Moreover, the effects of the ionospheric currents, especially the Hall currents are not present in the magnetospheric signals simplifying the interpretation of the signals away from the surface of the Earth.

## 1.2 Data and Instrumentation

The magnetospheric data presented in this thesis are based on magnetic field observations recorded by the Polar spacecraft. SI observations in the statistical data set occurred between April 1996 and December 2000. Polar began the period in elliptical orbits highly inclined to the ecliptic plane over the Northern polar region with an apogee of roughly  $9 R_E$ . Eventually the orbit will precess southward until the orbital apogee reaches the Southern hemisphere of the magnetosphere. Currently, the apogee is in the equatorial region, which allows Polar to record magnetic fields near the sub-solar point. Shown in Figure 1.8 are sample orbits projected onto the noon-midnight meridian in the

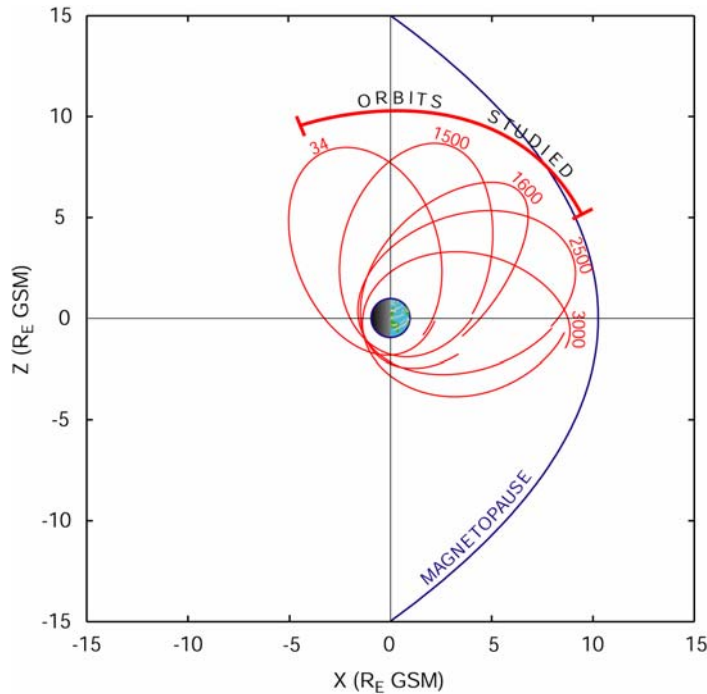


Figure 1.8: Illustration of Polar trajectories in the noon-midnight plane. Examples of Polar orbits are drawn in red and labeled numerically. The period investigated in this thesis (April 1996 to December 2000) is covered by orbits #34 through # 2350.

GSM coordinate system. The red arc illustrates the high altitude magnetospheric regions studied in this thesis, which are sampled over the duration of the mission spanning from orbit 34 to 2350. The only other spacecraft to explore these regions are the HEOS-2 spacecraft [Hedgecock, 1975] and HAWKEYE [Van Allen, 1992], both of which had low data rates. The Magnetic Field Experiment (MFE) onboard the Polar orbiter was used to record the magnetospheric response to the dynamic pressure changes in the solar wind [Russell *et al.*, 1995]. At the end of a 6 meter boom are two triads of orthogonal fluxgate magnetometer sensors, which are separate from the analog and data processing instruments onboard Polar. The instrument is designed to study dynamic fields in the polar cusp, magnetosphere, and magnetosheath, which allows for a thorough investigation of the global magnetosphere especially at high altitudes. Therefore, the magnetometer measures fields in three ranges of 700, 5700, and 47,000nT depending upon the background fields. Data is provided in three resolutions of 1 minute, 6 second, and 8 samples per second. SI observations were made with the 6-second data, unless higher resolution data were necessary. Steady state magnetic field values in the magnetosphere were averaged over 15 minute intervals upstream and downstream of the sudden impulse, except when the data analysis required the maximum and minimum values of the residual magnetic field. Throughout this thesis all presentations of magnetic field observations by Polar are residual values that have been detrended for spacecraft motion by subtracting a background magnetic field. This background subtraction is based on the *in situ* magnetic field determined by the Tsyganenko 96 model with dynamic pressure of 2 nPa, IMF values of  $B_y = B_z = 0$ , and  $Dst = 0$ . The magnetospheric

configuration for the background subtraction is an approximation of the field described by *Sibeck et al.* [1991].

We also investigate the same compressional events with the GOES 8, 9 and 10 spacecraft. These spacecraft orbit along the equatorial plane, thus our examination of magnetospheric compression is global in nature. Magnetic field measurements are recorded in 1-minute intervals, which is sufficient for determining SI magnitudes, but not the dynamic nature of the SI signal.

The strength of a sudden impulse is controlled by the solar wind dynamic pressure, which is the primary signature of an interplanetary shock. As mentioned above, plasma instrumentation onboard a spacecraft that is passed by a shock front will observe an increase in the number density, flow speed, and plasma temperature. In addition, there is a rotation in the interplanetary magnetic field (IMF) across a shock front where a fast shock bends the magnetic field towards the shock normal. Interplanetary shocks and pressure fronts were recorded by Wind using the 64-second SWE (Solar Wind Experiment) data and 92-second MFI (Magnetic Field Investigation) data [*Ogilvie et al.*, 1995; *Lepping et al.*, 1995]. The SWE instrument uses a Faraday cup subsystem that measures electric currents generated by solar wind ions that impinge upon semi-circular collector plates. The solar wind speed, density, and temperature are determined by calculating weighted moments of the currents measured in each energy window. The Faraday cups are situated such that solar wind is measured 2/3 of the time and variations in the full velocity distribution function can be observed with a time resolution of

approximately one second. Two sensors cover an energy/charge range from 150 V to 8 kV for the interplanetary ions, and the key parameter measurement ranges and precision are as follows: proton velocity (3 components) 200-1250 km/s  $\pm$  3%; proton number density 0.1-200/cc  $\pm$  10%; and thermal speed 0-200 km/s  $\pm$  10%. The MFI instrumentation consists of dual triaxial fluxgate magnetometers mounted on a boom. The magnetometer covers eight dynamic ranges from  $\pm$  4nT to  $\pm$  65,536 nT. Solar wind parameters were averaged over 15 minute intervals upstream and downstream of the interplanetary shock front to determine steady state conditions.

When a pressure front is identified in the solar wind its arrival time at the magnetosphere is determined by the solar wind speed and the location of Wind relative to Earth. For inclusion in this study we require a dynamic pressure change detected in the solar wind and an associated SI response. From these data, we use 62 events to examine magnetospheric compressions. Many compressions are not analyzed because of the unfavorable location of Polar either at perigee where spatial gradients are large, or outside the magnetopause where magnetic turbulence masks the compressional signal. All data are presented in GSM (Geocentric Solar Magnetospheric) coordinates.

Pressure fronts were also identified with the ACE spacecraft using SWEPAM (Solar Wind Electron and Proton Alpha Measurements) and MFI (Magnetic Field Investigation). However, the ACE spacecraft operated over a shorter period than the Wind spacecraft, so there is a limited set of events detected by both spacecraft. When both Wind and ACE were used for the identification of interplanetary shocks, an intercalibration was necessary since measured solar wind parameters were not always in

agreement. Adjustments to measured densities are determined as a function of two solar wind parameters, and the results are discussed in Appendix 1. The material in Appendix 1 does not treat either data set preferentially, but it does discuss the source of potential differences between the instruments used to measure the solar wind density.

Discrepancies are attributed to instrumentation differences and spatial variations in solar wind structures that arise due to significant spacecraft separation of the spacecraft. This comparison allows one to study solar wind phenomena with either data set and remain individually consistent.

### **1.3 Models**

Three steady state magnetospheric models are used in this thesis, which were developed by Nikolai Tsyganenko in 1989, 1996, and 2001. From herein we will refer to these models by their acronyms: T89, T96, and T01 respectively. We use these models to predict changes in the magnetic field throughout the magnetosphere based on changes in specific solar wind parameters.

The T89 model is an analytical model that uses a dipole magnetic field confined within a superconducting paraboloid of revolution. The cavity does not contain plasma, so the model approximates the magnetopause boundary and the Chapman-Ferraro current. Input parameters for this model include the solar wind dynamic pressure and dipole tilt. A detailed discussion of the T89 model is presented in Section 2.2.1.

The T96 model is an empirical model that determines the magnetic field contributions from several current systems which are not present in the T89 model. This model includes the effects from the field-aligned Birkeland currents, the ring current and the tail current. Input parameters for this model include the solar wind dynamic pressure, the IMF  $B_Y$  and  $B_Z$  components, the dipole tilt, and Dst values. A detailed discussion of the T96 model is presented in Section 2.2.2. It is possible to modify this model such that magnetic field contributions from three current systems are removed individually and jointly to examine the relative effects of these localized currents on the magnetic field changes. This aspect of the research is discussed in greater detail in Section 3.4.

The T01 model is another empirical model that is essentially an improved version of the T96 model. Numerical calculations of the magnetospheric currents are corrected in this model based on recent observational evidence. Additionally, that improves the determines the magnetic field contributions from several current systems which are not present in the T89 model. Input parameters for this model are the same as the T96 model with two additional parameters that are based on the solar wind electric field. A detailed discussion of the T01 model is presented in Section 2.2.3.

We also use an MHD model to investigate the time rate of change of SIs. This model is a magnetospheric-ionospheric coupled model, where the magnetospheric model was designed by *Raeder* [1999] and *Raeder et al.* [2001] and the ionospheric model was provided by *Fuller-Rowell et al.* [1996]. The ionospheric portion of the model couples the thermosphere and ionosphere. The MHD model accepts the following solar wind

input parameters: solar wind speed, density, IMF  $B_Y$  and  $B_Z$  components, thermal pressure and dipole tilt. To expedite the simulation runs solar wind inputs were made in 90-second intervals and output resolution is in 10-seconds intervals. The model was used to replicate *in situ* sudden impulses measured by Polar. We use the model to investigate not only SI magnitudes as done with the Tsyganenko models, but also the time evolution of the compressional signals. Additionally, we examine the effect of solar wind speed on SI rise times by adjusting the solar wind speed to simulate faster or slower approaching pressure fronts. This aspect of the research is discussed in Chapter 4.

#### **1.4 Synopsis of thesis**

The scope of this thesis is to better understand the phenomenon known as magnetospheric compression. In Chapter 2 we begin our investigation with the *Tsyganenko* magnetospheric models (T89, T96, & T01). With this work we consider possible physical models of the global magnetospheric response to dynamic pressure fronts traveling in the solar wind. For each model we use a step function increase in dynamic pressure as the only input parameter. This simulated pressure pulse generates a global change in magnetic field ( $\Delta B$ ), which is illustrated in color contour plots of magnetospheric regions. We see that each model predicts a decrease in magnetic field magnitude ( $-\Delta B$ ) at high altitudes on the dayside, but the magnetospheric response along the equator is different for each model. Compression of local current systems generates variations in the global  $\Delta B$  response. Further, we use dipole tilt and IMF orientation as

additional input parameters in the T96 and T01 models. We see the  $-\Delta B$  regions persist, although the volume and intensity of the response varies. We offer these predictions as a standardized magnetospheric response in three dimensions. In the following chapter we use observational evidence to establish the correct physical model.

In Chapter 3 we use Polar and GOES observations of SIs to qualitatively verify the standardized compression results. We will find sufficient correlation between observations and the standardized models to warrant further investigation. Thus, the full complement of input parameters for each model is utilized, which consists of Wind observations upstream and downstream of the solar wind structure. We then use numerical fits to quantify the comparison between *in situ*  $\Delta B$  predictions and Polar observations. Based on the fit quality we offer the T01 model as the most realistic representation of the physical processes in magnetospheric compression. We further correlate the global  $\Delta B$  response to the compression of local currents. To accomplish this we modify the T96 model to exclude field perturbations from three magnetospheric currents: field-aligned, ring and tail. We again use numerical fits to statistically compare model predictions to observations. A poor fit indicates the relative importance of each current's contribution to the global  $\Delta B$  response. We verify that high altitude depression regions are generated by the compression of the magnetopause current and the nightside depression region is generated by the compression of the tail current.

In Chapter 4 we test the relationship between solar wind pressure fronts and the dynamic response of the magnetosphere. The rise time of the compressional signal correlates to the duration of interaction between the solar wind structure and the

magnetosphere. The MHD model is used to investigate the effect of shock velocity on the rise times of SIs. We find that fast traveling shock fronts compress the magnetosphere rapidly, and conversely slow traveling shock fronts extend the duration of SIs. We also use the observed shock velocities to calculate the geoeffective length, which is the anti-sunward distance from the sub-solar point from which a shock front can affect magnetic fields. We find an average geoeffective length of  $18.7 R_E$ , which is consistent with previous research [*Ondoh*, 1963; *Nishida*, 1966].

In Chapter 5 we go one step further to investigate another consequence of magnetospheric compression, the enhancement of Ultra-low frequency (ULF) waves. We present a physical model of generating ULF waves when particle energy is transferred into wave energy. This phenomenon is observed as an enhancement in transverse wave power after the passage of the solar wind front. We identify enhanced resonance in the Pc 1-2 frequency band for one third of our compressional events. There are a few cases when the ULF waves are attenuated. The occurrence of energy transfer events does not exhibit spatial dependence, nor does the occurrence rate correlate with the state of the magnetosphere at the time of compression. However, it appears that when more work is done on the magnetosphere by the solar wind the greater the chance that particle and wave will exchange energy.

Appendix 1 is included so that we may consider the limitations associated with the solar wind parameters. The ACE spacecraft was occasionally used to identify shock structures in the solar wind, but the mission timeline does not overlap with the early years of the Polar mission. This period is critical because Polar orbits at higher latitudes, which

is necessary for a global investigation. Thus, the Wind spacecraft is the preferred solar wind monitor. However, simultaneous measurement of solar wind the events by both ACE and Wind were not always in good agreement. For this reason we provide a method of comparing density measurements between the spacecraft as a function of solar wind bulk velocity and thermal velocity. This comparison analysis is used to assess error in other chapters.

Presented in Appendix 2 is a numerical summary of spacecraft observations for the solar wind pressure fronts and the associated SIs. Solar wind values are measured by the SWE and MFI instruments onboard Wind. Magnetic field measurements within the magnetosphere are measured by the MFE instrument onboard Polar.

## 1.5 References

Araki, T., Response of the Earth's magnetosphere to dynamic pressure variation of solar wind, *Proc. of the Second SOLTIP Symposium*, Nakaminato, Japan, 13-17 June 1994, STEP GBRSC News, Vol 5., pp. 279-282, 1995.

Biermann, L., Kometenschweife und solare Korpuskularstrahlung, *Z. Astrophys.*, 29, 274-286, 1951.

Biermann, L. Untitled letter, *Observatory*, 77, 109, 1957.

Burton, R. K., R. H. McPherron, and C. T. Russell, An empirical relationship between interplanetary conditions and Dst, *J. Geophys. Res.*, 80, 4204-4214, 1975.

Cahill, L. J. and V. L. Patel, The boundary of the geomagnetic field, August to November 1961, *Planet. Space Sci.*, 15, 997-1033, 1967.

Cahill, L. J. Jr., Early studies of the boundary of the geomagnetic field: A historical review, *Physics of the Magnetopause, Geophys. Mono.*, 90, 9-14, 1995.

Chapman, S., and V. C. A. Ferraro, A new theory of magnetic storms, Part 1, *Terrest. Magnetism and Atmospheric Elec.*, 36, 77-97, 1931.

Chapman, S., and V. C. A. Ferraro, A new theory of magnetic storms, Part 1, The initial phase, *Terrest. Magnetism and Atmospheric Elec.*, 37, 147, 1932.

Chapman, S., and J. Bartels, Theories of magnetic storms and aurorae, *Geomagnetism Vol. II*, Clarendon Press, Oxford, pp. 850-861, 1940.

Chao, J. K. and R. P. Lepping, A correlative study of ssc's, interplanetary shocks, and solar activity, *J. Geophys. Res.*, 79, 1799, 1974.

Cladis, J. B., H. L. Collin, O. W. Lennartsson, T. E. Moore, W. K. Peterson, and C. T. Russell, Observations of centrifugal acceleration during compression of magnetosphere, *Geophys. Res. Lett.*, 27, 915-918, 2000.

Collier, M. R., J. A. Slavin, R. P. Lepping, K. Ogilvie, A. Szabo, H. Laakso, and S. Taguchi, Multi-spacecraft observations of sudden impulses in the magnetotail caused by solar wind pressure discontinuities: Wind and IMP 8, *J. Geophys. Res.*, 103, 17,293-17,305, 1998.

Fairfield, D. H., N. A. Tsyganenko, A. V. Usmanov, and M. V. Malkov, A large magnetosphere magnetic field database, *J. Geophys. Res.*, 99, 11,319-11,326, 1994.

- Fairfield, D. H. and J. Jones, Variability of the tail lobe field strength, *J. Geophys. Res.*, 101, 7785-7791, 1996.
- Fowler, G. J. and C. T. Russell, Geomagnetic field response along the Polar orbit to rapid changes in the solar wind dynamic pressure, *J. Geophys. Res.*, 106, 18,943-18,956, 2001.
- Fuller-Rowell, T. J., D. Reese, S. Quegan, R. J. Moffett, M. V. Codrescu, and G. H. Millward, A coupled thermosphere-ionosphere model (CTIM), in *STEP Report*, ed. R. Schunk, Scientific Committee on Solar Terrestrial Physics (SCOSTEP), NOAA/ NGDC, Boulder, Co., 217, 1996.
- Hoffmeister, C., Physikalisch Untersuchungen auf Kometen, I. Die Bewegung des primären Schweifstrahl zum Radiusvektor, *Z. Astrophys.*, 22, 265-285, 1943.
- Hoffmeister, C., Physikalisch Untersuchungen auf Kometen, II. Die Bewegung des Schweirmaterie und die Repulsivkraft der Sonne beim Kometen, *Z. Astrophys.*, 23, 1-18, 1944.
- Kokubun, S., R. L. McPherron, and C. T. Russell, Triggering of substorms by solar wind discontinuities, *J. Geophys. Res.*, 82, 74-86, 1977.
- Kokubun, S, Characteristics of storm sudden commencement at geostationary orbit, *J. Geophys. Res.*, 88, 10,025-10,033, 1983.
- Lepping, R. P., M. H. Acuña, L. F. Burlaga, W. M. Farrell, J. A. Slavin, K. H. Schatten, F. Mariani, N. F. Ness, F. M. Neubauer, Y. C. Whang, J. B. Byrnes, R. S. Kennon, P. V. Panetta, J. Scheifele, and E. M. Worley, The Wind magnetic field investigation, *Space Sci. Rev.*, 71, 207-229, 1995.
- Moore, T. E., W. K. Peterson, C. T. Russell, M. O. Chandler, M. R. Collier, H. L. Collin, P. D. Craven, R. Fitzenreiter, B. L. Giles, and C. J. Pollock, Ionospheric mass ejection in response to a CME, *Geophys. Res. Lett.*, 26, 2339-2342, 1999.
- Nagano, H., and T. Araki, Seasonal variation of amplitude of geomagnetic sudden commencements near midnight at geostationary orbit, *Planet. Space Sci.*, 24, 205-217, 1986.
- Nakai, H., Y. Kamide, and C. T. Russell, Influences of solar wind parameters and geomagnetic activity on the tail lobe magnetic field: a statistical study, *J. Geophys. Res.*, 96, 5511-5523, 1991.
- Neugebauer, M. and C. W. Snyder, Mariner 2 observations of the solar wind, *J. Geophys. Res.*, 71, 4469-4484, 1966.

- Ogilvie, K. W., L. F. Burlaga, and T. D. Wilkerson, Plasma observations on Explorer 34, *J. Geophys. Res.*, 73 6809, 1968.
- Ogilvie, K. W., D. J. Chornay, R. J. Fritzenreiter, F. Hunsaker, J. Keller, J. Lobell, G. Miller, J. D. Scudder, E. C. Sittler, R. B. Torbert, D. Bodet, G. Needell, A. J. Lazarus, J. T. Steinberg, J. H. Tappan, A. Mavretic, and E. Gergin, SWE, A comprehensive plasma instrument for the Wind spacecraft, *Space Sci. Rev.*, 71, 55-77, 1995.
- Ostapenko, A. A. and Y. P. Maltsev, Three-dimensional magnetospheric response to variations in the solar wind dynamic pressure, *Geophys. Res. Lett.*, 25, 261-263, 1998.
- Parker, E. N., Dynamics of the interplanetary gas and magnetic fields, *Astrophys. Jrl.*, 128, 664-676, 1958.
- Parker, E. N., Interaction of the solar wind with the geomagnetic field, *Phys. Fluids*, 1, 171, 1958.
- Patel, V. L., Sudden impulses in the geomagnetotail and the vicinity, *Planet. Space Sci.*, 20, 1127-1136, 1972.
- Raeder, J., Modeling the magnetosphere for northward interplanetary magnetic field: Effects of electrical resistivity, *J. Geophys. Res.*, 104, 17-357, 1999.
- Raeder, J., Y. L. Wang, and T. J. Fuller-Rowell, Geomagnetic storm simulation with a coupled magnetosphere-ionosphere-thermosphere model, in *Space Weather*, ed. P. Song, H. Singer, and G. Siscoe, Geophysical Monograph Series, Vol. 125, 2001.
- Reeves, G. D., D. N. Baker, R. D. Belian, J. B. Blake, T. E. Cayton, J. F. Fennell, R. H. W. Friedel, M. G. Henderson, X. Li, M. M. Meier, T. G. Onsager, R. S. Selesnick, and H. E. Spence, Relativistic electron response to the January 1997 magnetic cloud: Coordinated observations from 12 satellites, *IAGA General Assembly*, Uppsala, Sweden, August 5-15, 1997.
- Roelof, E. C. and D. G. Sibeck, Magnetopause shape as a bivariate function of the interplanetary magnetic field  $B_z$  and solar wind dynamic pressure, *J. Geophys. Res.*, 98, 21,421-21,450, 1993.
- Rufenach, C. L., R. L. McPherron, and J. Schaper, The quiet geomagnetic field at geosynchronous orbit, and its dependence on solar wind dynamic pressure, *J. Geophys. Res.*, 97, 25-42, 1992.
- Russell, C. T., M. Ginskey, S. Petrinec, and G. Le, The effect of solar wind dynamic pressure changes on low and mid-latitude magnetic records, *Geophys. Res. Lett.*, 19, 1227-1230, 1992.

Russell, C. T. and M. Ginskey, Sudden impulses at low latitudes; transient response, *Geophys. Res. Lett.*, 20, 1015-1018, 1993.

Russell, C. T., M. Ginskey, and S. M. Petrinec, Sudden impulses at low-latitude stations: Steady state response for northward interplanetary magnetic field, *J. Geophys. Res.*, 99, 253-261, 1994a.

Russell, C. T., M. Ginskey, and S. M. Petrinec, Sudden impulses at low latitude stations: Steady state response for southward interplanetary magnetic field, *J. Geophys. Res.*, 99, 13,403-13,408, 1994b.

Russell, C. T., R. C. Snare, J. D. Means, D. Pierce, D. Dearborn, M. Larson, G. Barr, and G. Le, The GGS/Polar magnetic field investigation, *Space Sci. Rev.*, 71, 563-582, 1995.

Russell, C. T., X. W. Zhou, P. J. Chi, H. Kawano, T. E. Moore, W. K. Peterson, J. B. Cladis, and H. J. Singer, Sudden compression of the outer magnetosphere associated with an ionospheric mass ejection, *Geophys. Res. Lett.*, 26, 2343-2346, 1999.

Schutz, S., G. J. Adams, F. S. Mozer, Electric and magnetic fields measured during a sudden impulse, *J. Geophys. Res.*, 79, 2002-2004, 1974.

Sibeck, D. G., R. E. Lopez, and E. C. Roelof, Solar wind control of the magnetopause shape, location, and motion, *J. Geophys. Res.*, 96, 5489-5495, 1991.

Siscoe, G. L., V. Formisano, and A. J. Lazarus, Relation between geomagnetic sudden impulses and solar wind pressure changes: an experimental investigation, *J. Geophys. Res.*, 73, 4869-4874, 1968.

Su, S. Y., and A. Konradi, Magnetic field depression at the Earth's surface calculated from the relationship between the size of the magnetosphere and *Dst* values, *J. Geophys. Res.*, 80, 195, 1975.

Verzariu, P., M. Sugiura, and I. B. Strong, Geomagnetic field variations caused by changes in the quiet time solar wind pressure, *Planet. Space Sci.*, 20, 1909, 1972.

Warnecke, J., H. Lühr, and K. Takahashi, Observational features of field line resonances excited by solar wind pressure variations on 4 September 1984, *Planet. Space Sci.*, 38, 1517-1531, 1990.

Zesta, E., H. J. Singer, D. Lummerzheim, C. T. Russell, L. R. Lyons, and M. J. Brittnacher, The effect of the January 10, 1997 pressure pulse on the magnetosphere-ionosphere current system, *Magnetospheric Current Systems, Geophysical Monograph*, 118, 217-226, 2000.

## Chapter 2: SI Predictions by Models

### 2.1 Introduction

In this chapter we examine the predicted changes in magnetic field magnitude ( $\Delta B_T$ ) throughout the magnetosphere as a result of an increase in the solar wind dynamic pressure. This work will be the foundation of possible three dimensional physical models that illustrate magnetospheric compression. This analysis is based on magnetospheric models, which include an analytic model, two empirical models and an MHD model. Changes in  $B_T$  are examined with the *Tsyganenko* models, known hereafter as the T89, T96 and T01 models [*Tsyganenko*, 1989b, 1996a, 2002a, 2002b], by comparing global magnetic field values upstream and downstream of a simulated dynamic pressure front that moves along the exterior of the magnetosphere. The same simulated solar wind conditions are used as inputs into the MHD model [*Raeder et al.*, 2001] to determine  $\Delta B_T$  globally. Results from each model are compared and all these models predict a dayside region at high altitudes where the total magnetic field decreases ( $-\Delta B_T$ ), which is referred to hereafter as a depression region. Each model predicts a slightly different response throughout the magnetosphere, particularly in the equatorial regions. The variety of  $\Delta B$  responses predicted by each model is a result of compressing different local current systems, which are discussed on a model by model basis in the sections below. The *Tsyganenko* models were also examined with additional changes in other input parameters, depending on the available choices for each model. The results show that the

depression regions persist despite additional input parameters. This qualitative analysis with the models provides the groundwork for a more quantitative analysis of Polar observations to these same models in Chapter 3.

This research is significant because it addresses the problem of magnetospheric compression in a global perspective. As discussed in the previous chapter, magnetic pressure in the magnetosphere ( $B^2/2\mu_0$ ) deflects the solar wind dynamic pressure ( $\rho v^2$ ) so that the solar wind flows along the magnetopause. A step-function increase in the dynamic pressure generates a global change in magnetospheric magnetic fields to maintain the pressure balance along the magnetopause boundary. Presented in Figure 2.1 is an illustration of *Araki's* model [1994], which is often assumed to describe the current

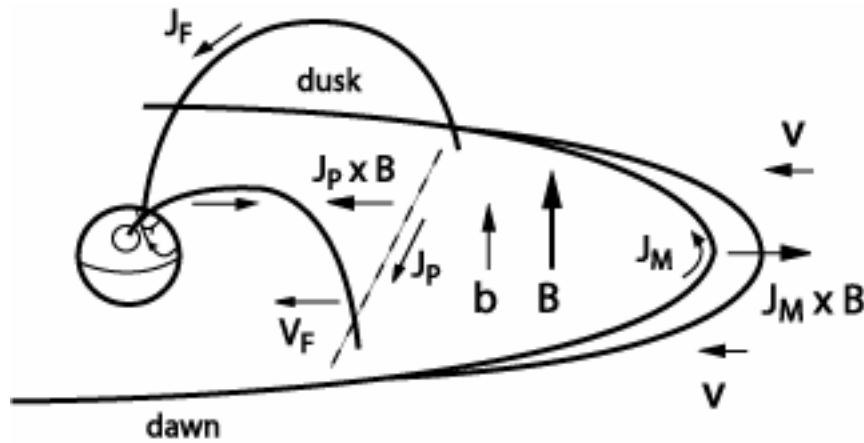


Figure 2.1: Geo-magnetospheric compression along the dayside equatorial region where the solar wind ( $\mathbf{V}$ ) approaches from the right. In response the dawn-to-dusk magnetopause current ( $\mathbf{J}_M$ ) is amplified, which produces a Sunward oriented force ( $\mathbf{J}_M \times \mathbf{B}$ ). Illustration from *Araki* [1994].

systems responsible for the sudden impulse signal. However, as we discuss here, this model is incorrect as it does not describe the reduction of magnetic field strength at high

latitudes. Moreover, the *Araki* model closes a compressed magnetopause current through a compressional front that travels in the magnetosphere, which is an oversimplification of the physical process.

Presented in Figure 2.2 is a three dimensional illustration of an interplanetary shock moving along the exterior of the magnetosphere. An interplanetary shock moves

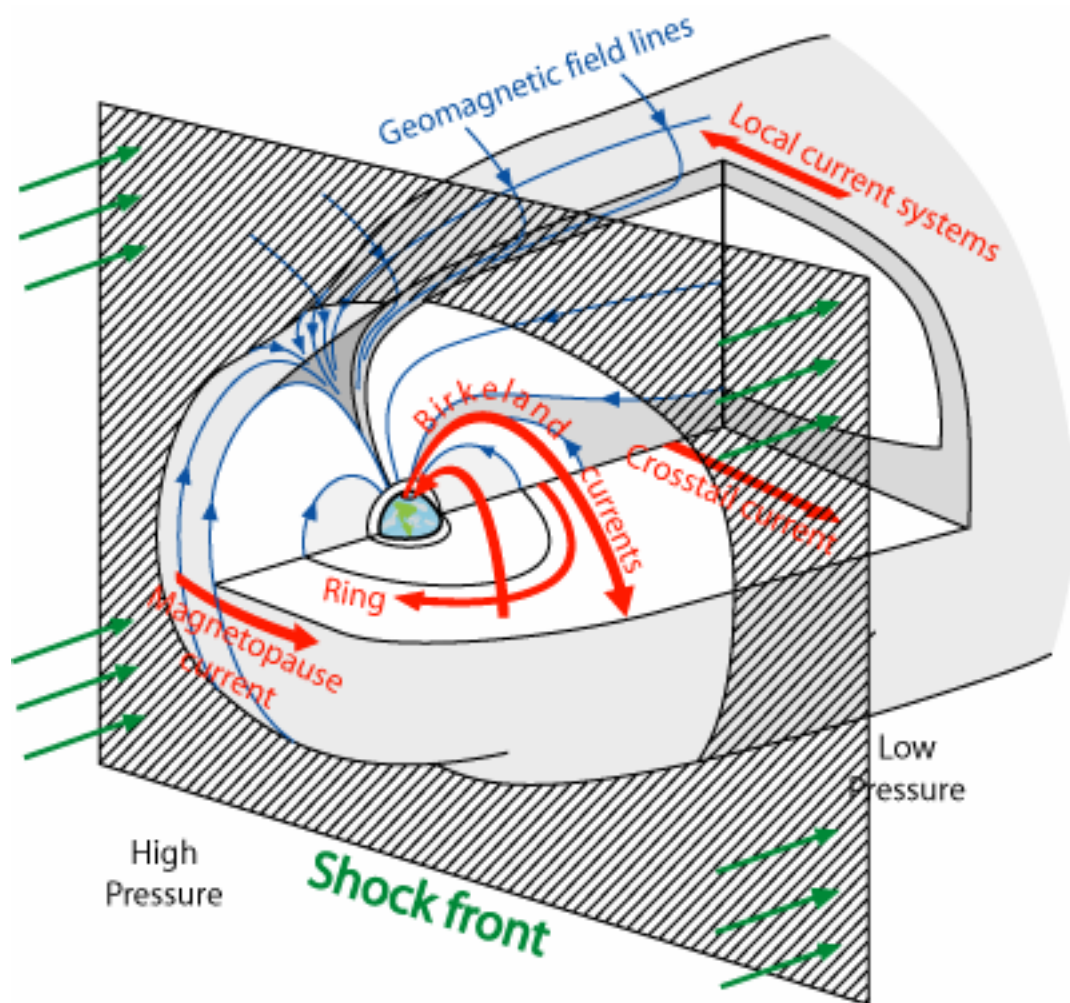


Figure 2.2: Illustration of an interplanetary shock interacting with the magnetosphere. The high solar wind dynamic pressure has already compressed the dayside magnetopause. As the shock front moves tailward other local currents are compressed, which generates field perturbations throughout the magnetosphere.

the magnetopause boundary inward and amplifies the magnetopause current, which closes through the boundary on the nightside. Other local current systems are also amplified by the compression to produce field perturbations that contradict the *Araki* model. A proper physical model needs to take into account that perturbations due to the increased magnetopause current are not necessarily parallel to the internal field away from the equatorial plane. The *Tsyganenko* models are used to determine a global  $\Delta B$  response to a simulated pressure front traveling in the solar wind. The material in this chapter presents the predicted  $\Delta B$  response qualitatively. The material in the following chapter builds on this foundation and presents the predicted  $\Delta B$  response quantitatively. Together these investigations provide the basis for a three-dimensional model of the magnetospheric response to rapid dynamic pressure changes in the solar wind.

### *2.1.1 Description of the T89 model*

*Tsyganenko* solves the boundary problem for a tilted dipole magnetic field trapped in an axially symmetric oblong ellipsoidal cavity of revolution [1989b]. Previous models approximated the boundary field for a non-zero dipole tilt using spherical harmonic expansions, but these models were only valid in near-Earth regions inside of  $10 R_E$  [Mead, 1964; Choe *et al.*, 1973; Halderson *et al.*, 1975]. Subsequent models provided a simple representation of the magnetopause boundary current field as a paraboloid [Alekseev and Shabansky, 1972; Stern, 1985]. Other research determined that the location of the magnetopause boundary contracts and expands as a result of changes in

solar wind dynamical pressure  $P_d = \rho v^2$  [Mead and Beard, 1964]. From this theoretical basis, *Tsyganenko* developed a mathematical representation of magnetic fields that is not only valid for sufficiently extended regions ( $X_{\text{GSM}} \geq -30 R_E$ ), but also capable of determining the magnetospheric dimensions based on solar wind momentum flux. This analytical representation of the magnetosphere is referred to as the T89 model throughout the thesis. One caveat for the T89 model is that it is a vacuum model and does not include effects of the magnetospheric plasma, such as the diamagnetic effect of the plasma sheet, field aligned currents or the ring currents. One advantage for the T89 model is that it demonstrates what field changes can be attributed solely to the magnetopause currents. Shown below and in Chapter 3 are the results of the T89 model when upstream and downstream solar wind inputs are used to determine changes in global geomagnetic fields.

### *2.1.2 Description of the T96 model*

In an attempt to include realistic plasma effects *Tsyganenko* also developed empirical magnetospheric models that served as a useful guide for the magnetospheric response to the solar wind by utilizing observational data and theory [1987, 1989a, 1996a]. *Tsyganenko*'s work is founded on theoretical models from existing data-based models available [Mead and Fairfield, 1975; *Tsyganenko and Usmanov*, 1982], which originally lacked the ability to correlate magnetospheric configurations to solar wind parameters. *Tsyganenko* developed the T96 model by upgraded earlier empirical models

[*Tsyganenko, 1987*] and the model, known as T89c [1989a]. These models neither prescribe the size of the magnetopause as a function of solar wind conditions, nor do they prescribe the interconnection across the boundary separating the Earth's magnetic field and the IMF.

The T96 model mathematically represents the magnetic field contribution from each major current system and an internal background field determined by IGRF when both are correlated to determinable parameters observed in the solar wind. External magnetic field values ( $\mathbf{B}_E$ ) are determined as the sum of contributions from all major magnetospheric current systems:

$$\mathbf{B}_E = \mathbf{B}_{MP} + \mathbf{B}_{RC} + \mathbf{B}_T + \mathbf{B}_{R1} + \mathbf{B}_{R2} + \mathbf{B}_I \quad (\text{Eqn. 2.1})$$

The terms on the right side of Equation 1 are the magnetic field contributions from the magnetopause currents ( $\mathbf{B}_{MP}$ ), the ring current ( $\mathbf{B}_{RC}$ ), the tail current ( $\mathbf{B}_T$ ), the Birkeland region 1 and 2 currents ( $\mathbf{B}_{R1} + \mathbf{B}_{R2}$ ), and the interconnection current ( $\mathbf{B}_I$ ), respectively. The T96 model determines the size and shape of the magnetopause based on the solar wind dynamic pressure as determined by magnetopause observations [*Sibeck et al., 1991*]. Despite the fact that the magnetopause shape is also dependent on the IMF orientation [*Petrinec and Russell, 1993*], the model exclusively uses the IMF for parameterization of the tail, Birkeland region 1, and interconnection currents [*Tsyganenko, 1996*]. Once the magnetopause location is known, the  $\mathbf{B}_{MP}$  is determined as the field responsible for shielding the field of all external magnetospheric sources within

the boundary. The magnetic field contributions from the ring current ( $\mathbf{B}_{RC}$ ) and tail currents ( $\mathbf{B}_T$ ) are determined by vector potentials that account for such factors such as day-night asymmetry, the geodipole tilt, and the finite thickness in the X and Y directions [Tsyganenko, 1995]. Previous research has shown that polar cusps shift towards the equator due to the Region 1 field-aligned current, which has a significant global effect [Donovan, 1993; Tsyganenko and Sibeck, 1994]. Thus, the most recent additions to this magnetospheric model are the magnetic field contributions from the Region 1 and 2 Birkeland currents ( $\mathbf{B}_{R1}$  &  $\mathbf{B}_{R2}$ ), which are fully described by Tsyganenko and Stern [1996]. Lastly, the contribution from the interconnection field ( $\mathbf{B}_I$ ) along the magnetopause boundary contributes non-zero normal components proportional to the IMF  $B_y$  and  $B_z$  components, which produces an open magnetospheric configuration [Dungey, 1961].

To bridge the gap between theory and observations, an extensive database was used to calibrate the T96 model. Tsyganenko's previous empirical models were limited to regions inside of the lunar orbit because Explorer 35 was locked in a Moon orbit [1987, 1989a]. The empirical T96 model uses a more extensive database from 11 satellites (Explorer 33 and 35, IMP 4, 5, 6, 7 and 8, Heos 1 and 2, and ISEE 1 and 2) covering the period 1966 to 1986 [Fairfield et al., 1994]. The caveat for the T96 model is that there are limitations in the predictive accuracy at higher altitudes. The empirical data set is significantly weighted by the amount of data collected (40%) from the ISEE 1 and 2 spacecraft, which orbit primarily at lower altitudes. An example of this shortcoming was investigated by Zhou et al. [1997] who found that generally the model

underdetermined the magnetic field values observed in the cusp region along Polar's orbit. Thus, there is lower predictive accuracy expected for this magnetospheric model at high altitude, which necessitates further investigation with the T01 model.

### *2.1.3 Description of the T01 model*

*Tsyganenko* further developed the magnetospheric model to include more realistic magnetic field values. The T01 magnetospheric model uses a deformation technique to determine the magnetic fields generated by the three major current systems: the ring current, the cross-tail current, and the Region 1 & 2 Birkeland currents, which are discussed below.

The ring current magnitude in the T96 and T01 models both track the corrected *Dst* index, but beyond that the T01 model includes two realistic improvements to the model ring current [*Tsyganenko, 2002a*]. Unlike the fixed radius of the ring current in the T96 model, the T01 model considers variations in the characteristic size of the ring current due to the penetration of energetic particles into the inner magnetosphere. Additionally, the ring current in the T01 model consists of two modules: the axially symmetric ring current (SRC) and the partial ring current (PRC). Asymmetry in the PRC results in larger plasma pressure and more depressed magnetic fields in the evening sector [*Liemohn et al., 2001*]. Thus, field-aligned currents are enhanced to divert the excess of azimuthal current from the duskside.

*Tsyganenko* uses previous research to describe the cross-tail current model [*Tsyganenko and Peredo, 1994; Tsyganenko, 1995, 1998*]. The deformation technique used in the T01 model generates warps along and across the cross-tail current sheet due to the dipole tilt. Magnetic field contributions are computed from multiple current sheets of varying current densities to generate the warping in cross-tail current sheet thickness and location [*Tsyganenko, 2002a and references therein*].

Previous models of the Birkeland Region 1 and 2 currents had only one variable parameter, the magnitude of the current [*Tsyganenko and Stern, 1996*]. In the T01 model an azimuthal current distribution affects the size of the Region 1 and 2 currents and the dipole tilt introduces an additional noon-midnight asymmetry [*Tsyganenko, 2002a*].

The T01 model is further improved by using a different data set for calibration and adding two input parameters. The new data set includes 9,573 records from the Geotail spacecraft from the period November 1994 to November 1999 and 28,351 records from the Polar spacecraft from the period March 1996 to August 1999. The addition of the Polar data set provides predictive accuracy at high altitudes, which plays a significant role in this thesis since the conclusions concentrate on these regions. The T01 model uses two additional inputs to parameterize the tail fields. The  $G_1$  parameter ( $G_1 = \langle V h(B_{\perp}) \sin^3(\theta/2) \rangle$ ) is based on the solar wind speed, the IMF transverse component, and the IMF clock angle. The  $G_2$  parameter ( $G_2 = a \langle V B_s \rangle$ ) is based on the solar wind speed and the southward component of the IMF. The second input parameter is also used to account for the effect of IMF electric fields on the Region 1 Birkeland current. Altogether these additions to the T01 model produce a more realistic magnetospheric

model that also yields better predictive accuracy in all near Earth magnetospheric regions.

#### *2.1.4 Description of the MHD model*

*Raeder et al.* developed a global magnetospheric model that solves the MHD equations throughout the volume surrounding the Earth [2001]. The volume of the global model extends from  $20 R_E$  to  $-300 R_E$  in  $X_{GSM}$  direction and to  $\pm 40 R_E$  in the  $Y_{GSM}$  and  $Z_{GSM}$  directions. The simulation domain extends from the bow shock to the magnetotail, and the numerical grid is a nonuniform rectangle with spatial resolution that reaches  $0.3 R_E$  near Earth and in the tail plasma sheet. The outer boundary is fixed by upstream solar wind conditions, and the inner boundary is given by an Earth centered shell with a radius of  $3.7 R_E$ . This placement of the inner boundary inhibits the formation of a ring current, and inside of the shell the MHD equations are replaced by a static dipole field [*Raeder*, 1999].

Input parameters for this model include solar wind speed, density, thermal pressure and IMF  $B_Y$  and  $B_Z$  components. For this examination speed and density values approximate solar wind conditions upstream and downstream of an interplanetary shock detected by Wind at 22:32 UT 10/12/00. IMF conditions are held fixed at  $B_Y = B_Z = 0$  nT, and the dipole is fixed perpendicular to the Earth-Sun line.

## 2.2 Standardized compression

In this section we discuss the results from the magnetospheric models that predict the global  $\Delta B$  response from a generic solar wind pressure front that compresses the magnetosphere. We approximate  $\Delta P_{dyn}$  associated with an interplanetary shock by using an upstream  $P_{dyn} = 1$  nPa and a downstream  $P_{dyn} = 4$  nPa to examine the change in a two state system. For each model the geomagnetic dipole tilt is fixed at zero (perpendicular to the Earth-Sun line) so the magnetospheric response in the Geocentric Solar Magnetospheric (GSM) coordinate system is symmetric about the equatorial plane. For the T96, T01, and MHD models, we use IMF components of  $B_Y = 0$  nT and  $B_Z = 0$  nT for both upstream and downstream conditions associated with the dynamic pressure front. These input parameters are fixed so that we examine magnetospheric changes in the magnetic field due solely to changes in the solar wind dynamic pressure, but the effects of the dipole tilt and IMF orientation are also discussed in Section 2.3.

The change in total magnetic field ( $\Delta B_T$ ) predicted by the *Tsyganenko* models are illustrated by a color scale that ranges from -30 nT to +30 nT. All the models predict a depression region above the cusps where magnetospheric compression generates a decrease in total magnetic field ( $-\Delta B_T$ ). This region is located at high altitudes on the dayside and it extends away from the noon-midnight meridian in symmetrical fashion, but the dimensions of the volume vary for each model. The T96 and T01 models predict additional small depression regions generated by the compression of localized current systems and the results for each model are discussed below.

### 2.2.1 Results from the T89 model

Illustrated in Figure 2.3 and 2.4 are the  $\Delta B$  predictions from the T89 model for a two state system that are equivalent to the upstream and downstream  $P_{dyn}$  values associated with a solar wind pressure front. Shown in Figure 2.3 are the  $\Delta B$  magnitudes along the noon-midnight meridian represented by a color scale that spans from -30 nT to +30 nT. This plane extends  $\pm 9 R_E$  in the  $X_{GSM}$  and  $Z_{GSM}$  directions and the data are linearly interpolated for spatial resolution of  $0.25 R_E$ . Shown in Figure 2.4 are the orthogonal Y-Z planes located at  $\pm 1 R_E$  and  $\pm 3 R_E X_{GSM}$ , which are denoted by dashed vertical lines in Figure 2.3. In the top row are the  $X_{GSM} = 1 R_E$  and  $X_{GSM} = 3 R_E$  planes and in the bottom row are the  $X_{GSM} = -1 R_E$  and  $X_{GSM} = -3 R_E$  planes.

Depicted in blue are regions where a decrease in total magnetic field ( $-\Delta B$ ) results from an increase in solar wind dynamic pressure. These depression regions located at high altitudes on the dayside are a result of magnetic field perturbations that are anti-parallel to the background field around the polar cusps. Along the equator, magnetic field perturbations are aligned northward with the Earth's field thereby resulting in an amplification of the background field, particularly on the dayside. In closer proximity to the magnetopause boundary northward field perturbations are larger, thus  $-\Delta B$  magnitudes are magnified at high altitudes and  $+\Delta B$  magnitudes are largest near the subsolar point. The orthogonal planes illustrated in Figure 2.4 depict the width of the depression region, which is not only symmetric to the noon-midnight meridian, but it also extends to distances of  $\pm 2 R_E$  in the  $Y_{GSM}$  direction. At higher altitudes the depression

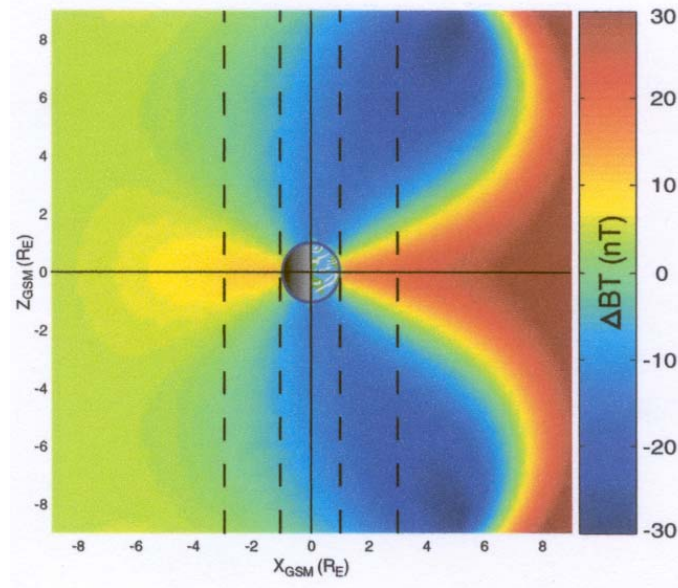


Figure 2.3: T89 model predictions when  $P_{dyn}$  increases from 1 nPa to 4 nPa. Representing  $\Delta B$  values along the noon-midnight meridian are color contours spanning from -30 nT to +30 nT. The plane extends  $\pm 9 R_E$  in the  $X_{GSM}$  and  $Z_{GSM}$  directions. Vertical dashed lines indicate the locations of orthogonal planes displayed in Figure 2.4. The Sun is on the right.

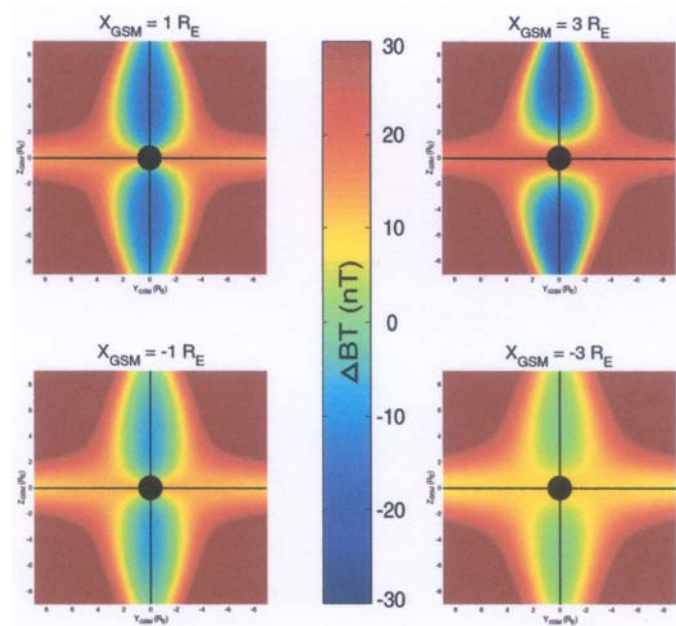


Figure 2.4: T89 model predictions when  $P_{dyn}$  increases from 1 nPa to 4 nPa. Orthogonal Y-Z planes correspond to the dashed lines in Figure 2.3 and they extend  $\pm 9 R_E$  in both directions. Top left and right panels are located at  $X_{GSM} = 1 R_E$  and  $X_{GSM} = 3 R_E$ , respectively. Bottom left and right panels are located at  $X_{GSM} = -1 R_E$  and  $X_{GSM} = -3 R_E$ , respectively. The same color scale applies to these illustrations.

region tapers down to  $\pm 1 R_E$  in similar fashion to the cross section of a teardrop. The depression region is primarily on the dayside, but the volume extends far enough tailward to be seen as small  $-\Delta B$  values in the  $X_{GSM} = -1 R_E$  plane (bottom-left panel, Figure 2.4).

### *2.2.2 Results from T96 model*

Illustrated in Figure 2.5 and 2.6 are the  $\Delta B$  predictions from the T96 model for a two state system that mimics a step-function increase in solar wind dynamic pressure from 1 nPa to 4 nPa. The plots are displayed in the same manner as the previous section and the  $\Delta B$  magnitudes are represented by the same color scale that spans from -30 nT to +30 nT.

The global response for the T96 model is different from the T89 model, but the most significant feature in common is the depression region predicted at high altitude on the dayside. This depression region is smaller in magnitude ( $\Delta B > -20$  nT) and volume as shown in Figures 2.5 and 2.6. The high altitude depression region is not visible in the  $X_{GSM} = 1 R_E$  plane (top-left, Figure 2.6), but small decreases ( $-\Delta B \sim -5$  nT to  $-10$  nT) are present in the  $X_{GSM} = 3 R_E$  plane (top-right, Figure 2.6), which extend symmetrically away from the noon-midnight meridian to distances of  $\pm 4 R_E Y_{GSM}$ . Similar to the T89 model, this depression region predicted by the T96 model is due to the compression of the magnetopause current, which has been repositioned Earthward due to the downstream solar wind dynamic pressure.

The T96 model also predicts an additional depression region along the equator,

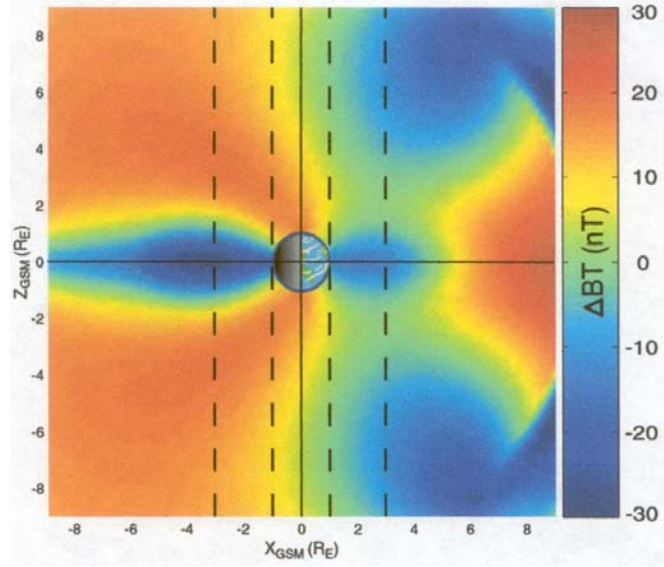


Figure 2.5: T96 predictions along the noon-midnight meridian when  $P_{dyn}$  increases from 1 nPa to 4 nPa. The color scale and spatial dimensions are the same as presented in Figure 2.3.

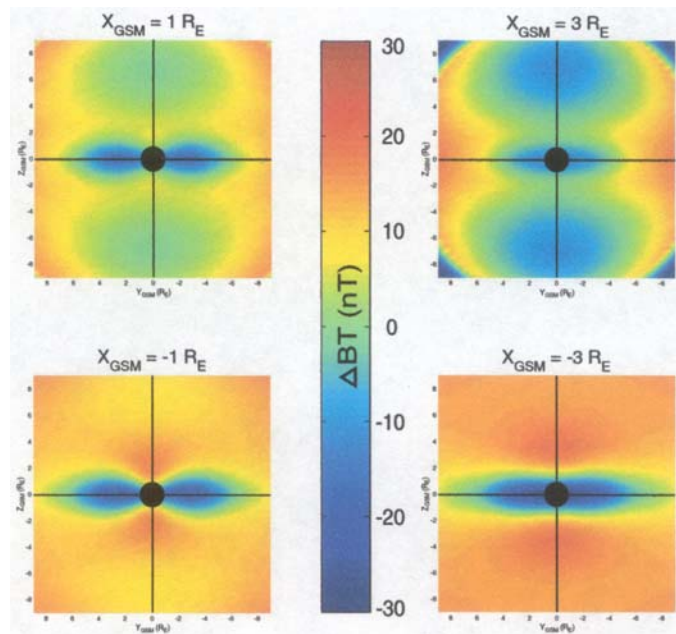


Figure 2.6: T96 model predictions when  $P_{dyn}$  increases from 1 nPa to 4 nPa. Orthogonal Y-Z planes correspond to the dashed lines in Figure 2.5. This figure is presented in the same format as Figure 2.4.

which results from compression of local current systems that are present in the T96 model (see Section 2.1.2). From Figures 2.5 and 2.6 we see that this depression region encircles the Earth from near the surface to a radial distance of  $\sim 4 R_E$  on the dawn and dusk flanks, as well as the dayside. This feature is generated by the compression of the westward ring current, but there is a day-night asymmetry because of additional field perturbations on the nightside. Compression of the dawn-to-dusk cross-tail current amplifies the magnitude of the nightside depression region, which flares to altitudes of  $\pm 2 R_E Z_{GSM}$  before tapering back to the equatorial plane near  $X_{GSM} \sim -9 R_E$ . The combined effect of the two compressed currents generates a region of  $-\Delta B$  to a magnitude of  $\sim -30$  nT, which are a result of field perturbations that are anti-parallel to the background field along the equator.

### *2.2.3 Results from T01 model*

Illustrated in Figure 2.7 and 2.8 are the  $\Delta B$  predictions from the T01 model due to a step-function increase in solar wind dynamic pressure from 1 nPa to 4 nPa. The plots are displayed in the same manner as the previous sections and the  $\Delta B$  magnitudes are represented by the same color scale that spans from -30 nT to +30 nT.

The global response for the T01 model is mostly similar to the results presented for the T96 model, and the most important feature predicted by the T89 and T96 models is also replicated here, the dayside depression region. Throughout the high altitude depression region the decreases in field strength are similar to the predictions from the

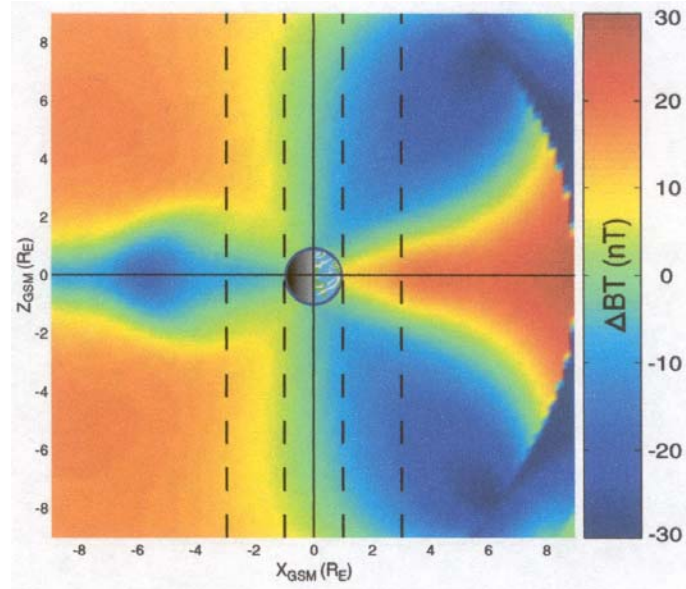


Figure 2.7: T01 predictions along the noon-midnight meridian when  $P_{dyn}$  increases from 1 nPa to 4 nPa. The color scale and spatial dimensions are the same as presented in Figures 2.3 and 2.5.

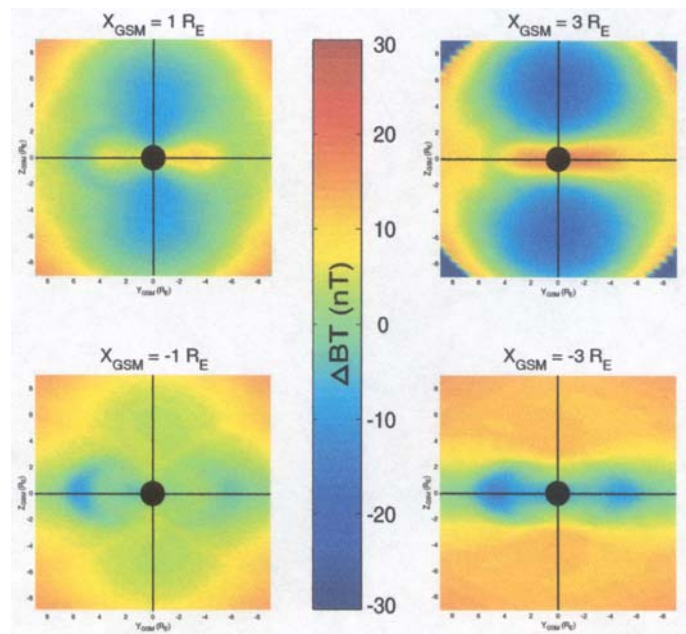


Figure 2.8: T01 model predictions when  $P_{dyn}$  increases from 1 nPa to 4 nPa. Orthogonal Y-Z planes correspond to the dashed lines in Figure 2.7. This figure is presented in the same format as Figures 2.4 and 2.6.

T96 model, but the T01 model predicts a larger spatial volume. Shown in the top-right panel of Figure 2.8 is a cross section of the high altitude depression region at  $X_{\text{GSM}} = 3 R_E$ , which extends  $\pm 5 R_E Y_{\text{GSM}}$  from the noon-midnight meridian and down to altitudes of  $\pm 2 R_E Z_{\text{GSM}}$ . The cross-section of the depression region predicted by the T01 model is larger than predicted by the T96 model (top right, Figure 2.6), and the field decreases are also greater in magnitude ( $-\Delta B \sim -10\text{nT}$  to  $-20\text{ nT}$ ) than the T96 model. The size of the high altitude depression region is one difference between the T96 and T01 models but there is also a difference in the structure of the equatorial depression region.

The T01 model predicts an additional depression region along the equator due to compression of local current systems, but the structure of this region varies from the predictions in the T96 model. Figure 2.7 illustrates a nightside depression region, but unlike the T96 model this region does not encircle the Earth. In the T01 model the partial ring current is diverted into the Region 1 Birkeland current thereby reducing field perturbations from the ring current. The absence of field perturbations from the ring current is most apparent on the dayside equator in Figure 2.7 (see also  $X_{\text{GSM}} = 3 R_E$  plane, top-right panel of Figure 2.8). Previously, the T96 model predicted a dayside depression region along the equator, but the correction for the partial ring current in the T01 model determines the correct magnetospheric response in this region. The partial ring current also introduces a dawn-dusk asymmetry (all panels, Figure 2.8) in the magnetic field changes due to weaker background fields in the evening sector.

#### 2.2.4 Standardized compression with MHD model

Illustrated in Figure 2.9 and 2.10 are the global  $\Delta B$  predictions from the MHD model, which result from a step-function increase in solar wind dynamic pressure from 1 nPa to 4 nPa. This pressure change is determined by increasing proton number density from  $5 \text{ cm}^{-3}$  to  $12 \text{ cm}^{-3}$  and solar wind speed 350 km/s to 450 km/s. All other solar wind inputs were kept at constant values to examine the magnetospheric response from only a dynamic pressure change. The dipole tilt was fixed at zero and the shock front was oriented such that the shock normal was parallel to the Earth-Sun line. The magnetic field changes are presented numerically as overlays on the T96 color plots. North-South symmetry is assumed for the  $\Delta B$  values presented. In Figure 2.9 *in situ*  $\Delta B$  values along the noon-midnight meridian are presented in spatial intervals of  $2 R_E$  for  $X_{\text{GSM}} = \pm 9 R_E$  and  $1 R_E$  for  $Z_{\text{GSM}}$  from  $1 R_E$  to  $9 R_E$ , excluding  $Z_{\text{GSM}} = 2 R_E$ . In Figure 2.10 the MHD results are plotted as overlays on the Y-Z planes at  $Y_{\text{GSM}}$  intervals of 0,  $\pm 1$ ,  $\pm 3$ , and  $\pm 5 R_E$ .

The MHD model predicts a high altitude depression on the dayside, which is consistent with all the previous models discussed. Presented in Figure 2.9 are the  $\Delta B$  values along the noon-midnight meridian. The  $-\Delta B$  magnitudes are consistent with the T96 model, although they extend to a larger volume that is more consistent with the T01 model. Decreases in field strength are predicted at high altitudes on the dayside in roughly a teardrop shape similar to the previous model results. There is an additional decrease in magnetic field on the nightside equator, which is consistent with both the T96

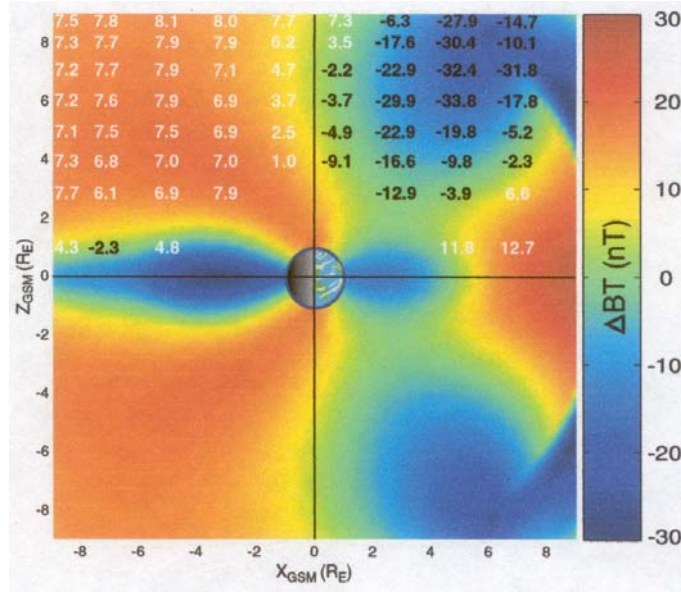


Figure 2.9: Predictions from the MHD model when dynamic pressure increases from 1 nPa to 4 nPa.  $\Delta B$  predictions along the noon-midnight meridian are presented as numerical overlays on Figure 2.3.

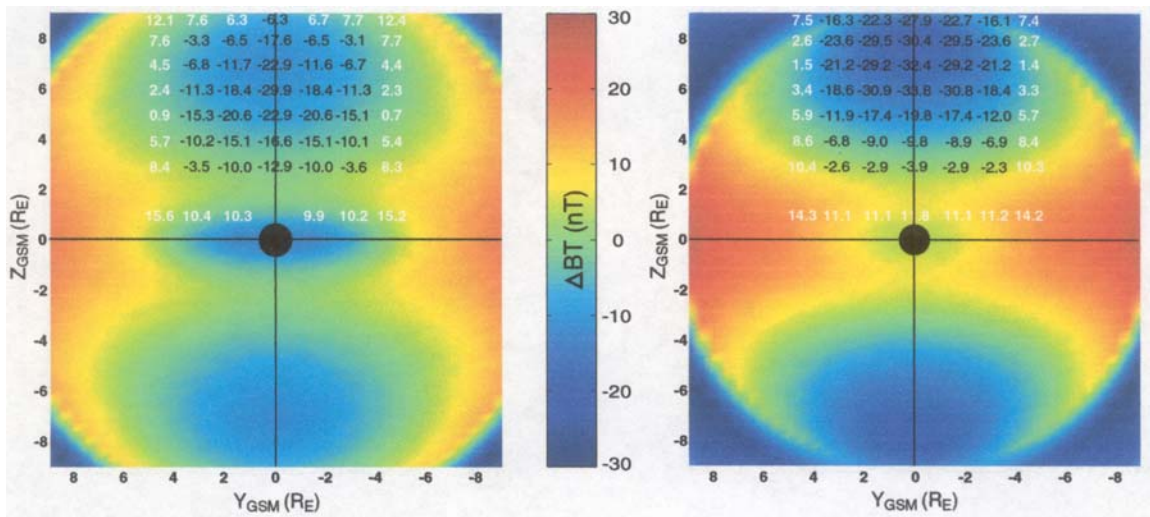


Figure 2.10: Predictions from the MHD model when dynamic pressure increases from 1 nPa to 4 nPa. The  $\Delta B$  values in the Y-Z planes are presented as numerical overlays on color contour plots predicted by the T96 model for the same solar wind conditions. The left panel is the Y-Z plane located at  $X_{GSM} = 3 R_E$  plane and the right panel is the Y-Z plane located at  $X_{GSM} = 5 R_E$ .

and T01 models. The T96 model is used for the overlay to confirm any MHD prediction of the dayside depression region at the equator. However, the MHD model does not

predict this particular depression region, which is more consistent with the T01 model. Shown in Figure 2.10 are the  $-\Delta B$  values at the  $3 R_E$  and  $5 R_E X_{GSM}$  planes, which are consistent in magnitude and location with the T96 model. The results in Figures 2.10 illustrate the width of the depression region, which extends to  $Y_{GSM} = \pm 3 R_E$  away from the noon-midnight meridian.

### *2.2.5 Summary of results*

All of the models discussed above predict a depression region at high altitudes on the dayside where the magnetic field decreases as a result of an increase in solar wind dynamic pressure. This phenomenon is a result of a compressed magnetopause current that generates magnetic field perturbations anti-parallel to the background field. The more sophisticated models predict additional decreases in field strength along the equator due to compression of local currents. These models are used to provide a global picture of the magnetospheric response, which is the framework for investigating the comparison with observational results in Chapter 3.

## **2.3 Varying other input parameters**

The results discussed above use solar wind dynamic pressure as the only input parameter for the models so that this parameter can be examined exclusively for its impact on the magnetospheric response. In reality there are other parameters that also

have an effect on the global response of the magnetosphere. The dipole tilt is one such parameter that can be altered in all the models, and the IMF orientation is another parameter that can be varied in the T96 and T01 models. This section is an investigation of the effects from altering these parameters in conjunction with the standardized compression where dynamic pressure is increase from 1 nPa to 4 nPa.

In Figure 2.11 are plots of  $\Delta B$  changes along noon-midnight meridian that are determined by the T96 model where the dipole tilt is fixed at  $-20^\circ$  or  $+20^\circ$ . These two plots are essentially the same as the results discussed in Section 2.2.2, except that there is a noticeable relocation of the depression regions. In the left panel of Figure 2.11 the

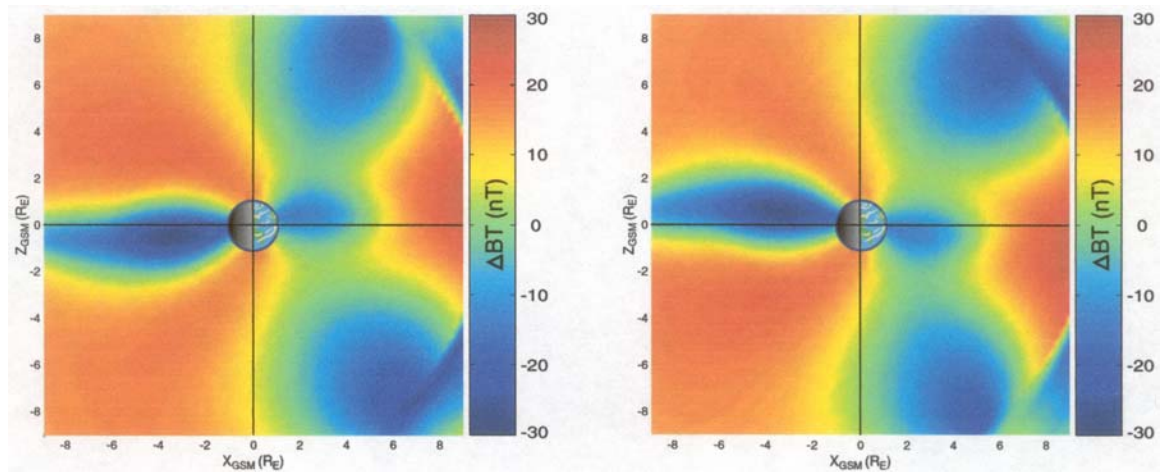


Figure 2.11: Predictions by the T96 model along the noon-midnight meridian. In addition to an increase in  $P_{dyn}$ , dipole tilt is also used as an input parameter. The dipole tilt is fixed at  $-20^\circ$  in the left panel and  $+20^\circ$  in the right panel.

dipole is fixed at  $-20^\circ$ , which shifts the southern depression region slightly Sunward and the northern depression lobe is shifted tailward. In the right panel of Figure 2.11 the dipole is fixed at  $+20^\circ$ , which shifts the northern depression region slightly Sunward and

the southern depression lobe is shifted tailward. The two panels in Figure 2.11 are essentially a reflection of each other about the equatorial plane, but the size of the depression region and the magnitude of the global  $\Delta B$  responses are consistent with the results presented in Figure 2.5. This same behavior was observed when the fixed dipole tilt was applied to the standardized compression of the T89 and T01 models. The only noticeable affect of the dipole tilt is to cause a shift in the location of the depression region, but the presence of  $-\Delta B$  regions persists.

The IMF orientation is used as an additional input parameter when the standardized compression is applied to the T96 model. Shown in Figure 2.12 are  $\Delta B$  predictions along the noon-midnight meridian when the IMF is fixed at  $-10$  nT  $Z_{GSM}$  and  $P_{dyn}$  increases from 1 nPa to 4 nPa. The global response presented is essentially the same

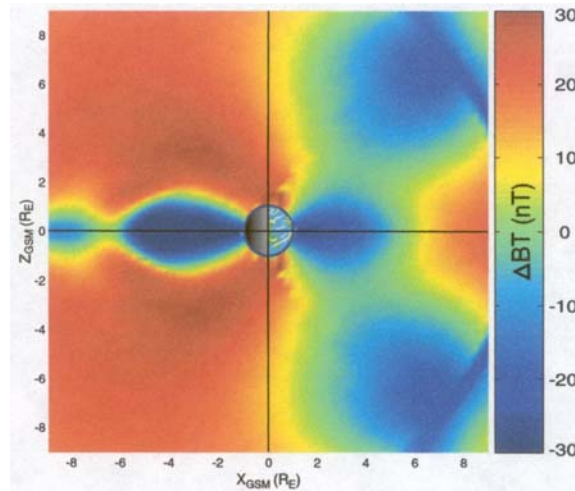


Figure 2.12: Predictions by the T96 model along the noon-midnight meridian.  $P_{dyn}$  increases from 1 nPa to 4 nPa during a fixed southward IMF ( $B_Z = -10$  nT).

as the case discussed in Section 2.2.2 where no IMF parameter is used, except there is a noticeable intensification  $\Delta B$  values on the nightside. The compressed ring current is further amplified when a southward IMF convects magnetospheric plasma Earthward. We find that the amplified current generates  $\Delta B \sim -30$  nT in the nightside depression region and at altitudes up to  $Z_{\text{GSM}} = \pm 4 R_E$  we find  $\Delta B \sim +25-30$  nT. Similar cases were tested with an IMF fixed with a northward orientation ( $+10$  nT  $Z_{\text{GSM}}$ ). In addition, we used an eastward and westward IMF orientation ( $\pm 10$  nT  $Y_{\text{GSM}}$ ). The global response for all three of these scenarios are essentially the same as the standardized compression shown in Figure 2.5, thus these cases are not presented. Only a southward IMF has an impact on the global response of the magnetosphere under compression, and the depression region will still be generated by the change in solar wind dynamic pressure.

Another scenario was tested with both additional input parameters, so dipole tilt was fixed at  $+20^\circ$  and a steady IMF of  $-10$  nT  $Z_{\text{GSM}}$  was applied in conjunction with the change in solar wind dynamic pressure. Shown in Figure 2.13 are the global  $\Delta B$  values predicted with the T96 model when all three input parameters are used. The magnitude of the global response is nearly identical to the results presented in Figure 2.12, except that the dipole tilt has also shifted the depression regions in the same manner as presented in Figure 2.11 (right panel). This examination has shown that IMF orientation and dipole tilt both affect the global response of the magnetosphere under compression. However, regardless of the additional solar wind parameter, the depression region is generated solely by the dynamic pressure change in the solar wind. Similar changes in the magnetospheric response were predicted by the T89 and T01 models when the same

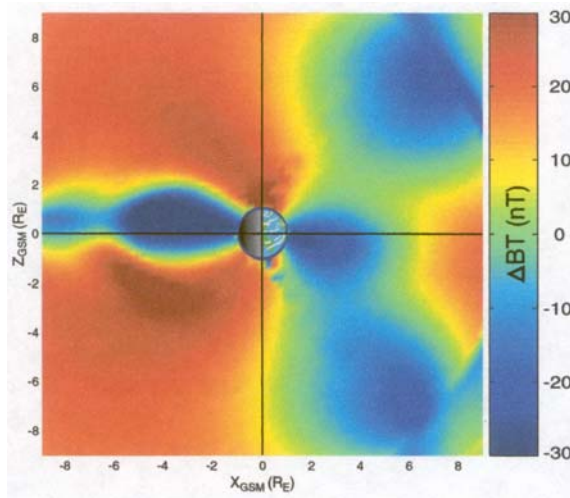


Figure 2.13: Predictions from the T96 model along the noon-midnight meridian.  $P_{dyn}$  increases from 1 nPa to 4 nPa, dipole tilt fixed at  $+20^\circ$ , and IMF is fixed southward ( $B_z = -10$  nT).

fixed input parameters were applied. As before, there are  $-\Delta B$  region persists with some spatial variations, but the results are not presented for brevity.

## 2.4 Summary and Conclusions

In this chapter we consider several potential physical models to explain the physics of the magnetospheric response to a sudden change in solar wind dynamic pressure. To accomplish this task we examine the predicted global magnetospheric response from three *Tsyganenko* models and an MHD model when we apply a step function increase in dynamic pressure. We simulate the passage of a pressure front that interacts with the magnetosphere by using input parameters of 1 nPa and 4 nPa as upstream and downstream dynamic pressure, respectively. This qualitative analysis with

the models provides a theoretical basis for the quantitative analysis presented in the next chapter, which compares model predictions to *in situ* spacecraft observations of  $\Delta B$ .

All the models predict a high altitude depression region on the dayside where the magnetic field decreases ( $-\Delta B$ ) as a result of magnetospheric compression. We found the volume of the depression region extending symmetrically away from the noon-midnight meridian (Figures 2.4, 2.6 and 2.8). Reductions in  $B_T$  along dayside polar field lines result from the compressed magnetopause perturbations that are anti-parallel to the background field. Although all the models predict the dayside depression region, the volume and  $-\Delta B$  magnitude of the region vary between the models. The T96, T01 and MHD models also predict that a nightside depression region develops in the equatorial plane due to compression of the cross-tail current. Further, we found that the T96 model predicts an additional depression region that encircles the Earth, which is a result of the compressed ring current. This feature is not present because the T01 model uses a partial ring current that does not generate the circular depression region. An examination with the standardized models illustrates the possible  $\Delta B$  response throughout the volume of the magnetosphere. In the following chapter we use observational evidence to verify the most accurate representation of the magnetospheric response. Already we see the relevance this thesis work because the physical models illustrate interesting results in regions away from the equator and on the nightside, which were not addressed in the *Araki* model.

We also examined the model predictions when other input parameters are used in conjunction with the dynamic pressure change. We find that tilting the dipole shifts the

location of the high altitude depression regions either Sunward or tailward, but the depression region does not disappear. When we apply a steady southward IMF the size and magnitude of the depression regions vary, but remain present. We must realize that using standardized input parameters provides an idealized physical model. So in the next chapter we use all available input parameters for each model, and we expect to see *in situ*  $-\Delta B$  predictions by the models. Ultimately the dynamic pressure changes drive the magnetic field response, but we will find that using the full compliment of input parameters will quantitatively and statistically reinforce our determination of the most accurate physical model of magnetospheric compression.

## 2.5 References

Alexseev, I. I., and V. P. Shabansky, A model of magnetic field in the geomagnetosphere, *Planet. Space Sci.*, 20, 117, 1972.

Araki, T., A physical model of the geomagnetic sudden commencement, *Solar Wind Sources of Magnetospheric Ultra-Low-Frequency Waves, Geophysical Monograph*, 81, 183-200, 1994.

Choe, Y. J., D. B. Beard, and E. C. Sullivan, Precise calculation of the magnetosphere surface for a tilted dipole, *Planet. Space Sci.*, 21, 485, 1973.

Dungey, J. W., Interplanetary magnetic field and the auroral zones, *Phys. Rev. Lett.*, 6, 47, 1961.

Fairfield, D. H., N. A. Tsyganenko, A. V. Usmanov, and M. V. Malkov, A large magnetosphere magnetic field database, *J. Geophys. Res.*, 99, 11,319-11,326, 1994.

Fuller-Rowell, T. J., D. Reese, S. Quegan, R. J. Moffett, M. V. Codrescu, and G. H. Millward, A coupled thermosphere-ionosphere model (CTIM), in *STEP Report*, ed. R. Schunk, Scientific Committee on Solar Terrestrial Physics (SCOSTEP), NOAA/NGDC, Boulder, Co., 217, 1996.

Halderson, D. W., D. B. Beard, and J. Y. Choe, Correction to "The compressed geomagnetic field as a function of dipole tilt", *Planet. Space Sci.*, 23, 887, 1975.

Liemohn, M. W., J. U. Kozyra, M. F. Thompsen, J. L. Roeder, G. Lu, J. E. Borovsky, and T. E. Cayton, Dominant role of the asymmetric ring current in producing the stormtime *Dst\**, *J. Geophys. Res.*, 106, 10.883, 2001.

Mead, G. D. and D. B. Beard, Shape of the geomagnetic field-solar wind boundary, *J. Geophys. Res.*, 69, 1169, 1964.

Mead, G. D. and D. H. Fairfield, A quantitative magnetospheric model derived from spacecraft magnetometer data, *J. Geophys. Res.*, 80, 523-534, 1975.

Petrenic, S. M. and C. T. Russell, An empirical model of the size and shape of the near-Earth magnetotail, *Geophys. Res. Lett.*, 20, 2695-2698, 1993.

Raeder, J., Modeling the magnetosphere for northward interplanetary magnetic field: Effects of electrical resistivity, *J. Geophys. Res.*, 104, 17-357, 1999.

- Raeder, J, Y. L. Wang, and T. J. Fuller-Rowell, Geomagnetic storm simulation with a coupled magnetosphere-ionosphere-thermosphere model, in *Space Weather*, ed. P. Song, H. Singer, and G. Siscoe, Geophysical Monograph Series, Vol. 125, 2001.
- Sibeck, D. G., R. E. Lopez, and E. C. Roelof, Solar wind control of the magnetopause shape, location, and motion, *J. Geophys. Res.*, 96, 5489-5495, 1991.
- Tsyganenko, N. A. and A. V. Usmanov, Determination of the magnetospheric current system parameters and development of experimental geomagnetic field models based on data from IMP and HEOS satellites, *Planet. Space Sci.*, 30, 985-998, 1982.
- Tsyganenko, N. A., A magnetospheric magnetic field model with a warped tail current sheet, *Planet. Space Sci.*, 37, 5-20, 1989a.
- Tsyganenko, N. A., A solution of the Chapman-Ferraro problem for an ellipsoidal magnetopause, *Planet. Space Sci.*, 37, 1037-1046, 1989b.
- Tsyganenko, N. A., Methods for quantitative modeling of the magnetic field from Birkeland currents, *Planet. Space Sci.*, 39, 641, 1991.
- Tsyganenko, N. A. and M. Peredo, Analytical models of the magnetic field of disk-shaped current sheets, *J. Geophys. Res.*, 99, 199, 1994.
- Tsyganenko, N. A. and D. G. Sibeck, Concerning flux erosion from the dayside magnetosphere, *J. Geophys. Res.*, 99, 13,425-13,436, 1994.
- Tsyganenko, N. A., Modeling the Earth's magnetospheric magnetic field confined within a realistic magnetopause, *J. Geophys. Res.*, 100, 5,599-5,612, 1995.
- Tsyganenko, N. A., Effects of the solar wind conditions on the global magnetospheric configuration as deduced from data-based field models, *Third International Conference on Substorms (ICS-3)*, 181-185, 1996.
- Tsyganenko, N. A. and D. P. Stern, Modeling the global magnetic field of the large-scale Birkeland current systems, *J. Geophys. Res.*, 101, 27,187-27,198, 1996.
- Tsyganenko, N. A., Modeling of twisted/warped magnetospheric configurations using the general deformation method, *J. Geophys. Res.*, 103, 23,551, 1998.
- Tsyganenko, N. A., A model of the near magnetosphere with a dawn-dusk, asymmetry 1. Mathematical structure, *J. Geophys. Res.*, 10.1029/2001JA000219, SMP 10-1, 2002a.

Tsyganenko, N. A., A model of the near magnetosphere with a dawn-dusk asymmetry 2. Parameterization and fitting to observations, *J. Geophys. Res.*, 10.1029/2001JA000220, SMP 10-2, 2002b.

Zhou, X. -W., C. T. Russell, G. Le, and N. Tsyganenko, Comparison of observed and model magnetic fields at high altitudes above the polar cap: Polar initial results, *Geophys. Res. Lett.*, 24, 1451-1454, 1997.

## Chapter 3: Comparison of Observations to Models

### 3.1 Introduction

In this chapter we qualitatively analyze magnetospheric compression by comparing spacecraft observations of SIs to model predictions of the phenomenon. In the previous chapter we determined that the models predict decreases in total magnetic field at high altitudes on the dayside when a dynamic pressure front in the solar wind encounters the geo-magnetosphere. This discovery is confirmed with magnetometer measurements by Polar MFE observations of  $-\Delta B$  in this region. We use numerical comparisons between observations and models to verify the three dimensional physical models of magnetospheric compression presented in the previous chapter.

We begin our analysis by assessing the reasonableness of  $\Delta B$  measurements from Polar and GOES by using the standardized model results presented in the previous chapter (Figures 2.4, 2.6, and 2.8) to qualitatively analyze the global magnetospheric response. The modeled response is fairly generic because the simulated pressure front only approximates actual solar wind conditions. Therefore, we use solar wind plasma and magnetic field measurements from the Wind spacecraft as model inputs to replicate SIs observed by Polar and GOES. Then we use a quantitative analysis of the numerical results and we find the T01 model most accurately replicates reality. The predictive accuracy of the T01 model confirms the three dimensional physical model of magnetospheric compression presented in the previous chapter.

In the previous chapter we found that compression of local magnetospheric currents generates depression regions throughout the magnetosphere. With the numerical analysis we find that the T89 model accurately predicts SIs observed at high altitudes, but there are inconsistencies in the equatorial plane because the model lacks a tail current. So, we use modified versions of the T96 model where magnetic field contributions from specific current systems are removed individually and jointly to investigate the relative impact of each current system on the global  $\Delta B$  response. At high altitudes we find no significant  $\Delta B$  contribution from compression of the Birkeland currents, ring current, or tail current. We conclude that the compressed tail current is necessary to generate the nightside depression region at the equator.

Polar measurements of  $\Delta B$  throughout the geo-magnetosphere are compared with changes in solar wind dynamic pressure measured by Wind. The ratio ( $\Delta B/\Delta p^{1/2}$ ) is used to parameterize the magnetospheric response. We find that response ratios at high altitudes are consistent with previously determined ratios from other magnetospheric research. We also find that the response ratio is spatially dependent where the largest values are found on the dayside during northward IMF.

### **3.2 Qualitative Verification of the Standardized Compression**

When the magnetosphere is compressed there are decreases in total magnetic field detected *in situ* by Polar and GOES, which confirm the depression regions predicted by the *Tsyganenko* models. Graphical presentations are used for comparisons with

spacecraft observations, which provide the background for a more quantitative analysis in the following section. Illustrated in Figure 3.1 are  $\Delta B$  responses along the noon-midnight meridian predicted by the three *Tsyganenko* models when a standardized change in solar

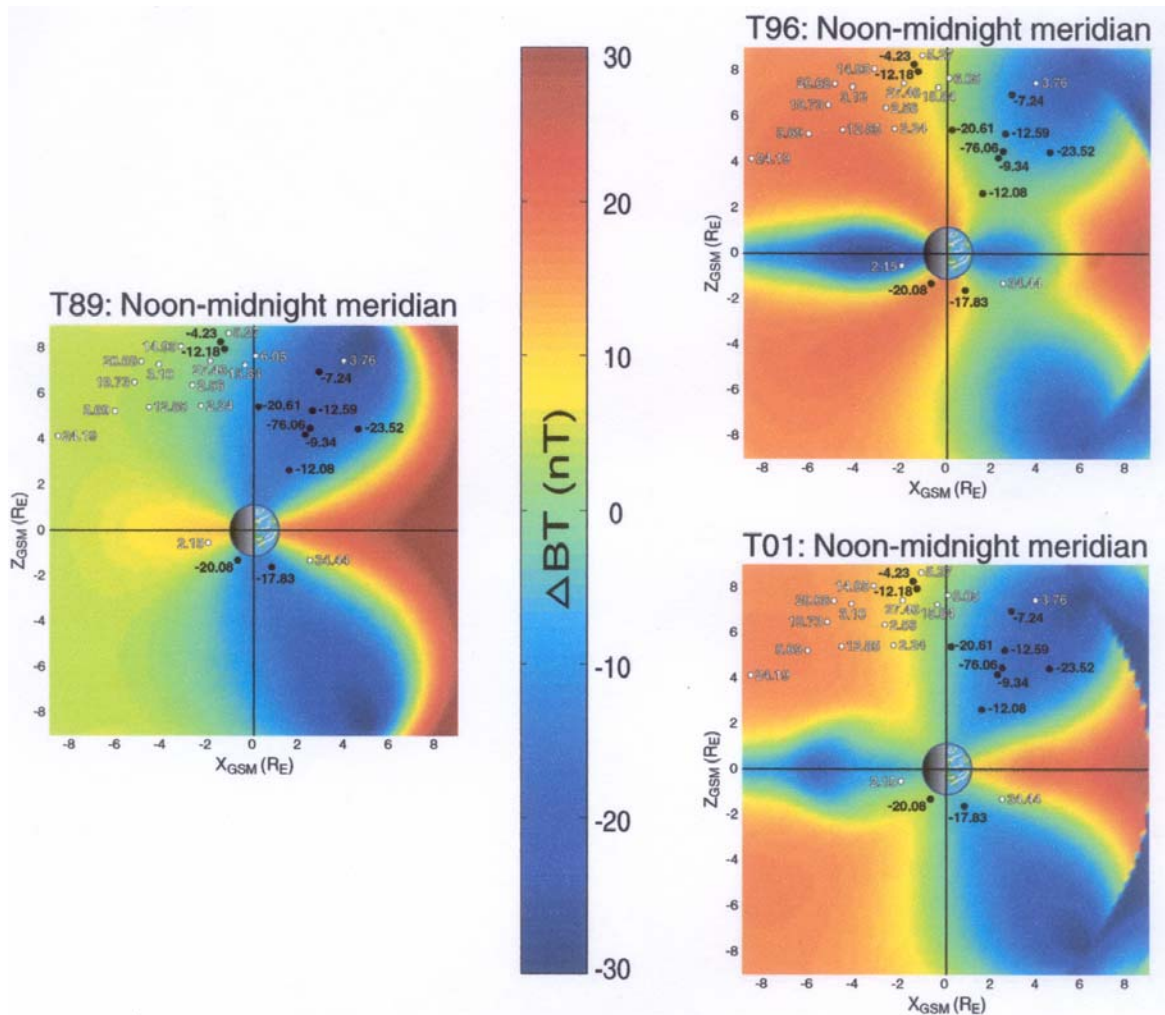


Figure 3.1:  $\Delta B$  predictions from the standardized compression of the *Tsyganenko* models. Projected onto the noon-midnight meridian plots are the Polar observations located within  $\pm 1 R_E$  of the plane.  $-\Delta B$  observations are displayed in black. We apply the same spatial format and color scale as seen in Figures 2.3, 2.5 and 2.7.

wind dynamic pressure is applied. The  $\Delta B$  magnitudes of SIs measured by Polar within  $\pm 1 R_E Y_{GSM}$  of the noon-midnight meridian have been projected onto these planes. The

values in black represent  $-\Delta B$  observations and the values in white represent  $+\Delta B$  observations. Solar wind parameters such as IMF orientation and dipole tilt are unique for each observed SI and the color background represents a standardized compression, so we do not expect the color to correspond to any one particular observations. In fact, the dipole tilt is responsible for all contradictions where  $-\Delta B$  observations occur outside of the high altitude depression region and  $+\Delta B$  observations occur inside the standardized depression region. This graphical presentation is meant to provide a general guide for the magnetospheric response, which sets precedence for the statistical analysis in the following section.

We make similar comparisons with  $\Delta B$  measurements by the GOES 8, 9, and 10 spacecraft from the same event pool of interplanetary shocks that triggered the SIs observed by Polar. The GOES spacecraft are in geosynchronous orbit along the equatorial plane, which is not well sampled by Polar (see Figure 1.8). Figures 3.2 – 3.4 show  $\Delta B$  magnitudes observed *in situ* by GOES which are projected onto color plots of the standardized compressional event from the *Tsyganenko* models. These figures are presented in four planes: along the noon-midnight meridian (top left), along the equatorial plane (top right), and the X-Y planes at  $Z_{\text{GSM}}$  altitudes of 1 and 2  $R_E$  (bottom left and bottom right, respectively). Since the *Tsyganenko* results are symmetric about the equatorial plane, GOES measurements projected onto the  $Z_{\text{GSM}}$  planes are located within  $\pm 0.5 R_E$  of either the Northern or Southern plane. These comparisons illustrate the predictive accuracy of the *Tsyganenko* models in near proximity to the equatorial region. In Figure 3.2, the  $+\Delta B$  observations on the dayside of the magnetosphere agree with the

T89 model results. The T89 model does not predict a nightside depression region, which conflicts with the  $-\Delta B$  measurements seen at different altitudes. In Figures 3.3 and 3.4 the T96 and T01 models predict a nightside depression region generated by magnetic field perturbations from the compressed tail current, and the T96 includes an additional

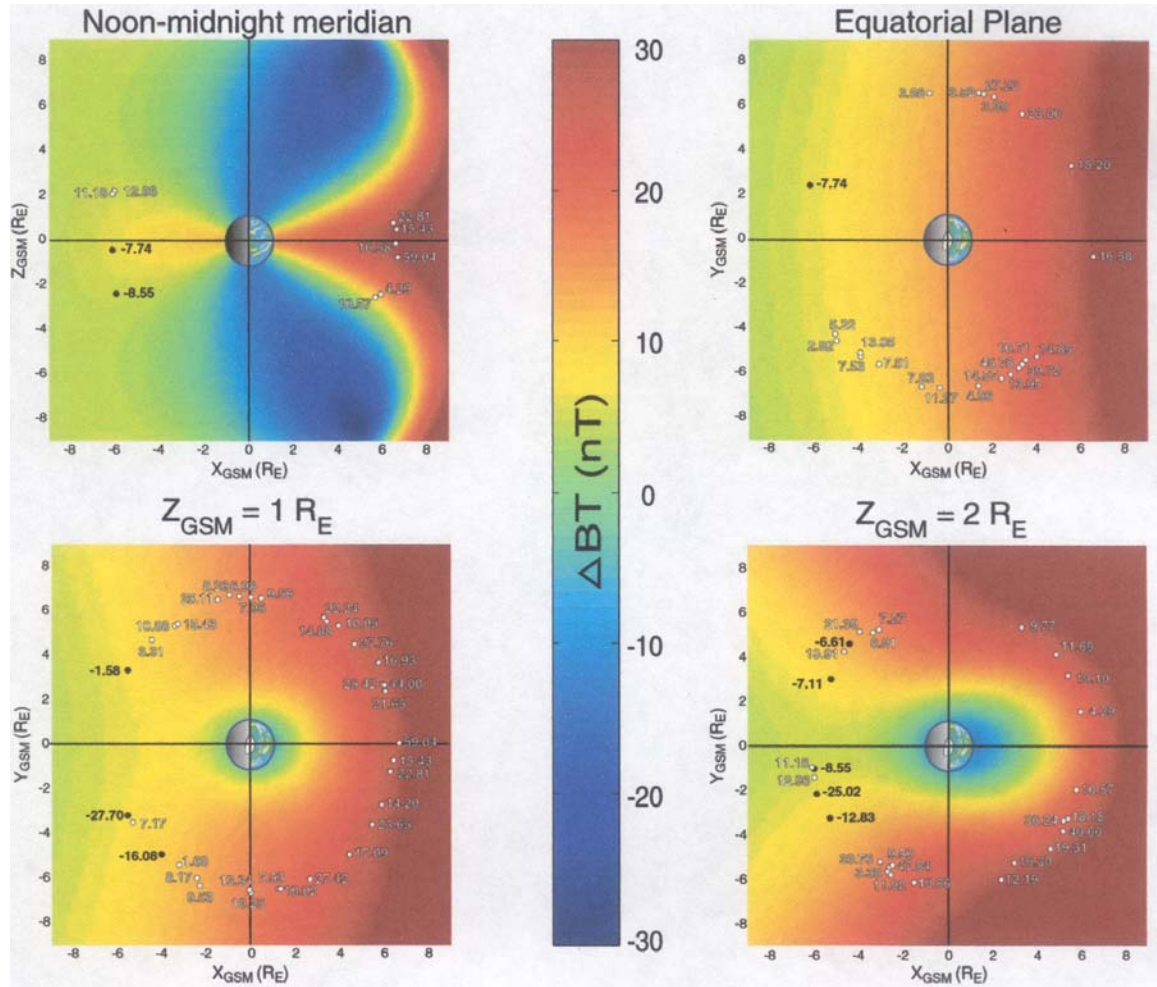


Figure 3.2: Contour plots of  $\Delta B$  predictions by the T89 model along the noon-midnight meridian and X-Y planes at three  $Z_{GSM}$  altitudes. Projected onto the noon-midnight meridian are  $\Delta B$  measurements observed by GOES 8, 9, and 10 spacecraft at locations within  $\pm 1 R_E$  of the plane (top left panel). GOES observations are also projected onto the equatorial plane (top right panel). There is north-south symmetry in the model predictions. Any observations within  $\pm 0.5 R_E$  of either  $Z_{GSM} = \pm 1 R_E$  planes are displayed in the bottom left panel. Any observations with  $\pm 0.5 R_E$  of either  $Z_{GSM} = \pm 2 R_E$  planes are displayed in the bottom right panel.

contribution from ring current compression. The GOES spacecraft detect  $-\Delta B$  compressional signals on the nightside in near proximity to the predicted nightside depression region. All  $-\Delta B$  measurements at higher altitude are due to the effect of the dipole tilt, which is not considered in the model results. At all altitudes on the dayside

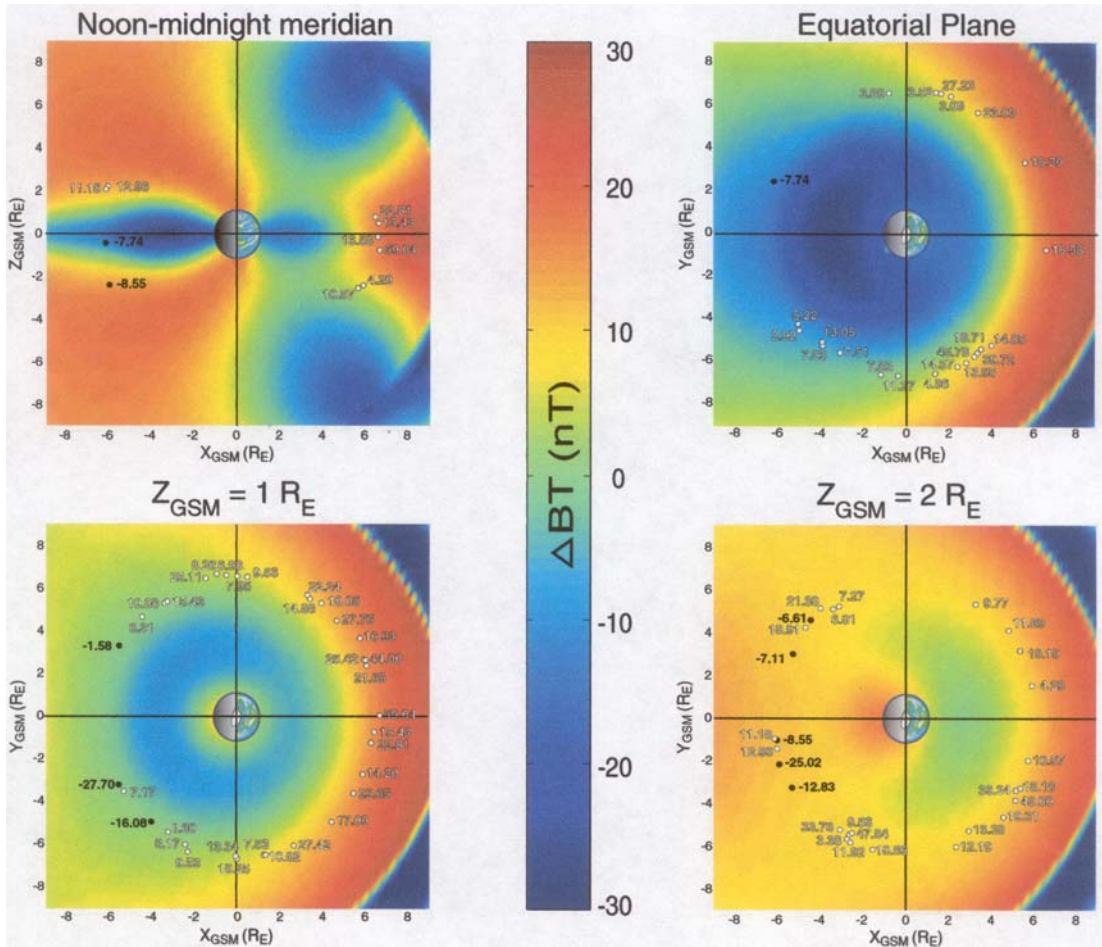


Figure 3.3: Contour plots of  $\Delta B$  predictions by the T96 model along the noon-midnight meridian and X-Y planes at three  $Z_{GSM}$  altitudes. Projected onto the noon-midnight meridian are  $\Delta B$  measurements observed by GOES 8, 9, and 10 spacecraft at locations within  $\pm 1 R_E$  of the plane (top left panel). GOES observations are also projected onto the equatorial plane (top right panel). There is north-south symmetry in the model predictions. Any observations within  $\pm 0.5 R_E$  of either  $Z_{GSM} = \pm 1 R_E$  planes are displayed in the bottom left panel. Any observations with  $\pm 0.5 R_E$  of either  $Z_{GSM} = \pm 2 R_E$  planes are displayed in the bottom right panel.

the GOES spacecraft measures only increases in magnetic field ( $+\Delta B$ ), which is consistent with the T01 model predictions (Figure 3.4). However, the dayside depression region predicted by the T96 model (Figure 3.3) is not sampled by the GOES spacecraft. There may be a depression region along the dayside equator generated by a compressed

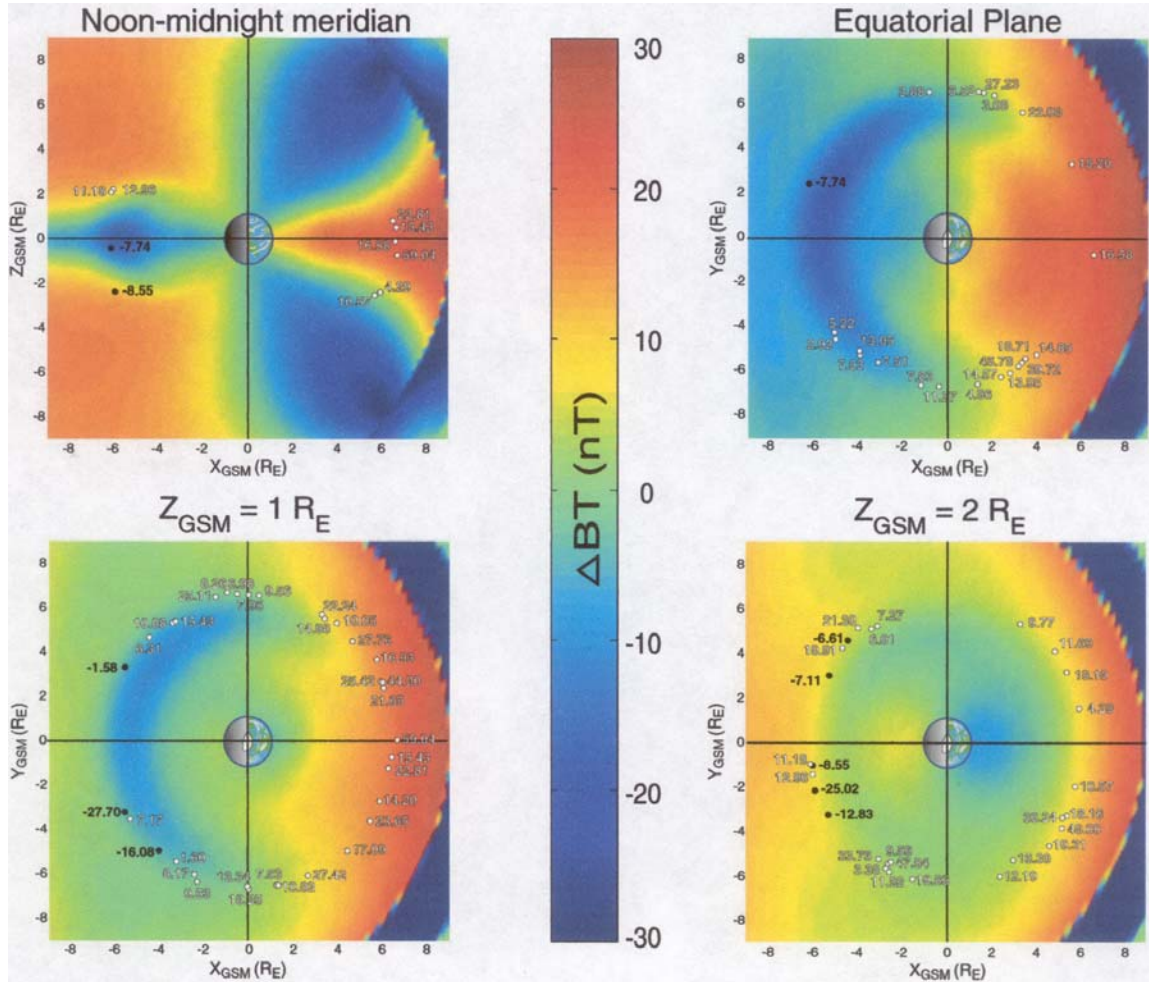


Figure 3.4: Contour plots of  $\Delta B$  predictions by the T01 model along the noon-midnight meridian and X-Y planes at three  $Z_{GSM}$  altitudes. Projected onto the noon-midnight meridian are  $\Delta B$  measurements observed by GOES 8, 9, and 10 spacecraft at locations within  $\pm 1 R_E$  of the plane (top left panel). GOES observations are also projected onto the equatorial plane (top right panel). There is north-south symmetry in the model predictions. Any observations within  $\pm 0.5 R_E$  of either  $Z_{GSM} = \pm 1 R_E$  planes are displayed in the bottom left panel. Any observations with  $\pm 0.5 R_E$  of either  $Z_{GSM} = \pm 2 R_E$  planes are displayed in the bottom right panel.

ring current, but we are unable to measure it with the Polar or GOES spacecraft. The comparisons presented in this section provide a global perspective of the magnetospheric response to a generic change in solar wind dynamic pressure, which we qualitatively confirm with spacecraft observations. In the following section we make statistical comparisons for the entire event pool.

### **3.3 Statistical Analysis of Observations and Model Predictions**

Until now, there has not been a statistical study of SIs measured by spacecraft throughout the magnetosphere. Previous observational studies investigated SIs *in situ* with spacecraft, but they were typically case studies focusing only on particular regions of the magnetosphere such as along the equatorial plane in geosynchronous orbit [Kokubun, 1983; Nagano and Araki, 1986; Rufenach et al., 1992; Araki, 1995], the magnetotail [Nakai et al., 1991; Fairfield and Jones, 1996], or the near Earth nightside [Ostapenko and Maltsev, 1998]. Over much of the magnetosphere the magnetic field increases when the solar wind dynamic pressure increases, but as shown in the previous chapter reductions in the magnetic field magnitude are also expected. Ostapenko and Maltsev [1998] attribute decreases in  $\Delta B$  on the nightside to the growth of the cross-tail currents. Fowler and Russell [2001] observed  $-\Delta B$  responses to magnetospheric compression at high altitudes on the dayside, which is consistent with the Tsyganenko models. We use these models with observed solar wind input parameters to replicate *in situ*  $\Delta B$  measurements from Polar. Statistical fits are used to determine the predictive

accuracy of each model, which is an indication of the realistic representation of dynamic magnetospheric processes.

We use fifteen minute averages of Wind plasma data upstream and downstream of interplanetary shocks and pressure pulses as input parameters for the T89, T96, and T01 models. Recall from the previous chapter that input parameters vary for each model, but all available choices for each model are utilized. *In situ* changes in magnetic field predicted by the models are compared with *in situ* observations of SIs using six-second magnetometer data from Polar and 1-minute data from the GOES spacecraft. The comparison plots presented in this chapter are for two dependent variables, so the best fit lines are based on the least absolute deviation (LAD). The LAD line minimizes the sum of the perpendicular deviation between each data point and the best fit line. The uncertainty in the slope of the LAD fit lines are based on model results when high and low estimates of solar wind number density ( $\pm 20\%$ ) are used as input parameters. The uncertainty associated with this input parameter is based on the results presented in Appendix 1.

### 3.3.1 Statistical Results

Figures 3.5 – 3.7 are scatter plots of  $\Delta B_{\text{Polar}}$  and  $\Delta B_{\text{GOES}}$  measurements compared to  $\Delta B$  predictions by the T89, T96, and T01 models. Solid red line represent the LAD best fit line and the dashed lines represent the uncertainty associated with the model results due to high and low estimates of the solar wind number density ( $\pm 20\%$ ). An ideal

magnetospheric model, which is expressed numerically as unity and illustrated as a solid black line in Figures 3.5 – 3.7. We use two indicators to assess the accuracy of the models. A precise prediction will have both unity slope and a high correlation coefficient.

Figure 3.5 is a plot of *in situ* Polar and GOES observations of SIs compared to  $\Delta B$  predictions from the T89 model. The LAD best fit line for the Polar observations (left panel) is  $y_{Polar} = 0.60 (\pm 0.02) x + 2.73 (\pm 0.95)$  with a correlation coefficient of  $R_{Polar} = 0.65 (\pm 0.02)$ . The LAD best fit line for the GOES observations (right panel) is  $y_{GOES} = 0.68 (\pm 0.07) x + 8.71 (\pm 1.55)$  with a correlation coefficient of  $R_{GOES} = 0.57 (\pm 0.01)$ .

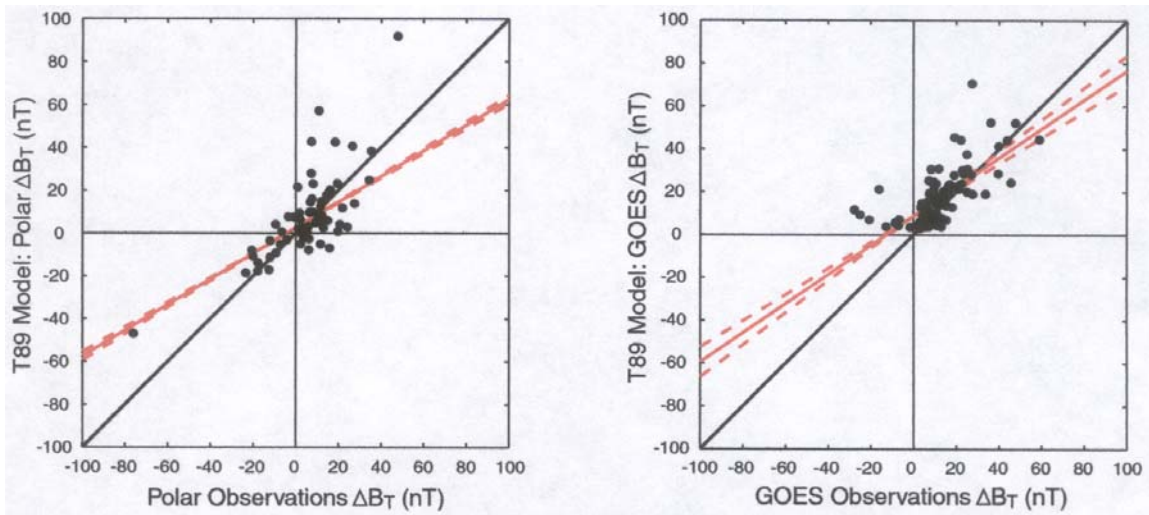


Figure 3.5: Correlation fits between  $\Delta B$  spacecraft observations and  $\Delta B_{T89}$  predictions. Polar observations are shown in the left panel and GOES observations are shown in the right panel. The red line is the least absolute deviation (LAD) fit, and the black line is unity.

The slopes are similar and significantly smaller than unity. One reason for this difference between observations and predictions is that that T89 model is a vacuum model with no

plasma present. The increase in pressure caused by magnetospheric compression will be partially in the plasma and partially in the field for the observations, but all in the field for the predictions. Thus, the observed field change should be lower than predictions, and the low correlation coefficients may be due to the variability of the plasma contribution. The two data sets have similar correlations to the T89 model predictions, and in both cases there is significant scatter, which includes events where the model and observations disagree about the sign of  $\Delta B$ . Statistically, the GOES observations are slightly better approximated by the T89 model, but the model does not predict any  $-\Delta B$  values for *in situ* GOES observations. This discrepancy results from the incompleteness of the T89 model, which only considers a magnetopause current that does not generate any compressional effects in the equatorial region (see Figures 2.4, 2.5, 3.1, and 3.2).

Figure 3.6 is a plot of *in situ* Polar and GOES observations of SIs compared to  $\Delta B$  predictions from the T96 model. The LAD best fit for the Polar data (left panel) is  $y_{Polar} = 0.43 (\pm 0.10) x + 7.91 (\pm 1.12)$  with a correlation coefficient of  $R_{Polar} = 0.43 (\pm 0.05)$ . The LAD best fit for the GOES data (right panel) is  $y_{GOES} = 0.43 (\pm 0.06) x + 2.23 (\pm 0.64)$  with a correlation coefficient of  $R_{GOES} = 0.46 (\pm 0.08)$ . Both the slopes and correlation coefficients for Polar and GOES have decreased. Neither of the numerical fits for the data sets is well replicated by the T96 model, and the scatter is also significant for both spacecraft data sets. Despite the additional input parameters and current systems, the complexity of the T96 model generates more discrepancies with observations. In theory, the compression of local current systems generates more local depression regions (see Figures 2.6, 2.7, 3.1, and 3.3), but the  $-\Delta B_{GOES}$  are not consistently predicted for *in*

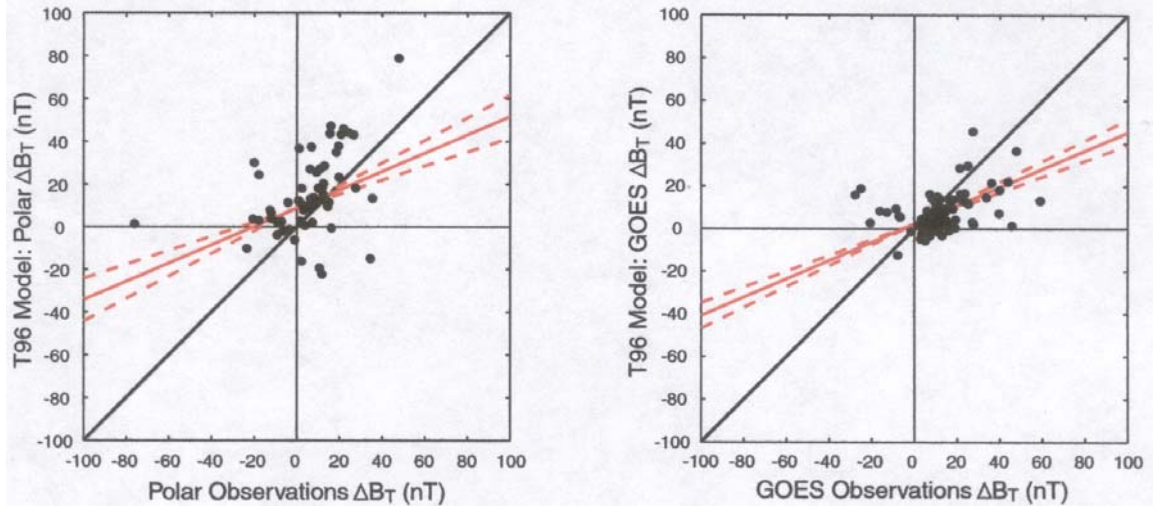


Figure 3.6: Correlation fits between  $\Delta B$  spacecraft observations and  $\Delta B_{T96}$  predictions. Polar observations are shown in the left panel and GOES observations are shown in the right panel. The red line is the least absolute deviation (LAD) fit, and the black line is unity.

*in situ* GOES observations. These differences are attributed to inaccuracies of the model in the equatorial region. Differences between the T96 model and Polar observations are attributed to the lack of empirical calibration at high altitude.

Figure 3.7 is a plot of *in situ* Polar and GOES observations of SIs compared to  $\Delta B$  predictions from the T01 model. The LAD best fit line for the Polar data (left panel) is  $y_{Polar} = 0.83 (\pm 0.06) x + 1.00 (\pm 0.39)$  with a correlation coefficient of  $R_{Polar} = 0.77 (\pm 0.09)$ . The LAD best fit line for the GOES data (right panel) is  $y_{GOES} = 0.84 (\pm 0.01) x - 2.54 (\pm 0.29)$  with a correlation coefficient of  $R_{GOES} = 0.76 (\pm 0.05)$ . Here we have a significant improvement in the slopes and the correlation coefficients. Both numerical fits are well approximated by the T01 model predictions and the correlation coefficients are also high for both data sets. This model produces fewer inconsistencies with regard to the sign of  $\Delta B$ , and the observations are well replicated both along the equator and at

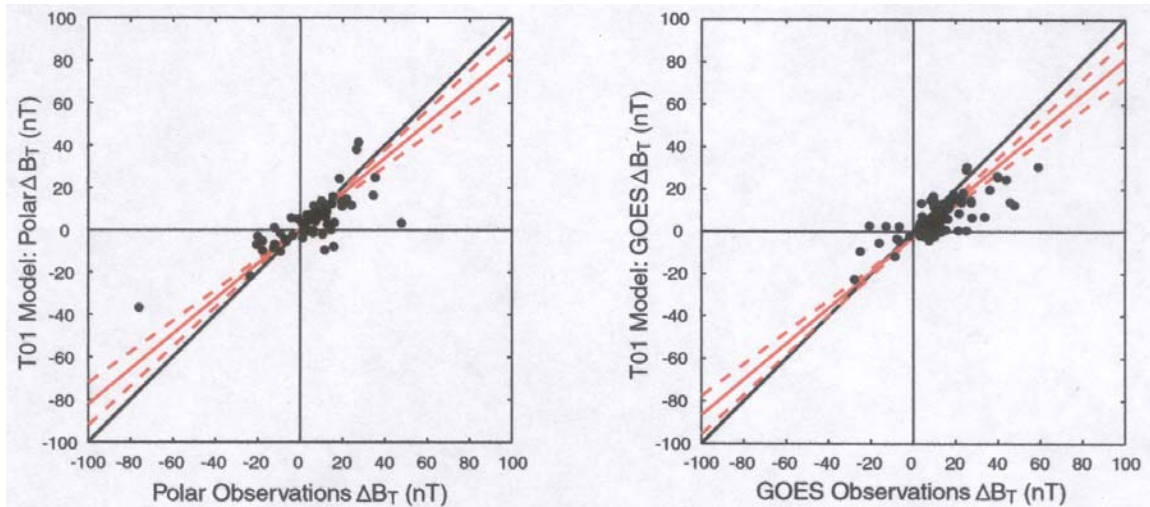


Figure 3.7: Correlation fits between  $\Delta B$  spacecraft observations and  $\Delta B_{T01}$  predictions. Polar observations are shown in the left panel and GOES observations are shown in the right panel. The red line is the least absolute deviation (LAD) fit, and the black line is unity.

high latitudes. Polar observations are well replicated with the T01 model because of the improved calibration with empirical data sets at high altitudes (see Section 2.1.3). GOES observations are also well replicated because the model includes accurate representations of realistic current systems (see Section 2.1.3).

### 3.3.2 Discussion of Numerical Results

The comparative statistics between Polar and GOES observations are summarized in Table 3.1, and the results from each model are discussed below. These numerical fits indicate that the T01 model provides the best replication of observations both at high altitudes and in the equatorial region.

The T89 model provides a suitable numerical approximation of magnetospheric

	Polar		GOES	
	LAD best fit	R	LAD best fit	R
T89 Model	$y = 0.60(\pm 0.02) x + 2.73 (\pm 0.95)$	0.65 ( $\pm 0.02$ )	$y = 0.68(\pm 0.07) x + 8.71 (\pm 1.55)$	0.57 ( $\pm 0.01$ )
T96 Model	$y = 0.43(\pm 0.10) x + 7.91 (\pm 1.12)$	0.43 ( $\pm 0.05$ )	$y = 0.43(\pm 0.06) x + 2.23 (\pm 0.64)$	0.46 ( $\pm 0.08$ )
T01 Model	$y = 0.83(\pm 0.06) x + 1.00 (\pm 0.39)$	0.77 ( $\pm 0.09$ )	$y = 0.84(\pm 0.01) x - 2.54 (\pm 0.29)$	0.76 ( $\pm 0.05$ )

Table 3.1: Numerical results from correlation fits presented in Figures 3.5 – 3.7.

compression at high altitudes but there are inconsistencies in the equatorial region. The LAD best fit lines are similar for both data sets and both fits are relatively close to unity. The correlation coefficient is higher for the Polar data because the analytical representation of the magnetosphere is flawed in the equatorial region. The T89 model does not predict a nightside depression region as illustrated in Figure 3.2. This discrepancy is also apparent in the right panel of Figure 3.5 where the T89 model fails to generate any  $-\Delta B$  values as observed by GOES along the equator. Despite the inaccuracies in the equatorial region, the T89 model well replicates the majority of  $-\Delta B$  observations by Polar at high latitudes. We conclude that the compressed magnetopause current generates the high altitude depression region because of the high correlation in this region.

The T96 model is the least effective in replicating observed SIs. The predictions at high altitudes are inaccurate due to the lack of calibration in this region, and in the equatorial region the model does not consistently predict  $-\Delta B$  values observed by GOES. Also, both data sets exhibit poor correlation coefficients. These results indicate that the T96 is inaccurate in all regions of the magnetosphere. Despite its shortcomings the T96

model can be dissected to determine the relevant contribution of each current system to the overall magnetic field changes. As mentioned above, the high correlation of the Polar observations to the T89 model predictions indicates the importance of the magnetopause current for generating the high altitude depression region. In the next section we remove the magnetic field contributions from each compressed current system. Thus, we investigate the relative importance of local current systems by examining the resulting correlations between observations and predictions from the T96 model.

The T01 model provides the best predictive accuracy throughout the magnetosphere. For both data sets the LAD fits are nearly identical and well approximate unity, which indicates the predictive accuracy of the T01 model for compression in all regions of the magnetosphere. The high correlation coefficients indicate the reliability of the model throughout the magnetosphere. Thus, we conclude that the T01 model provides an excellent representation of the global magnetosphere undergoing compression. Compressed currents contribute to the  $\Delta B$  values and in the next section we investigate the importance of individual currents contributing to the global  $\Delta B$  values.

### **3.4 Modifications to the T96 model**

We examine the relative effect of local currents on compressional signals. Statistical correlations are made between spacecraft observations and modified versions of T96 predictions that exclude field contributions from individual local currents.

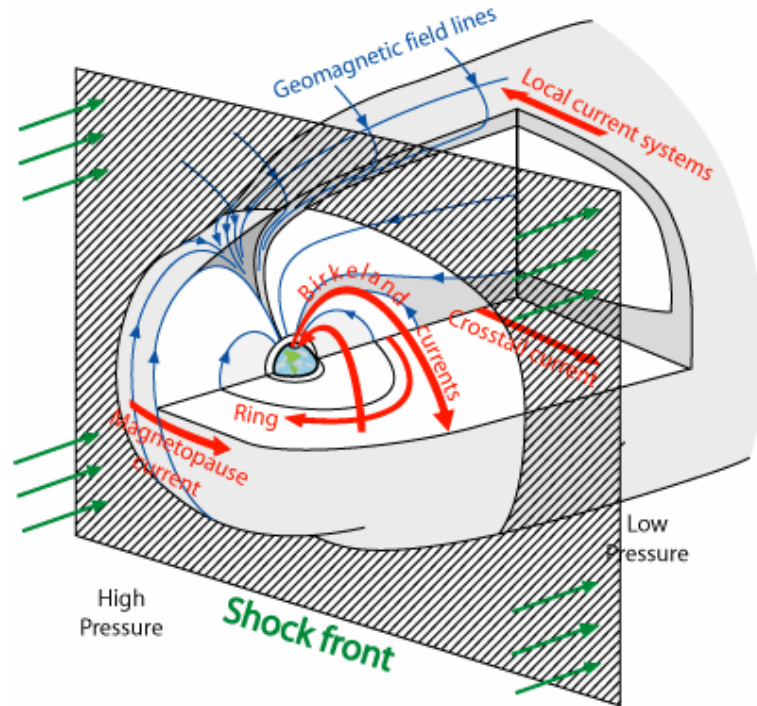


Figure 3.8: Illustration of the magnetosphere undergoing compression when a shock front passes along the exterior of the magnetosphere. Labeled in red are the local currents.

Illustrated in Figure 3.8 is the three dimensional model of the magnetosphere undergoing compression where the current systems are labeled in red. Presented in Figure 3.9 is a flowchart of the T96 model, which depicts how these local current systems contribute to *in situ* magnetic fields. We modify the T96 model by removing the magnetic field contributions from the three current systems (Birkeland, ring, and tail currents) individually and jointly. Upstream and downstream solar wind conditions are used to predict  $\Delta B$  values for correlation fits between  $\Delta B_{T96}$  and  $\Delta B_{obs}$ . A poor correlation fit with significant scatter indicates the importance of the particular current system removed. When all three current systems are removed, we expect the T96 model results to approximate magnetic field perturbations generated by the magnetopause current.

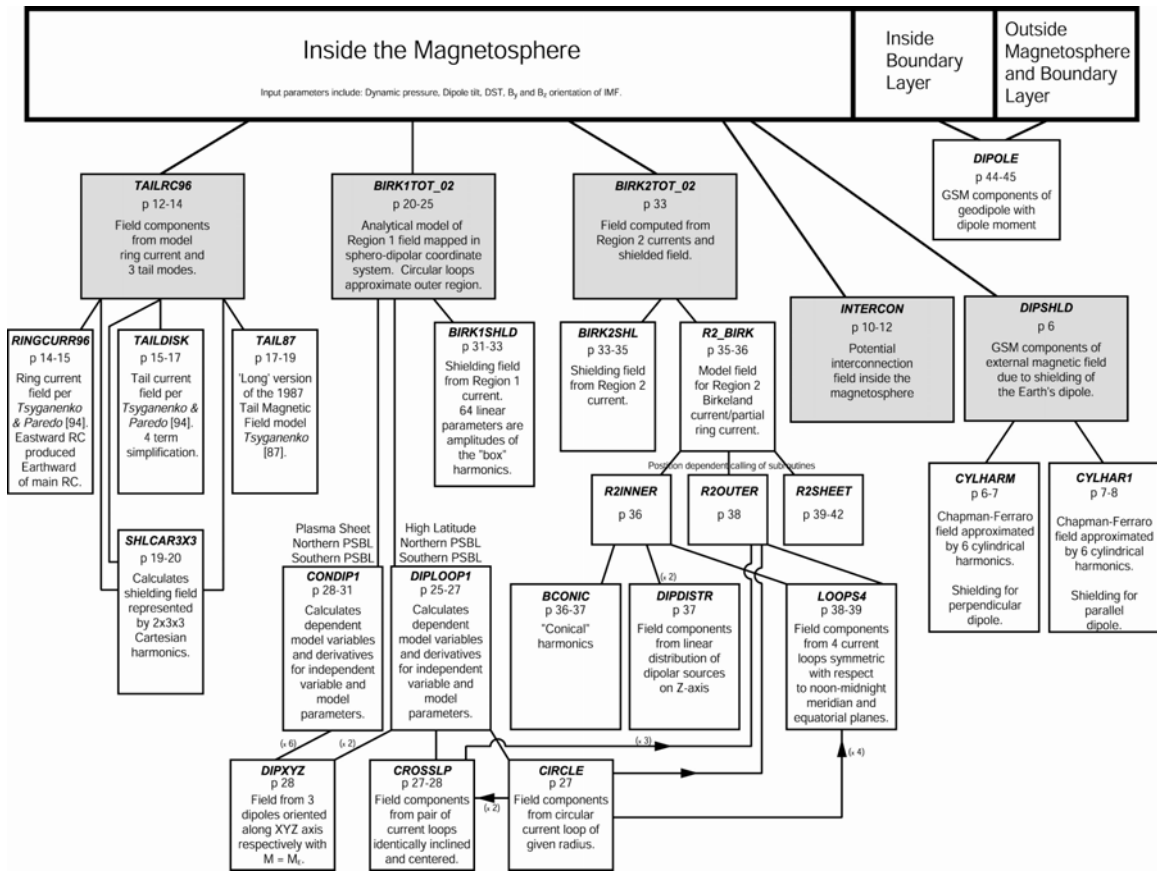


Figure 3.9: Flowchart of the subroutines used in the code for the T96 model.

### 3.4.1 Statistical Results

Presented in Figures 3.10 and 3.11 are scatter plots of  $\Delta B_{\text{Polar}}$  and  $\Delta B_{\text{GOES}}$  measurements compared to  $\Delta B$  predictions by modified versions of the T96 model. Solid red lines represent the LAD best fit line and the dashed lines represent the uncertainty associated with the model results due to high and low estimates of the solar wind number density ( $\pm 20\%$ ). An ideal magnetospheric model replicates spacecraft observations in all

regions of the magnetosphere, which is expressed numerically as unity and illustrated as a solid black line.

In Figure 3.10 are four scatter plots that correlate  $\Delta B_{\text{Polar}}$  observations to  $\Delta B_{\text{T96}}$  predictions from modified versions of the T96 model. Each plot is labeled according to the particular current systems removed from the T96 model either individually or jointly. The LAD best fit line from the T96 model with the Birkeland currents removed (top left panel) is  $y_{\text{Polar}} = 0.54 (\pm 0.16) x + 4.74 (\pm 0.43)$  with a correlation coefficient of  $R_{\text{Polar}} = 0.53 (\pm 0.04)$ . The LAD best fit line from the T96 model with the ring current removed

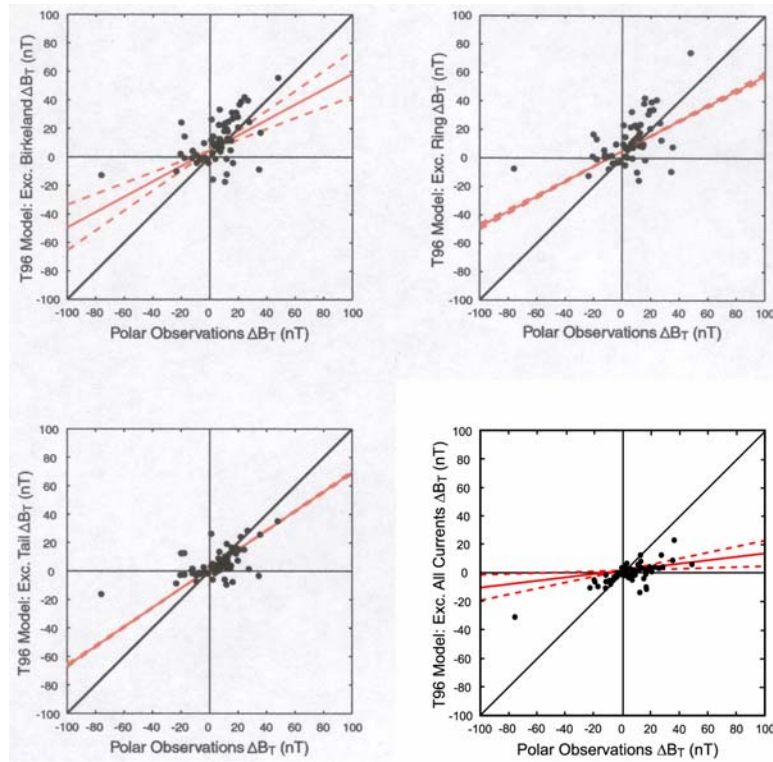


Figure 3.10: Correlation fits between  $\Delta B_{\text{Polar}}$  observations and  $\Delta B_{\text{T96}}$  predictions when magnetic field contributions from particular current systems are removed. Birkeland currents are excluded in the top left panel. The ring current has been removed from the top right panel. The tail current has been removed from the bottom left panel. All three currents have been removed from the bottom right panel.

(top right panel) is  $y_{Polar} = 0.53 (\pm 0.02) x + 4.87 (\pm 0.77)$  with a correlation coefficient of  $R_{Polar} = 0.52 (\pm 0.00)$ . The LAD best fit line from the T96 model with the tail current removed (bottom left panel) is  $y_{Polar} = 0.68 (\pm 0.02) x + 1.73 (\pm 0.38)$  with a correlation coefficient of  $R_{Polar} = 0.58 (\pm 0.04)$ . The LAD best fit line from the T96 model with all three currents removed (bottom right panel) is  $y_{Polar} = 0.12 (\pm 0.07) x + 1.21 (\pm 0.30)$  with a correlation coefficient of  $R_{Polar} = 0.75 (\pm 0.02)$ . The significance of the numerical statistics is discussed below.

In Figure 3.11 are four scatter plots that correlate  $\Delta B_{GOES}$  observations to  $\Delta B_{T96}$

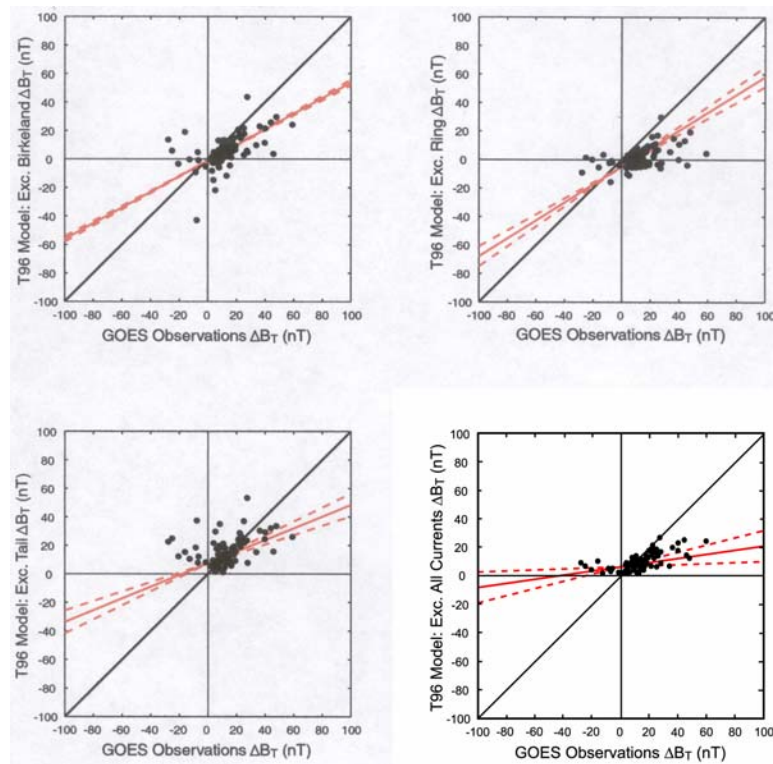


Figure 3.11: Correlation fits between  $\Delta B_{GOES}$  observations and  $\Delta B_{T96}$  predictions when magnetic field contributions from particular current systems are removed. Birkeland currents are excluded in the top left panel. The ring current has been removed from the top right panel. The tail current has been removed from the bottom left panel. All three currents have been removed from the bottom right panel.

predictions from modified versions of the T96 model, which are presented in the same manner as Figure 3.10. The LAD best fit line from the T96 model with the Birkeland currents removed (top left panel) is  $y_{GOES} = 0.55 (\pm 0.02) x - 0.94 (\pm 0.21)$  with a correlation coefficient of  $R_{GOES} = 0.58 (\pm 0.06)$ . The LAD best fit line from the T96 model with the ring current removed (top right panel) is  $y_{GOES} = 0.63 (\pm 0.07) x - 4.79 (\pm 0.22)$  with a correlation coefficient of  $R_{GOES} = 0.41 (\pm 0.08)$ . The LAD best fit line from the T96 model with the tail current removed (bottom left panel) is  $y_{GOES} = 0.39 (\pm 0.08) x + 8.25 (\pm 0.80)$  with a correlation coefficient of  $R_{GOES} = 0.38 (\pm 0.05)$ . The LAD line from the T96 model with all three currents removed (bottom right panel) is approximated due to a data corruption error. We find  $y_{GOES} \sim 0.15 (\pm 0.10) x + 5.00 (\pm 1.00)$  with a correlation coefficient of  $R_{GOES} = 0.58 (\pm 0.01)$ . The significance of the numerical statistic is discussed below.

### 3.4.2 Discussion of Numerical Results

In the previous section the LAD fit lines for both data sets were nearly identical for each magnetospheric model, but the results vary when magnetic field contributions from compressed current systems are removed from the T96 model. We determine the importance of each current system based on the lack of correlation after each current system is removed. Thus, the LAD fit line will approach unity if the removed current system does not make a significant contribution to  $\Delta B$ . Conversely, the removal of a prominent current system will cause the LAD fit line to approach zero. The numerical

results from the correlation fits between the modified T96 model versions and both the Polar and GOES data are summarized in Table 3.2.

T96 Model	Polar		GOES	
	LAD best fit	R	LAD best fit	R
No Birkeland	$y = 0.54(\pm 0.16) x$ $+ 4.74 (\pm 0.43)$	0.53 ( $\pm 0.04$ )	$y = 0.55(\pm 0.02) x$ $- 0.94 (\pm 0.21)$	0.58 ( $\pm 0.06$ )
No Ring	$y = 0.53(\pm 0.02) x$ $+ 4.87 (\pm 0.77)$	0.52 ( $\pm 0.00$ )	$y = 0.63(\pm 0.07) x$ $- 4.79 (\pm 0.22)$	0.41 ( $\pm 0.08$ )
No Tail	$y = 0.68(\pm 0.02) x$ $+ 1.73 (\pm 0.38)$	0.58 ( $\pm 0.04$ )	$y = 0.39(\pm 0.08) x$ $+ 8.25 (\pm 0.80)$	0.38 ( $\pm 0.05$ )
No Currents	$y = 0.12(\pm 0.07) x$ $+ 1.21 (\pm 0.30)$	0.75 ( $\pm 0.02$ )	$y \sim 0.15(\pm 0.10) x$ $+ 5.00 (\pm 1.00)$	0.58 ( $\pm 0.01$ )

Table 3.2: Numerical results from correlation fits presented in Figures 3.10 – 3.11.

When  $\Delta B$  contributions from the Birkeland currents are removed the correlation fits from both data sets are similarly affected. The correlation fits for the Polar and GOES data sets are nearly identical before and after the removal of the Birkeland currents. This is an excellent indication that the Birkeland currents have a similar impact at high altitudes and equatorial regions when the magnetosphere is compressed. We also find that the Birkeland currents do not significantly contribute to compressional signals because the LAD fits improve after the currents are removed. The correlation coefficients equally improve for both data sets, which provide additional reliance on the conclusion drawn about each data set.

When  $\Delta B$  contributions from the ring current are removed the correlation fits are improved for both data sets. Thus, we find that the ring current does not have a significant contribution to the compressional signal at high altitudes, which is physically

intuitive. However, the LAD fit for the GOES data set is much closer to unity. This indicates a less significant contribution from the ring current in the equatorial region, which is physically counterintuitive. Instead, we attribute the statistical changes to a ring current that is not properly represented by the T96 model. Recall that the T01 model includes the theoretical adjustments to account for observational evidence of a partial ring current [Tsyganenko, 2002].

When  $\Delta B$  contributions from the tail current are removed the data sets are adversely affected. The LAD fit for the Polar data is significantly closer to unity, which indicates that the tail current does not affect compressional signals at higher altitudes. The correlation coefficient also increases, which indicates an improvement in the reliability of the correlation fit. Conversely, the LAD fit for the GOES data set is less correlated and the fit is unreliable. These statistical factors indicate that the tail current makes a significant contribution to  $\Delta B$  perturbations in the equatorial region, especially on the nightside. We have previously shown that the tail current is responsible for generating the depression region on the nightside equator (see Figure 3.3). This conclusion is reinforced by inspection of the bottom left panel of Figure 3.11 where the T96 model does not generate  $-\Delta B$  values without the tail current.

When the  $\Delta B$  contributions from all three current systems are removed the LAD slopes decrease significantly. These results are expected to approximate the results from the T89 model since the global compressional signal would be generated by only remaining current, the magnetopause current. However, both slopes are significantly lower than unity. The poor replication of the Polar data is due to the lack of calibration

of the T96 model at high latitudes, but there is high correlation because all observations are under estimated. We note that the LAD fit with the GOES data is only an estimation because of a data corruption error. This slope is significantly lower than unity because removal of the three currents precludes the T96 model from generating any  $-\Delta B$  values along the equator, as shown in the bottom right panel of Figure 3.11. We conclude that the model requires the inclusion of all currents for replication of observations, but the most important current is the tail current, especially in the low latitude region.

### 3.5 Response ratios

SIs are the observable magnetospheric response to sudden changes in the solar wind dynamic pressure changes that reach the magnetosphere. These pressure fronts compress the magnetosphere and the magnetic field increase to maintain the pressure balance. The response ratio ( $\Delta B/\Delta p^{1/2}$ ) parameterizes the magnetospheric response in terms of changes in magnetic field magnitude relative to the changes in dynamic pressure. The response ratio is determined for the Polar SI observations at high altitude, which are consistent with previously determined response ratios in other regions of the magnetosphere and near the surface of the Earth.

Earlier studies determined the response ratios of pressure pulse triggered SIs using ground-based magnetometers [*Siscoe et al.*, 1968; *Oglivie et al.*, 1968; *Verzariu et al.*, 1972; *Su and Konradi*, 1975]. Other ground-based studies investigated how the response ratio is affected by local time and IMF orientation [*Russell et al.*, 1992; *Russell*

*et al.*, 1994a, b]. Figure 3.12 shows Polar observations of  $\Delta B_T$  plotted as a function of the change in the square root of dynamic pressure ( $\Delta\sqrt{\rho v^2}$ ) for each SI event studied in this thesis. The slope of the median line is  $11.6 (\pm 2.8) \text{ nT/nPa}^{1/2}$ , which corresponds to the response ratio of  $|\Delta B|$  measurements for the entire data set. Also shown in Figure 3.12 is the median line with a slope of  $-19.4 (\pm 1.5) \text{ nT/nPa}^{1/2}$  for only  $-\Delta B$  observations. There are too few  $-\Delta B$  events to provide statistics on solely these events, so it is more appropriate to examine the response ratio in terms of  $|\Delta B|$ , which is consistent with previously calculated response ratios ( $14 \text{ nT/nPa}^{1/2}$ ) [*Siscoe et al.*, 1968]. It was shown in

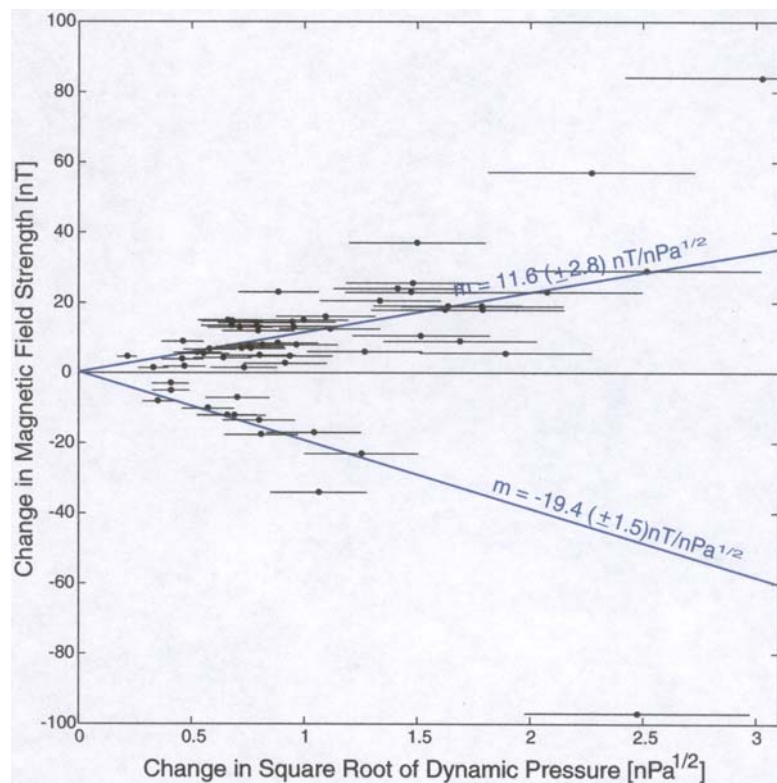


Figure 3.12: Polar  $\Delta B$  observations versus  $\Delta\sqrt{p}$ . The median fit line of  $|\Delta nT/\Delta nPa^{1/2}|$  is  $11.6 (\pm 2.8) \text{ nT/nPa}^{1/2}$  for the entire data set. The response ratio for  $-\Delta B$  observations is  $-19.4 (\pm 1.5) \text{ nT/nPa}^{1/2}$ .

the previous chapter that additional solar wind conditions affect the global response of  $\Delta B$  (see Figures 2.11 – 2.13), so we investigate the effect of IMF orientation on the response ratio.

*Russell et al.* [1994a, b] used ground-based data to investigate the effects of local time and IMF orientation on the magnetospheric response. They found that the average magnetospheric response at mid-latitudes during northward IMF was  $18.4 \text{ nT/nPa}^{1/2}$  [1994a]. During southward IMF the magnetospheric response on the dayside was reduced by 25% because of Region 1 Birkeland currents [*Russell et al.*, 1994b]. *Russell et al.* also found a day-night asymmetry in the magnetospheric response, which they attributed to the enhancement of tail currents during magnetospheric compression [*Russell et al.*, 1994a]. Although ionospheric currents affect magnetic field measurements on the surface of the Earth, the *Russell et al.* response ratios are good approximations of SIs observed by spacecraft. Figure 3.13 is a scatter plot of  $\Delta B$  as a function of  $\Delta\sqrt{pv^2}$ , color-coded according to the IMF conditions and SI location according to *Russell et al.* [1994a, b]. The response ratios determined by *Russell et al.* are shown as positive and negative slopes, although their research did not investigate any  $-\Delta B$  events. They found an average response ratio of  $18.4 \text{ nT/nPa}^{1/2}$  for SIs observed on the dayside during northward IMF (blue). They found an average response ratio of  $13.8 \text{ nT/nPa}^{1/2}$  for SIs observed on the dayside during a southward IMF (green). They also found an average response ratio of  $12.3 \text{ nT/nPa}^{1/2}$  for SIs observed on the nightside during northward IMF (red). Using these same categories, the response ratios for Polar observations are determined by the median slopes of the  $|\Delta B/\Delta\sqrt{p}|$  measurements. We

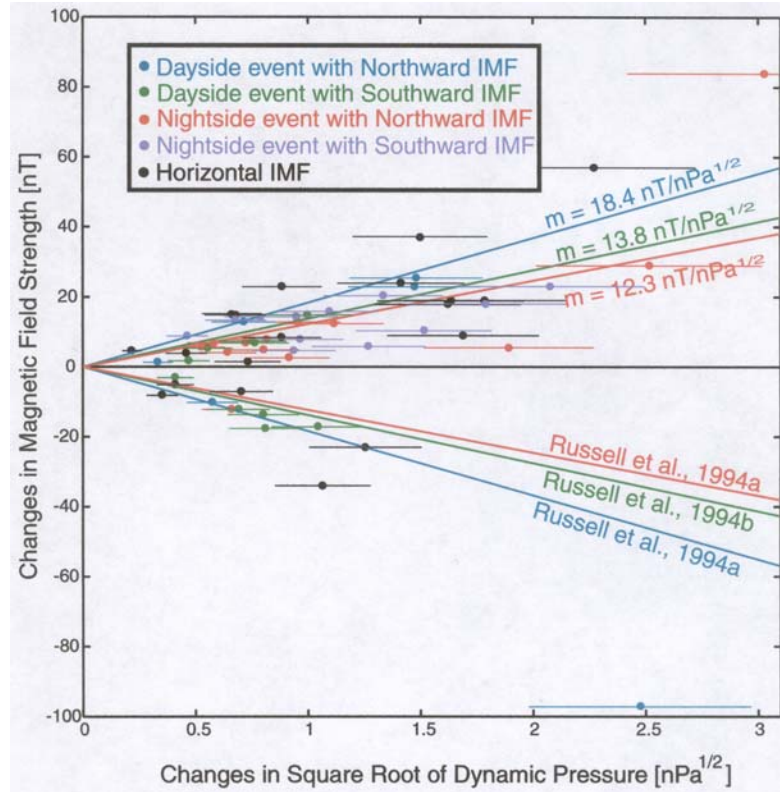


Figure 3.13: Polar  $\Delta B$  observations versus  $\Delta\sqrt{p}$ . Shown in the Figure key is the color-coding used to represent IMF orientation and SI location for each event. Also displayed are the response ratios determined by *Russell et al.* [1994a, b]. The slopes of these lines are similarly color-coded according to the conditions described in the key.

find a response ratio of  $17.7 (\pm 1.4) \text{ nT/nPa}^{1/2}$  for SIs observed on the dayside during northward IMF (blue). We find a response ratio of  $12.6 (\pm 1.8) \text{ nT/nPa}^{1/2}$  for SIs observed on the dayside during southward IMF (green). We also find a response ratio of  $11.3 (\pm 2.8) \text{ nT/nPa}^{1/2}$  for SIs observed on the nightside during northward IMF (red). IN all three cases the response ratios for the Polar spacecraft are well approximated by the previous research, and any discrepancy is attributed to the ionospheric effect on ground-based measurements. We find the same overall trend occurs for the space-based response ratios, as seen in the ground-based response ratios. The largest response ratio is

SI local time/ IMF orientation	<i>Russell et al., 1994a</i> $nT/\sqrt{nPa}$	<i>Russell et al., 1994b</i> $nT/\sqrt{nPa}$	Polar Observations $nT/\sqrt{nPa}$
Dayside/Northward IMF	18.4	-	$17.7 \pm 1.4$
Dayside/Southward IMF	-	13.8	$12.6 \pm 1.8$
Nightside/Northward IMF	12.3	-	$11.3 \pm 2.8$
Nightside/Southward IMF	-	-	$12.9 \pm 1.5$
Day & Night/Horizontal IMF	-	-	$17.4 \pm 4.3$

Table 3.3: Summary of numerical results from response ratios in Figure 3.13.

associated with SIs observed on the dayside during northward IMF. We also find that dayside SIs have a smaller average response ratio during southward IMF. The response ratios discussed in this section are summarized in Table 3.3.

The response ratio of Polar observations is examined for an additional category that is not considered by *Russell et al.* We find a response ratio of  $12.9 (\pm 1.5) nT/nPa^{1/2}$  for SIs observed on the nightside during a southward IMF (purple). The response ratios are consistent during southward IMF (green and purple) regardless of the local time location of the SI. We also find a response ratio of  $17.4 (\pm 4.3) nT/nPa^{1/2}$  for SIs observed on either the dayside or nightside during a horizontal IMF (black), which is numerically consistent with the dayside observations during northward IMF.

The error bars associated with  $\Delta p^{1/2}$  are based on discrepancies in solar wind density measurements by the Wind and ACE solar wind monitors. Appendix 1 presents a method of intercalibrating the plasma measurements by the spacecraft as a function of

solar wind speed and ion thermal speeds. Based on this analysis we use a fractional uncertainty of 20% associated with solar wind density measurements.

### **3.6 Summary and conclusions**

In this chapter we used Polar and GOES observations to verify the global response of magnetospheric compression predicted by the three magnetospheric models. In the previous chapter we found a high altitude depression region predicted by the T89, T96, and T01 models due to the compression of the magnetosphere. Polar observations confirmed that a depression region is generated at high altitudes, as shown in Figure 3.1. However, the T89 model did not account for  $-\Delta B$  observations by GOES in the equatorial region (see Figure 3.2). A second depression region is predicted on the nightside by the T96 and T01 as a result of a compressed tail current, which was confirmed by GOES observations (see Figures 3.3 and 3.4). The T96 model predicted another dayside depression region generated due to the compression of the ring current, which was attributed to an inaccurate representation of the partial ring current. We did not find any observations that confirm the generation of the depression region.

We used numerical correlation fits between spacecraft observations and model predictions to test the validity of the global compression. These results indicated that the T01 model provides the best fit to SI observations in all magnetospheric regions. This model most accurately represents the magnetospheric current systems, and the calibration throughout the magnetosphere provides confidence in the results. The T89 model well

replicates the Polar observations, which is an indication of the generation of the depression region at high altitudes due to the compression of the magnetopause current. Despite the high correlation with the GOES data, the T89 model does not predict any  $-\Delta B$  observations on the nightside (see right panel of Figure 3.5). The T96 model produced the poorest replication of observations and there was significant scatter in the correlation. The T96 model is expected to have deficiencies at high altitudes because of the lack of empirical calibration in this region. Additionally, the T96 model inaccurately represents the dayside equatorial compression the partial ring current is improperly calculated. Thus, we conclude that the T01 model provides the best representation of compressional signals throughout the magnetosphere, thereby reinforcing the physical model of magnetospheric compression in three dimensions.

We used correlation fits with modified versions of the T96 model that exclude magnetic field contributions from different current systems. A poor correlation indicated the relevant importance of magnetic field contributions by each current system to the global compressional signal. We found that the magnetopause current is responsible for the high altitude depression region because removal of all three current systems improved the correlation fits with Polar observations. We also found that the tail current is vital for the generation of the nightside depression region. Removal of the magnetic field contribution from a compressed tail current adversely affects the correlation with the GOES data (see bottom panels of Figure 3.11 and Table 3.2). The Birkeland currents and ring current did not significantly contribute to the compressional signal in the equatorial

region. Thus, we conclude that the magnetopause currents generate the high altitude depression region and the tail current generates the nightside depression region.

We quantified the  $\Delta B$  observations with the response ratio, which compares the global magnetospheric response as a function of the change in the square root of dynamic pressure changes. We found that the response ratio ( $|\Delta B/\sqrt{p}|$ ) for the Polar data is  $11.6 (\pm 2.8) \text{ nT/nPa}^{1/2}$ , which agrees with previous ground-based measurements [Siscoe *et al.*, 1968]. We also categorized the SI events according to SI local time location and IMF orientation to determine the relative effects on the response ratio. We found that the largest response ratio occurs on the dayside during a northward IMF. We also found that southward IMF generates a response ratio of  $12.6 (\pm 1.8) \text{ nT/nPa}^{1/2}$  on the dayside, which is consistent with previous research [Russell *et al.*, 1994b]. Thus, we conclude that the southward IMF orientation will lead to smaller response ratios on the dayside. We also conclude that the largest response ratios are anticipated on the dayside.

### 3.7 References

- Araki, T., Response of the Earth's magnetosphere to dynamic pressure variation of solar wind, *Proc. Of the Second SOLTIP Symposium*, Nakaminato, Japan, 13-17, June 1994, STEP GBRSC News, Vol. 5, pp. 279-282, 1995.
- Fairfield, D. H. and J. Jones, Variability of the tail lobe field strength, *J. Geophys. Res.*, 101, 7785-7791, 1996.
- Fowler, G. J. and C. T. Russell, Geomagnetic field response along the Polar orbit to rapid changes in the solar wind dynamic pressure, *J. Geophys. Res.*, 106, 18,943-18,956, 2001.
- Kokubun, S, Characteristics of storm sudden commencement at geostationary orbit, *J. Geophys. Res.*, 88, 10,025-10,033, 1983.
- Nagano, H. and T. Araki, Seasonal variation of amplitude of geomagnetic sudden commencements near midnight at geostationary orbit, *Planet. Space Sci.*, 24, 205-217, 1986.
- Nakai, H., Y. Kamide, and C. T. Russell, Influences of solar wind parameters and geomagnetic activity on the tail lobe magnetic field: a statistical study, *J. Geophys. Res.*, 96, 5511-5523, 1991.
- Ogilvie, K. W., L. F. Burlaga, and T. D. Wilkerson, Plasma observations on Explorer 34, *J. Geophys. Res.*, 73, 6809, 1968.
- Ostapenko, A. A. and Y. P. Maltsev, Three-dimensional magnetospheric response to variations in the solar wind dynamic pressure, *Geophys. Res. Lett.*, 25, 261-263, 1998.
- Rufenach, C. L., R. L. McPherron, and J. Schaper, The quiet geomagnetic field at geosynchronous orbit, and its dependence on solar wind dynamic pressure, *J. Geophys. Res.*, 97, 25-42, 1992.
- Russell, C. T., M. Ginskey, S. Petrinec, and G. Le, The effect of solar wind dynamic pressure changes on low and mid-latitude magnetic records, *Geophys. Res. Lett.*, 19, 1227-1230, 1992.
- Russell, C. T., M. Ginskey, and S. M. Petrinec, Sudden impulses at low-latitude stations: Steady state response for northward interplanetary magnetic field, *J. Geophys. Res.*, 99, 253-261, 1994a.
- Russell, C. T., M. Ginskey, and S. M. Petrinec, Sudden impulses at low latitude stations: Steady state response for southward interplanetary magnetic field, *J. Geophys. Res.*, 99, 13,403-13,408, 1994b.

Sibeck, D. G., R. E. Lopez, and E. C. Roelof, Solar wind control of the magnetopause shape, location, and motion, *J. Geophys. Res.*, 96, 5489-5495, 1991.

Siscoe, G. L., V. Formisano, and A. J. Lazarus, relation between geomagnetic sudden impulses and solar wind pressure changes: an experimental investigation, *J. Geophys. Res.*, 73, 4869-4874, 1968.

Su, S. Y. and A. Konradi, Magnetic field depression at the Earth's surface calculated from the relationship between the size of the magnetosphere and *Dst* values, *J. Geophys. Res.*, 80, 195, 1975.

Verzariu, P., M. Sugiura, and I. B. Strong, Geomagnetic field variations caused by changes in the quiet time solar wind pressure, *Planet. Space Sci.*, 20, 1909, 1972.

## Chapter 4: Analysis of SI Rise Times

### 4.1 Introduction

We investigate the relationship between the speed of a solar wind structure moving along the magnetosphere and the duration of the magnetospheric response. A thin interplanetary shock produces a lengthy response because the finite size of the magnetosphere prolongs the interaction to the interval required for the shock to pass by the magnetosphere and near tail region [Wilken *et al.*, 1982]. If hydromagnetic waves within the magnetosphere communicate the compressional signal faster than the solar wind disturbance travels down the boundary the magnetospheric field then the increase in magnetic field magnitude will be slow and gradual. If the shock induced disturbance moves faster than the local fast mode speed the compressional signal inside the magnetosphere will be shock like. *A priori* it is not certain where to expect a sudden rise in field strength or a slow one. This is important because a more rapid change in magnetic fields can enhance the radial diffusion of energized particles and the energy range of the acceleration will depend on the sharpness of the compression. In other words, Faraday's law ( $\partial B/\partial t = -\nabla \times \mathbf{E}$ ) states that magnetic fields varying rapidly in time will produce an electric field capable of energizing particles. Thus, solar wind structures are capable of providing energy to magnetospheric particles without reconnection occurring.

The rise time of a compressional signal is a measurement of an SIs duration that

begins at onset and ends when the magnetic field is fully enhanced, which lasts roughly 2-10 minutes with an average of 4 minutes [Maeda *et al.*, 1962]. Previous research on this topic has led to several different theories on magnetospheric effects that lengthen the rise time. Baumjohann *et al.* [1983] theorized that the rise time is based on a time constant of the magnetosphere rather than a propagation effect. Several influential factors proposed by Nishida [1964, 1966] include the type of solar wind discontinuity, the thickness of the shock front, the duration for the solar wind front to sweep by the magnetosphere, and the variable transit times of the compressional front within the magnetosphere. Ondoh [1963] concluded that SI rise times are truncated on the dayside and lengthened on the nightside due to the transit time of hydromagnetic waves throughout the magnetosphere. Several previous studies investigated an inverse relationship between the rise time of sudden commencements and the magnitude of the change in magnetic field measured at the surface of the Earth [Dessler *et al.*, 1968; Pisharoty and Srivastava, 1962; Mayaud, 1975]. Dessler *et al.* [1960] further proposed that SI rise times are sensitive to the size and shape of the magnetospheric boundary since this affects the transit time of hydromagnetic waves. Takeuchi *et al.* [2002] attribute an extended rise time to the oblique orientation of the shock front. In contrast, Burlaga and Ogilvie [1969] contend that SI rise times have no relation to the type of discontinuity, the speed of the solar wind structure or its thickness, although no other physical mechanism was suggested.

Here, we investigate the effect of solar wind speed on the SI rise time. Our presumption is that the solar wind speed is the most relevant parameter since the speed of

the structure moving past the magnetosphere's exterior determines the duration of interaction between the shock front and the magnetosphere. To test this assumption we begin with two case studies of SIs well replicated by the *Raeder et al.* [2001] MHD model, and then we modify the input parameters and assess the qualitative difference in the SI signal. We find that the SI rise time is truncated when the shock front travels faster and the rise time is prolonged when the shock front travels slower.

Additionally, the shock speeds and SI rise times are used to calculate an average geoeffective length for the entire data set. A solar wind structure that compresses the magnetosphere eventually travels a distance downtail from the subsolar point from which the compressional signal is no longer detected *in situ*. This distance, known as the geoeffective length, for the shock events in this thesis has an average length of 18.7  $R_E$ . We note that the SI rise times discussed in this section exclude the initial and final 10% of the observed SI signal to account for the uncertainty in the SI onset and completion. This assumption is used since the precise measurement of SI onset and completion are somewhat subjective due to subtle gradients in high resolution magnetometer observations of magnetic field magnitude.

## 4.2 Rise times and shock speed

We investigate the effect of solar wind speed on the SI rise times by comparing MHD results from simulation runs with various solar wind speeds. We begin with Wind measurements of solar wind velocity ( $V_x, V_y, V_z$ ), plasma number density ( $N_p$ ), IMF

components ( $B_y$  &  $B_z$ ), and thermal pressure as input parameters in ninety-second intervals. Additional simulation runs use solar wind speeds that are increased or decreased by a multiplicative factor ( $X$ ). A proportional adjustment to plasma number density ( $1/X^2$ ) ensures that dynamic pressure values are similar for each simulation run. All other input parameters are retained at the original values measured by Wind so that this study specifically focuses on effects of solar wind speed. Another input parameter is the normal vector ( $\mathbf{n}$ ), which is fixed throughout each simulation run. The normal vector is determined by the co-planarity formula [Colburn and Sonett, 1966; Burgess, 1995]:

$$\text{(Eqn. 4.1)} \quad \mathbf{n} = [(\mathbf{B}_1 - \mathbf{B}_2) \times (\mathbf{B}_1 \times \mathbf{B}_2)] / |(\mathbf{B}_1 - \mathbf{B}_2) \times (\mathbf{B}_1 \times \mathbf{B}_2)|$$

where  $\mathbf{B}_1$  is the Wind measurement of the IMF upstream of the shock front and  $\mathbf{B}_2$  is the downstream IMF. The downstream  $B_x$  and  $\mathbf{n}$  values are held constant throughout each simulation run to ensure that  $\mathbf{B}$  remain divergenceless ( $\nabla \cdot \mathbf{B} = 0$ ) during the simulation. The shock velocity ( $V_S$ ) is not an input parameter, but it quantifies the propagation of a shock front in the solar wind. This value is calculated as follows:

$$\text{(Eqn. 4.2)} \quad V_S = \mathbf{n} \cdot (\rho_u v_u - \rho_d v_d) / (\rho_u - \rho_d)$$

where  $\rho$  and  $v$  are the plasma density and solar wind speed values measured upstream and downstream of the shock front. Throughout this chapter we will express this quantity in the  $X_{\text{GSM}}$  direction. This vector best approximates the spatial dimension along which the

shock front and the magnetosphere interact. We note that the solar wind is launched from an inflow boundary of  $20 R_E$  upstream of the magnetosphere thereby precluding any evolution of the solar wind structure before encountering the magnetosphere. Presented in Figures 4.1 and 4.2 are time series plots of SI observations and MHD results for two case studies. We compare dynamic changes in magnetic fields ( $B_x$ ,  $B_y$ ,  $B_z$ , and  $B_T$ ) and conclude that SI rise times are dependent on the solar wind speed.

#### *4.2.1 Case study: October 12, 2000*

Presented in Figure 4.1 are the time series plot of the residual magnetic fields observed on October 12, 2000 by Polar at  $(-4.50, -0.98, 5.53 R_E \text{ GSM})$ , which are depicted by the black dashed trace. The blue trace represents the MHD results when Wind observations are used as input parameters. The model results well replicate the SI observation both in magnitude and duration (4 minutes). There is an additional secondary increase in  $B_x$  and  $B_T$  due to an artifact in the  $N_p$  input parameter. Additional traces (green and red) are the MHD results from alternate simulations when  $V_x$  and  $N_p$  are modified from their original values, and the results from each scenario are discussed below. Fixed input parameters for all simulation runs are  $B_x = -1.39 \text{ nT}$  and  $\mathbf{n} = 0.8, -0.5, 0.3$ . The observed shock front has a speed of  $V_x = 497 (\pm 50) \text{ km/s}$ .

Depicted by the green trace is the simulation run when  $V_x$  values are doubled and  $N_p$  values are reduced by a factor of four. The green trace matches the magnitude change in  $B_x$  and  $B_T$ , but there is an additional rotation in  $B_y$ . Full compression of the field is

reached more rapidly (3 minutes), which is exemplified by a steeper gradient in the time series profile of  $B_T$ . For this simulation  $V_S = 994 (\pm 99)$  km/s, which is twice the value in the original simulation. Thus, doubling the solar wind speed quickens magnetospheric

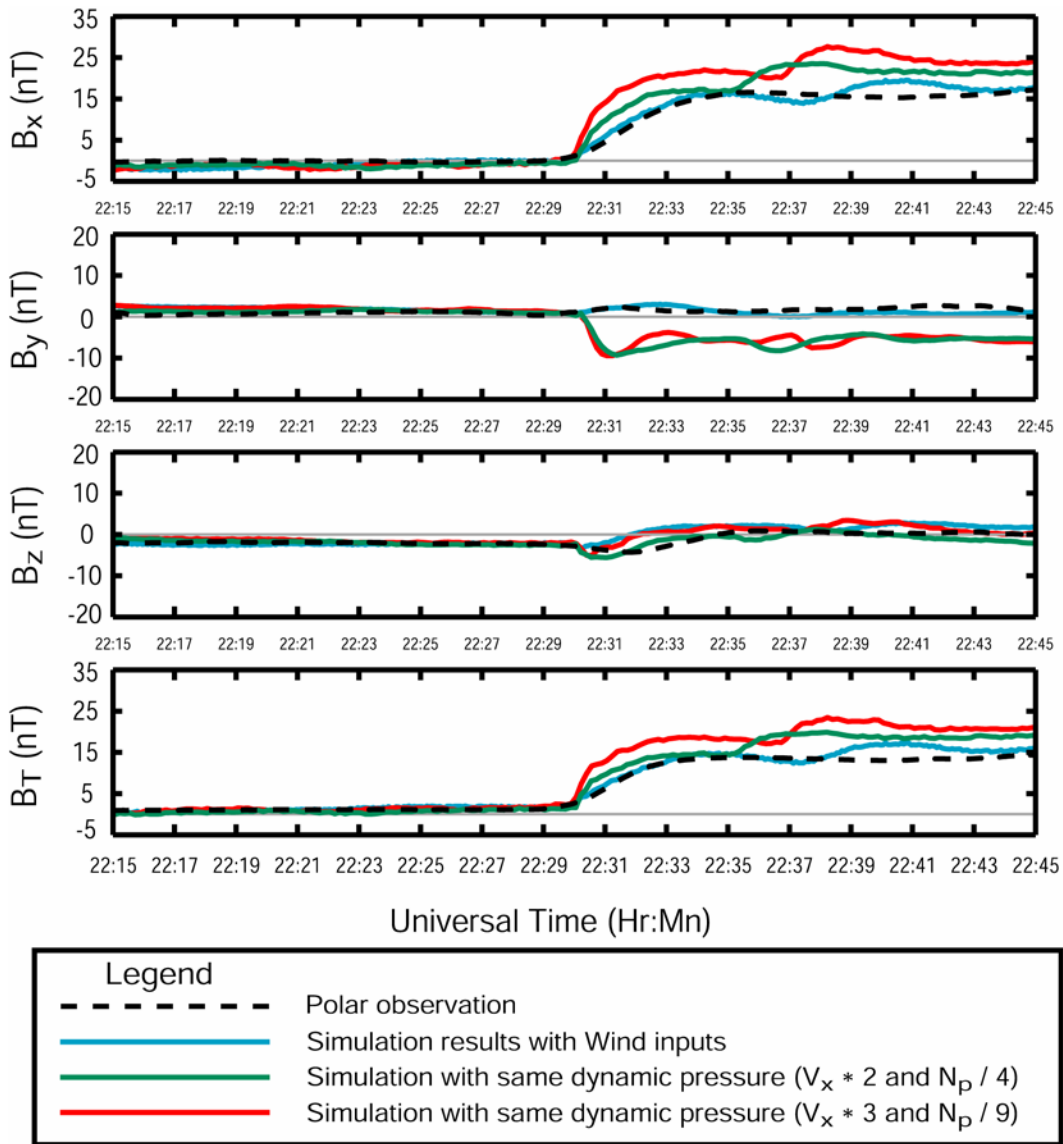


Figure 4.1: Time series plot of the SI observed by Polar on 10/12/00 (black dashed trace) and the MHD simulation results (blue trace). The MHD results from simulations with modified inputs are also presented (green and red traces).

compression by approximately one minute.

Depicted by the red trace is the simulation run when  $V_X$  values are tripled and  $N_p$  values are reduced by a factor of nine. In this simulation there is a similar rotation in the  $B_Y$  component, but more importantly there is rapid amplification in the  $B_X$  and  $B_T$  components (2.75 minutes). Although the dynamic pressure is similar for all simulations there is a larger amplification in the  $B_X$  and  $B_T$  components. The background field at this *in situ* location primarily consists of a  $B_X$  component and is therefore susceptible to preferential forcing in the  $-X_{GSM}$  direction when the solar wind speed is amplified solely in the  $V_X$  component. For this simulation  $V_S = 1491 (\pm 149)$  km/s, which is three times greater than the value in the original simulation. Thus, tripling the solar wind speed hastens magnetospheric compression by 115 seconds.

#### 4.2.2 Case study: September 28, 1996

Presented in Figure 4.2 are the time series plot of the residual magnetic fields observed on September 28, 1996 by Polar at (4.44, 0.95, 4.54  $R_E$  GSM), which are depicted by the black trace. The blue trace represents the MHD results when Wind observations are used as input parameters. The model predicts a  $-\Delta B$  that is -10 nT greater in magnitude and three minutes longer in duration than the Polar SI observation. The dynamic field changes are not exactly replicated by the MHD model due to artifacts in the solar wind density input parameter, but the  $B_X$  and  $B_Z$  components are nearly replicated in magnitude and duration. There is a noticeable difference in the  $B_Y$

component because the MHD model does not predict an oscillation in this field component. Additional traces (green, red, purple, and orange) are the MHD results from alternate simulations when  $V_x$  and  $N_p$  are modified from their original values, and the results from each scenario are discussed below. Fixed input parameters for all simulation runs are  $B_x = -0.10$  nT and  $\mathbf{n} = 0.8, -0.5, 0.3$ . The observed shock front has a speed of  $V_x = 502 (\pm 50)$  km/s.

Depicted by the green trace are the simulation results when  $V_x$  values are doubled and  $N_p$  values are reduced by a factor of four. We make qualitative comparisons with the blue trace since the Polar observations are not exactly replicated. The rise/fall times in all the components are more rapid than the results the simulation results in the blue trace where inputs were not modified. In this simulation full compression of the field is reached six minutes after the SI onset. The SI duration is more than two minutes shorter than the initial simulation, which is exemplified by a shaper gradient in the time series profile of  $B_T$ . For this simulation  $V_S = 1005 (\pm 101)$  km/s, which is twice the value in the original simulation. Thus, doubling the solar wind speed hastens magnetospheric compression by 135 seconds.

Depicted by the red trace are the simulation results when  $V_x$  values are increased by a factor of 1.5 and  $N_p$  values are reduced by a factor of 2.25. The rise/fall times in these traces are more rapid than the blue trace, but less so than the green trace, as expected. In this simulation full compression of the field is reached 6.5 minutes after the SI onset. For this simulation  $V_S = 753 (\pm 75)$  km/s. Thus, increasing the solar wind speed by a factor of 1.5 quickens magnetospheric compression by roughly 2 minutes.

This case study also investigates the effect on rise/fall times when  $V_x$  is decreased. Depicted by the purple trace are the simulation results when  $V_x$  values are

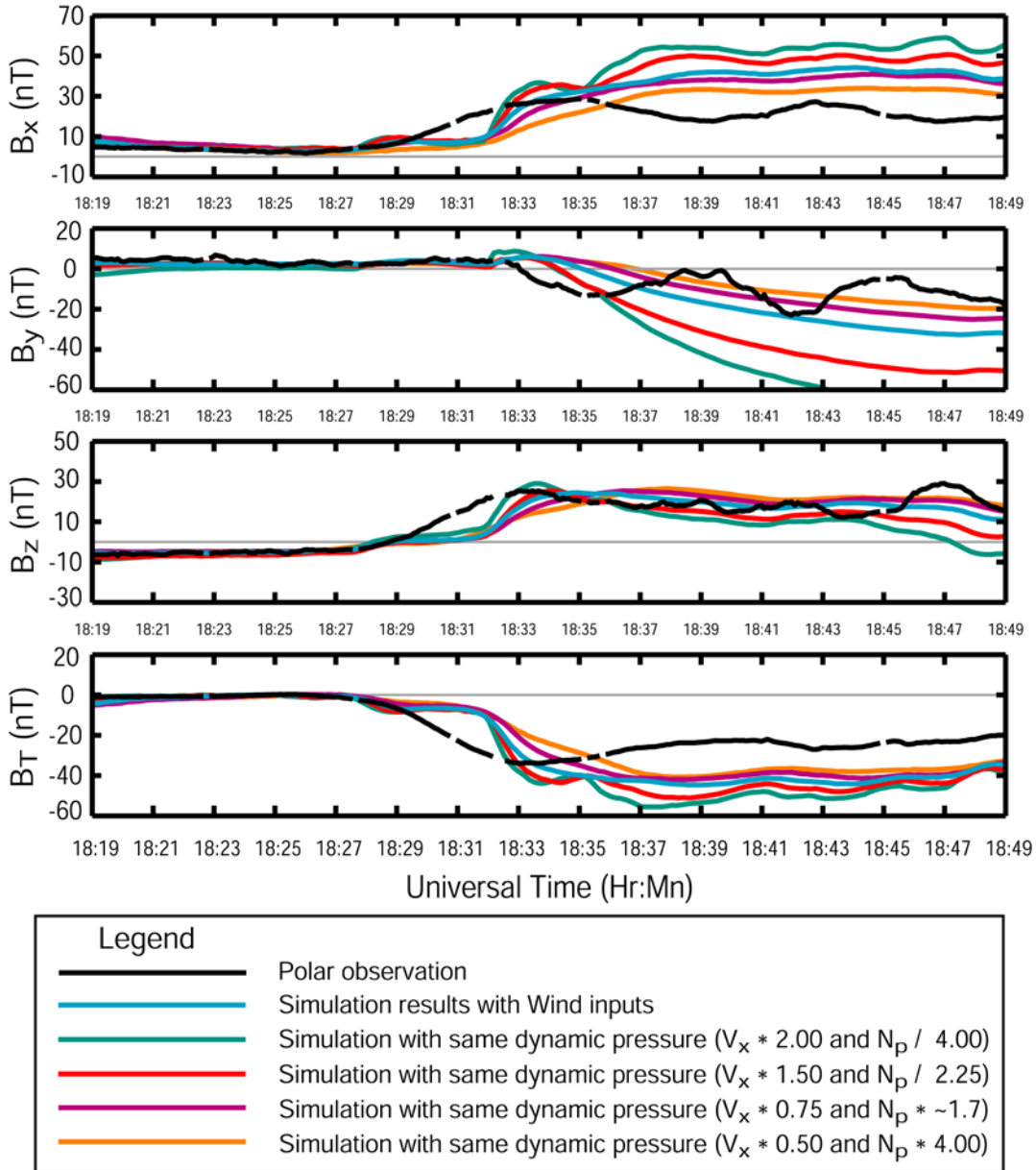


Figure 4.2: Time series plot of the SI observed by Polar on 9/28/96 (black trace) and the MHD simulation results (blue trace). MHD results from simulations with modified inputs are also presented. The green and red traces are associated with increases in solar wind speed. The purple and orange traces are associated with decreases in solar wind speed.

reduced by 25% and  $N_p$  values are increased by a factor of 1.7. Not surprisingly, reducing solar wind speed has the opposite effect of increasing the speed, which is apparent by a more gradual gradient in the time series profile. In this simulation full compression is reached 9.5 minutes after SI onset. For this simulation  $V_S = 377 (\pm 38)$  km/s, which is three-quarters of the value in the original simulation. Thus, reducing solar wind speed by a fourth will lengthen the compressional signal by approximately 30 seconds.

Finally, depicted by the orange trace are the simulation results when  $V_X$  values are reduced by 50% and  $N_p$  values are increased by four. The rise/fall times in the orange trace is even less pronounced than seen in the purple trace, and full compression is reached 10 minutes after SI onset. For this simulation  $V_S = 251 (\pm 25)$  km/s, which is half of the value in the original simulation. Thus, reducing solar wind speed by half will prolong the compressional signal by approximately 90 seconds.

#### *4.2.3 Summary*

We found that SI rise times are dependent on the speed of the solar wind structure when it moves along the exterior of the magnetosphere. MHD simulations of SIs are used to verify this theory. Two Polar observations of SIs are replicated with the MHD model. Several simulations were run with  $V_X$  and  $N_p$  values were modified while all other parameters are left at their observed quantities. We compared the dynamical change in the SI signals, and found that the duration of the SI is dependent on  $V_X$ . We

found that when the solar wind speed is increased the duration of the SI is completed more rapidly, and conversely, when the solar wind speed is decreased the duration of the SI is prolonged. In all simulations of each case study dynamic pressure values are consistent, thus we conclude that  $\partial B/\partial t$  is dependent on the only modified input parameter, solar wind speed. This dependence is confirms our expectations of the physical model. The more rapidly a solar wind structure moves along the exterior the sooner the compressional signal is fully communicated *in situ* throughout the magnetosphere.

### 4.3 Geoeffective length

*Takeuchi et al.* [2002] defines the geoeffective magnetopause as the region from which a compressional signal continues to be detected within the near Earth magnetosphere. Thus, the anti-sunward distance from the sub-solar point that a solar wind front sweeps along the exterior of the magnetosphere is known as the geoeffective length. *Ondoh* [1963] estimated a geoeffective size of 17-26  $R_E$  from compressional events observed at low and middle latitude stations, whereas *Nishida* [1966] determined the geoeffective length to be roughly 20-30  $R_E$ .

The events in this statistical study are used to determine a geoeffective length from inverse rise time and the speed of shock that triggers an SI. Shown in Figure 4.3 is a scatter plot of the inverse rise times as a function of shock speed in the  $X_{GSM}$  direction. Illustrated by the linear best fit is the slope used to calculate a geoeffective length of 18.7

$R_E$  for the 58 shock-triggered SIs observed by Polar. An assumption is used which characterizes the shock speed in solely the  $-X_{GSM}$  direction. This assumption is justified because of the uncertainty associated with the determination of shock normals.

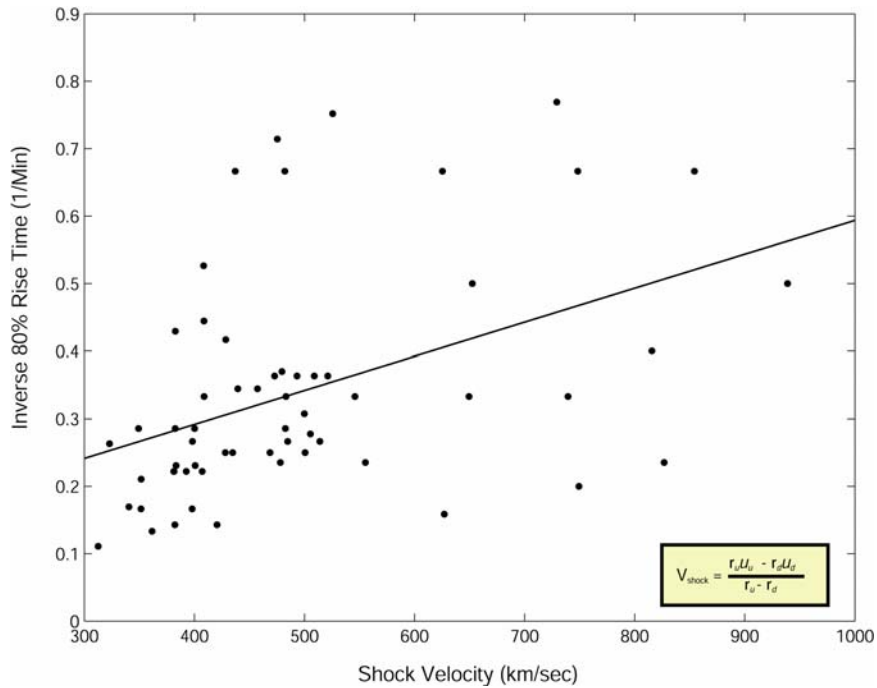


Figure 4.3: Plot of the inverse SI rise times as a function of the shock velocity. The slope of the best fit line is used to calculate the geoeffective length for the entire data set.

Previous investigation of rise time dependence has shown that dayside compressional signals are fully detected more rapidly than *in situ* measurements on the nightside [Ondoh, 1963]. For this reason the geoeffective lengths have been determined based on the location of the *in situ* measurements. Thus, the event pool is sorted according to SIs observed on the dayside or nightside, as well as at high latitudes or low latitudes. In Figure 4.4 is the same scatter plot as seen in Figure 4.3, except that dayside and nightside SI observations are color coded as red and black, respectively.

Additionally, symbols are used to indicate whether an event is observed at high latitudes (represented with “ $\Delta$ ”) or at low latitudes (represented with “ $\bullet$ ”). Median fits for these subsets are plotted and the slopes of these fits are used to calculate respective geoeffective lengths where solid lines are used to indicate the low latitude events and the dashed lines for high latitude events. The low and high latitude dayside events have respective geoeffective lengths of  $19.1 R_E$  and  $11.0 R_E$ . The low and high latitude events on the nightside have respective geoeffective lengths of  $21.2 R_E$  and  $20.5 R_E$ . Geoeffective lengths determined for nightside events are slightly longer, which is attributed to greater sensitivity in this region to the compression of the distant tail. Only

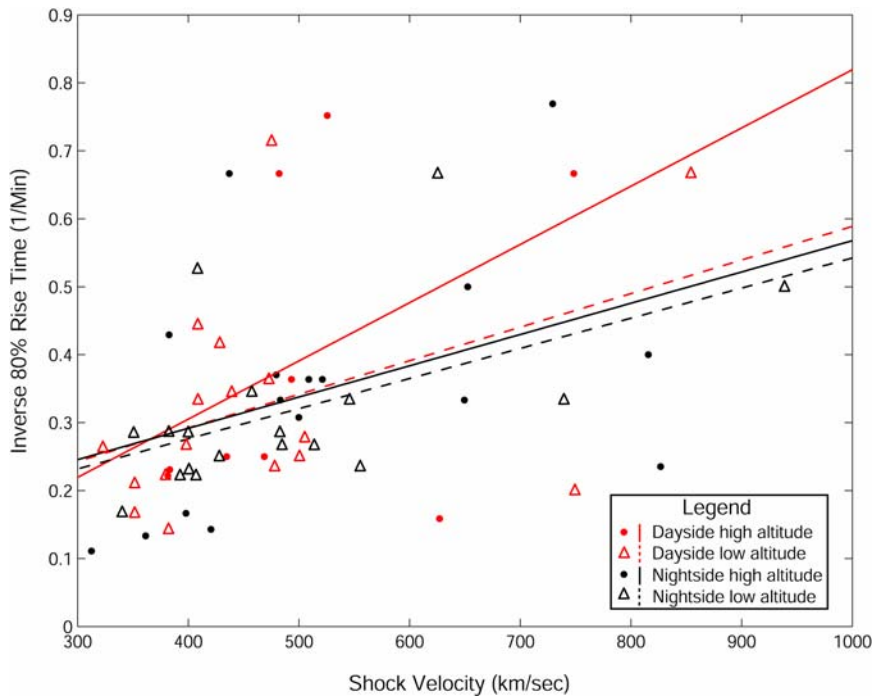


Figure 4.4: Plot of the inverse SI rise times as a function of the shock velocity. Data are sorted according to local time and latitude of the SI occurrence. The slopes of best fit lines are used to determine the geoeffective lengths.

the high latitude dayside region predicts a significantly shorter geoeffective length, which is consistent with previous research [Ondoh, 1963]. Dayside regions are more likely to experience full compression prior to the nightside because dayside regions are less susceptible to compressional signals transmitted from the far tail. Due to the complex geometry and a small event pool the geoeffective length for smaller. A more extensive statistical survey of this phenomenon throughout all regions of the magnetosphere would provide a more accurate analysis of the regional dependence of SI rise times.

#### **4.4 Summary and Conclusions**

Faraday's law states that changes in magnetic fields generate an electric field capable of accelerating particles. Geomagnetic fields are perturbed when an interplanetary shock compresses the magnetosphere, and local plasma is energized depending on how rapidly the compressional signal is received *in situ*. In this chapter we investigated the SI rise time dependence on solar wind speed. We have shown that rise times are directly related to the speed of a solar wind structure that moves along the exterior of the magnetosphere. This information is also useful in determining the geoeffective length, which is the distance from which a compressional signal is detected *in situ* throughout the magnetosphere.

The effect of shock speed on the SI rise times was investigated with an MHD model. This model simulated two Polar observations of SIs, which were used as guides for a qualitative analysis of shock speed dependence. Additional simulations were run

with modifications to solar wind speed and particle density while other input parameters were maintained at the originally observed values. Solar wind dynamic pressure values were maintained for each additional simulation so that only the effects of solar wind speed were investigated. Time series plots of magnetic fields show that larger solar wind speeds change magnetic fields more rapidly, and slower solar wind speeds prolong the duration of the magnetic field changes. As a solar wind structure moves along the exterior of the magnetosphere a compressional signal will continue to be transmitted to locations throughout the magnetosphere until the structure reaches the geoeffective length. It is logical that faster solar wind structures will propagate more quickly towards the geoeffective length, thus locations throughout the magnetosphere will measure full compression more quickly.

Geoeffective lengths are calculated for this data set by using the linear best fit from investigating the rise time dependence on shock speeds. We find an average geoeffective length of  $18.7 R_E$ , which is consistent with previous research [*Ondoh*, 1963; *Nishida*, 1966]. The geoeffective lengths were also calculated for SIs sorted according to magnetospheric regions. The most significant finding was that the calculated geoeffective lengths for dayside SIs were shorter, which is consistent with previous research [*Ondoh*, 1963].

## 4.5 References

Baumjohann, W., O. H. Bauer, G. Haerendel, and H. Junginger, Magnetospheric plasma drifts during a sudden impulse, *J. Geophys. Res.*, 88, 9,287-9,289, 1983.

Burgess, D., *Introduction to Space Physics*, ed. M. G. Kivelson and C. T. Russell, Cambridge University Press, Cambridge, United Kingdom, 142-143, 1995.

Burlaga, L. F. and K. W. Ogilvie, Causes of sudden commencements and sudden impulses, *J. Geophys. Res.*, 74, 2,815-2,825, 1969.

Colburn, D. S., and C. P. Sonett, Discontinuities in the solar wind, *Space Sci. Rev.*, 5, 439-506, 1966.

Dessler, A. J. and E. N. Parker, Hydromagnetic theory of geomagnetic storms, *J. Geophys. Res.*, 64, 2,239-2,252, 1959.

Dessler, A. J., W. E. Francis, and E. N. Parker, Geomagnetic storm sudden-commencement rise times, *J. Geophys. Res.*, 65, 2,715-2,719, 1968.

Maeda, H., K. Sakurai, T. Ondoh, and M. Yamamoto, Solar terrestrial relationships during the IGY and IGC, *Ann. Geophysicae*, 18, 305, 1962.

Mayaud, P. N., Analysis of storm sudden commencements (SSC) for the years 1868-1967, *J. Geophys. Res.*, 80, 111, 1975.

Nishida, A., Transmission of storm sudden commencements through the interplanetary space; shock wave mode and non-shock mode, *Rep. Ionos. Space Res. Japan*, 18, 295, 1964.

Nishida, A., Interpretation of SSC rise time, *Res. Ionos. Space Res. Japan*, 20, 42-44, 1966.

Ondoh, T., Longitudinal distribution of SSC rise time, *J. Geomagnetism and Geoelectricity*, 14, 198, 1963.

Pisharoty, P. R. and B. J. Srivastava, Rise times versus magnitudes of sudden commencements of geomagnetic storms, *J. Geophys. Res.*, 67, 2,189-2,192, 1962.

Raeder, J., Y. L. Wang, and T. J. Fuller-Rowell, Geomagnetic storm simulation with a coupled magnetosphere-ionosphere-thermosphere model, in *Space Weather*, ed. P. Song, H. Singer, and G. Siscoe, *Geophysical Monograph Series*, Vol 125, 2001.

Takeuchi, T., C. T. Russell, and T. Araki, Effect of the orientation of interplanetary shock the geomagnetic sudden commencement, *J. Geophys. Res.*, 107, doi:10.1029/2001JA900152, 2002.

Wilken, B., C. K. Goertz, D. N. Baker, P. R. Higbie, and T. A. Fritz, The SSC on July 29, 1977 and its propagation within the magnetosphere, *J. Geophys. Res.*, 87, 5901-5910, 1982.

## Chapter 5: ULF Wave Activity due to Magnetospheric Compression

### 5.1 Introduction

In previous chapters we found that magnetospheric compression by the solar wind will increase and decrease the global geomagnetic field. In this section we investigate the growth of Pc 1-2 waves that are generated as a result of the compression. We illustrate this phenomenon by comparing power spectra from five minute intervals upstream and downstream of the observed SIs listed in Appendix 2. We find that Pc 1-2 waves are noticeably increased up to orders of magnitude in the transverse power for 17 of 50 SI events triggered by magnetospheric compression. We additionally find that three events exhibit a decrease in ULF wave amplitude when the magnetosphere is compressed. Further, we compare the relative effect of other parameters affecting the occurrence rate. These wave phenomena are generated when an increase in solar wind dynamic pressure does work on the magnetosphere by displacing the magnetopause boundary Earthward. This work energizes the inner magnetosphere by accelerating gyrating ions perpendicular to the field. The duration of an SI is slow relative to the particle motions along the ambient field. This assumption ensures conservation of the first adiabatic invariant ( $\mu = mv_{\perp}^2/2B$ ), so any change in the magnetic field directly affects the perpendicular motion of the particles. Thus, an adiabatic compression of plasma particles generates a preferential gain in particle energy perpendicular to the magnetic field. The development of an anisotropic distribution of particles ( $T_{\perp} > T_{\parallel}$ ) is shown to be unstable to the growth of

ion-cyclotron waves [Cornwall, 1965; Lin and Parks, 1976; Olson and Lee, 1983].

When particle energy is transferred into wave energy by Doppler-shifted cyclotron resonance, particle pitch angles decrease and left-handed elliptically polarized waves are generated. Illustrated in Figure 5.1 is the effect of the cyclotron resonances on a single ion in which the particle loses energy and the wave gains energy. The left panels represent the conditions prior to magnetospheric compression and panels 2 and 3 are post-compression. We compare the difference in wave power before compression (panel 1) and after compression (panel 3). We define a wave activity event as a change in the

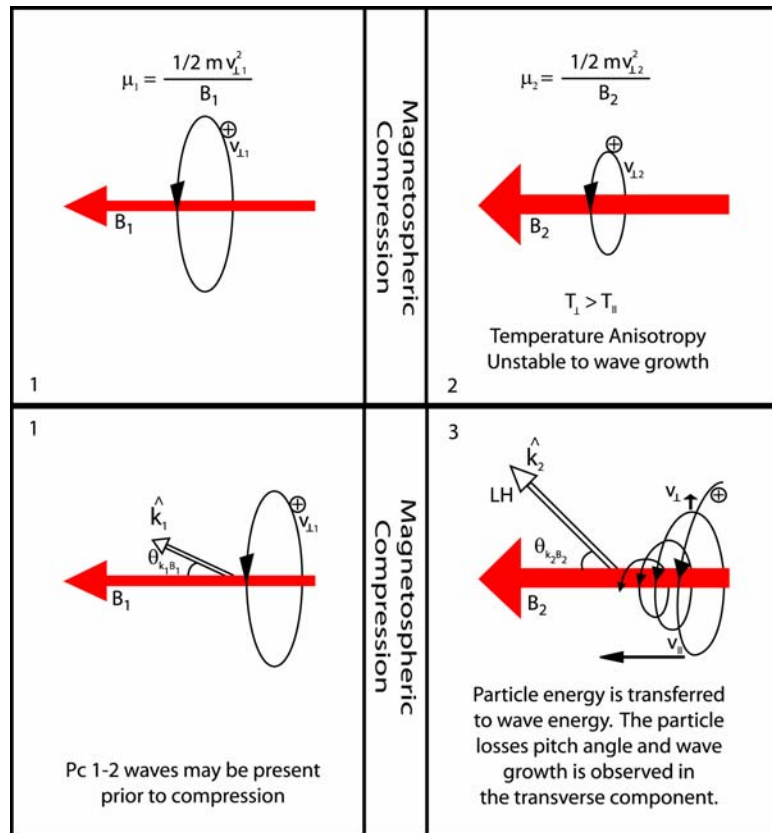


Figure 5.1: Illustration of ULF wave generation due to magnetospheric compression. The two left panels are pre-compression and the two right panels are post-compression.

transverse wave power ( $\text{nT}^2/\text{Hz}$ ) by at least an order of magnitude.

ULF waves are categorized according to the frequency of the continuous pulsations (Pc) as follows: Pc 1 are 0.2-5.0 Hz, Pc 2 are 0.1-0.2 Hz, Pc 3 are 22-100 mHz, Pc 4 are 7-22 mHz, and Pc 5 are 2-7 mHz. We statistically examine the regularity of Pc 1-2 wave growth resulting from magnetospheric compression along the Polar orbit. A similar study with ground-based magnetometers has shown that 32 of 76 compressional events led to significant ULF wave growth in the Pc 1-2 frequency band (0.1 - 1.0 Hz) [*Olson and Lee*, 1983]. Our rate of occurrence (40%) is consistent with the results from *Olson and Lee* (42%). Conversely, *Engebretson et al.* [2002] examined correlation between SIs and ULF waves by investigating 20 Pc 1-2 wave events with Polar and high-latitude ground magnetometers, and they found that 75% of these events were triggered by magnetospheric compression. *Anderson et al.* [1996] use a case study to assert that ULF waves serve as beacons for compression events, but we suspect that a compressional event does not guarantee ULF wave growth. Thus, we also examine additional parameters affecting the regularity of occurrence.

Previous studies investigated ULF wave growth triggered by magnetospheric compression when other factors are considered, such as the local time of the observations, the magnetospheric activity, and the magnitude of the SI [*Kangas et al.*, 1986]. Several studies argue that ULF emissions associated with magnetospheric compression occur preferentially near local noon at high latitudes [*Olson and Lee*, 1983, and references therein; *Kangas et al.*, 1986, *Anderson et al.*, 1996]. Another study suggests that the source region of Pc 1-2 waves is in the postnoon equatorial region, but

they do not proclaim which physical mechanism generates the micropulsations [Dryud *et al.*, 1997; Bolshakova *et al.*, 1980]. It has been shown that Pc 1 pulsations can gain energy from plasma sheet ions on open drift paths [Anderson *et al.*, 1992a, b], or from ions injected in the cusp/cleft region [Hansen *et al.*, 1992]. However, further research has shown that the cold plasma population plays a significant role in generating ULF wave growth [Lin and Parks, 1976]. Thus, we suggest that wave growth occurs in any region of the magnetosphere given the proper plasma distribution.

Another factor that may contribute to the generation of ULF waves triggered by an SI is the pre-existing magnetospheric conditions. Kangas *et al.* [1986] suggest that ULF pulsations are more likely to be observed when the magnetosphere is active allowing convecting plasma to contribute to temperature anisotropies. For this research they used the global planetary index,  $K_p$  (“planetarische Kennziffer”), which is recognized worldwide as a measurement of geomagnetic activity.  $K_p$  is measured by finding the mean irregular disturbance in 3-hour intervals for the two horizontal field components observed at selected subauroral stations, which are presented in a quasi-logarithmic scale ranging from 0 to 9. We observe wave activity events at all levels of magnetospheric activity and half of the non-events occurred when  $K_p > 3+$ .

Based on the physical mechanism of magnetospheric compression presented in Figure 5.1, it is reasonable that large amplitude SIs are capable of larger energization of plasma. It has been statistically shown that larger amplitude SIs are more likely to generate wave growth [Kangas *et al.*, 1986]. Despite the logic of this process previous research has also shown that moderate amplitude SIs are also capable of generating ULF

waves [Anderson and Hamilton, 1993]. Our examination of this problem shows that there is a variable range of SI amplitudes capable of generating Pc 1-2 waves. We also find that some of the largest amplitude compression events do not lead to ULF wave growth.

## 5.2 Observations and Results

Detrended high resolution Polar data are examined for ULF wave activity triggered by magnetospheric compression over the period April 1996 to December 2000. A high pass filter with a corner frequency at 0.08 Hz is applied to the high resolution magnetometer data. We compare transverse power spectra from 5-minute intervals before and after the SI observed at Polar. An increase in wave power indicates that there has been energy exchanged from particles to waves. For this study we define a wave activity event when there is an observable change in transverse wave power by at least an order of magnitude. We observe Pc 1-2 wave activity in 20 of 50 compressional events when the transverse wave power is greater than  $10^{-2}$  nT<sup>2</sup>/Hz at the time of compression. First, we examine four case studies of Pc 1-2 wave activity events. We use the mathematical method described by Means [1972] to determine the polarization properties of enhanced waves over selected frequency bands. The Means technique uses the imaginary part of the covariance matrix to determine such properties as the angle of wave propagation ( $\theta_{BK}$ ), the ellipticity (-LH/+RH), and the coherence of the non-linear portion of the wave. From this we determine the ratio of the weighted frequency relative to the

ion gyrofrequency ( $\Omega = qB/m$  where  $q$  and  $m$  are the charge and mass of a proton respectively, and  $B$  is the local background magnetic field). When necessary we preclude the discrete spin tones of Polar (6 seconds) to avoid biasing the statistical characteristics of the wave properties. In the last section we examine the occurrence rate of ULF wave events for the entire data pool. For this portion of the study we examine the dependence on SI location, SI magnitude, and magnetospheric activity.

### *5.2.1 Case Study: November 22, 1997*

Presented in Figure 5.2 is the detrended and filtered time series of the SI observed on November 22, 1997. We notice that there is a sustained increase in high frequency oscillations after compression occurs. For the time intervals indicated in Figure 5.2 we examine the transverse wave power as a function of frequency by applying a Fast-Fourier Transform (FFT). Presented in Figure 5.3 are the power spectral density functions the before and after the SI event. The red trace correlates to the transverse wave power prior to the onset of the SI (0942 – 0947 UT), and the black trace correlates to the transverse wave power downstream of the SI. There is an enhancement in power density ( $\text{nT}^2/\text{Hz}$ ) by approximately a factor of 10 that spans the Pc 1-2 frequencies (0.1 Hz to 0.3 Hz). The post-compression ULF waves generated are left-handed elliptically polarized. Other wave characteristics for these intervals are discussed later in this section. This ULF event represents the archetypical observed response.

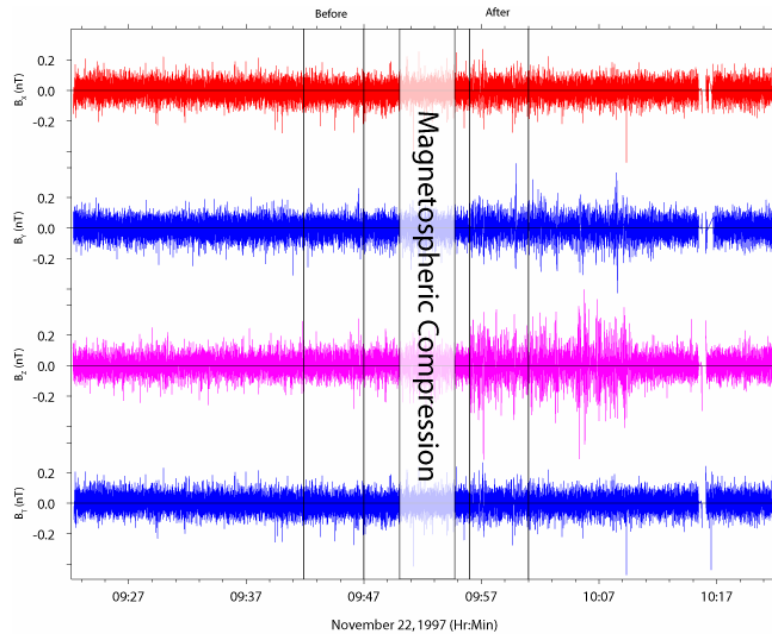


Figure 5.2: Detrended and filtered time series plot of magnetic field components observed by Polar on November 22, 1997.

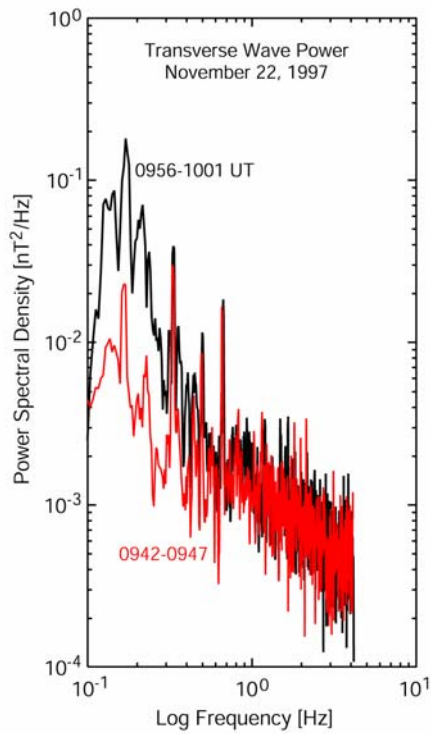


Figure 5.3: Power spectra of transverse waves before and after the SI observed on November 22, 1997.

### 5.2.2 Case Study: November 7, 1998

Presented in Figure 5.4 is the detrended and filtered time series of the SI observed on November 7, 1998. This wave growth event is 1 of 8 to be observed in a depression region where  $-\Delta B$  is observed as a result of magnetospheric compression (as described in Chapters 2 and 3). Wave growth is not dependent on  $\Delta B$ , thus we see the ULF activity in the field components when the transverse wave power is enhanced. Presented in Figure 5.5 is the power spectra change for the SI observed on November 7, 1998 where the red trace correlates to the interval prior to compression (0808 – 0813 UT) and the black trace

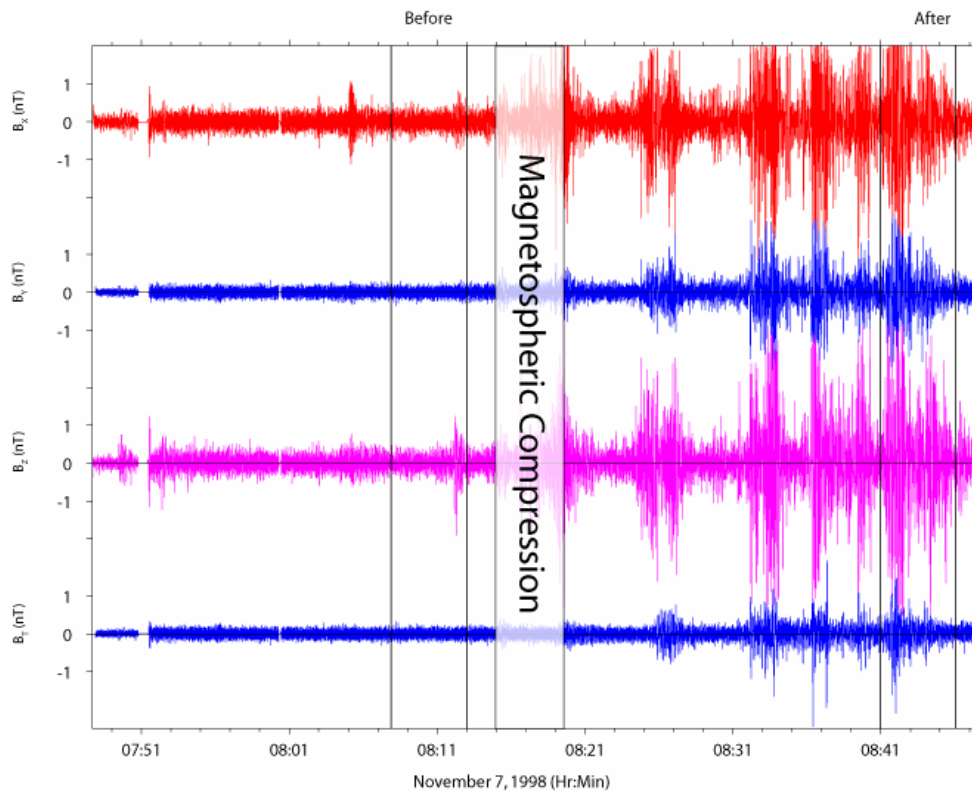


Figure 5.4: Detrended and filtered time series plot of magnetic field components observed by Polar on November 7, 1998.

correlates to the interval after the compression (0841 – 0846 UT).

The other interesting aspect about this particular event is that wave power is amplified over a broad range of frequencies (0.1 – 1.0 Hz). The broadband enhancement of emission intensity is a commonly observed occurrence [Kangas, *et al.*, 1986; and references therein]. Presented in Table 5.1 are the polarization properties of the enhanced downstream ULF waves over narrow frequency bands as indicated by the shaded stripes in the background of Figure 5.5.

The trace amplitude is representative of the wave power, and is calculated from the imaginary covariance matrix [Means, 1972]. The largest enhancement of waves was

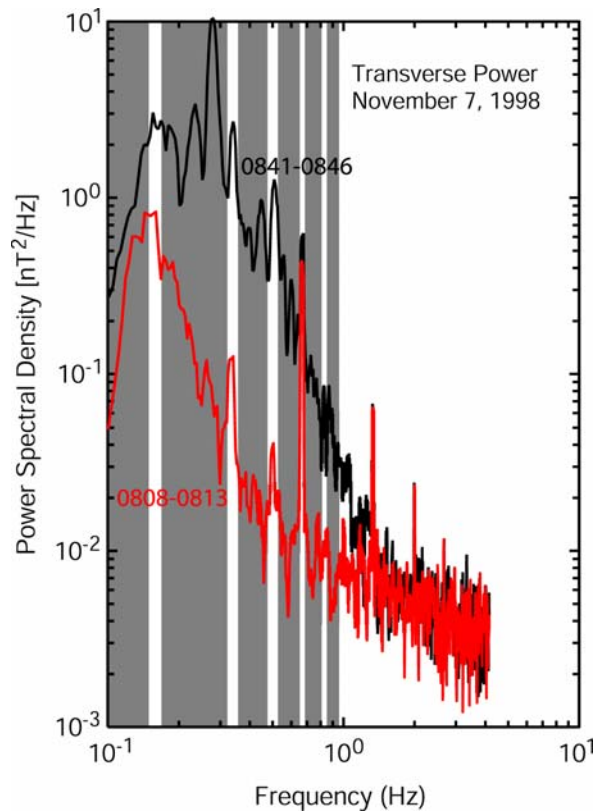


Figure 5.5: Power spectra of transverse waves before and after the SI observed on November 7, 1998.

centered around 0.24 Hz. The angle ( $\Theta_{kb}$ ) describes the orientation of the wave vector ( $\mathbf{k}$ ) relative to the background field ( $\mathbf{B}$ ). The wave vector travels away from the magnetic field for each frequency band investigated. The percentage of polarization is representative of the wave coherence. The level of coherence for each of these frequency bands is sufficiently large. The ellipticity is calculated from the dot product ( $\mathbf{k}\cdot\mathbf{B}$ ), and counterclockwise rotation looking down the magnetic field is right-handed ( $\mathbf{k}\cdot\mathbf{B} > 0$ ), whereas clockwise rotation is left-handed ( $\mathbf{k}\cdot\mathbf{B} < 0$ ). We find that the ULF waves generated are generally left-handed or very nearly linear. The ratio ( $f/f_g$ ) of the weighted frequency relative to the ion-gyrofrequency in the ambient background field, which is 486.5 nT. We note that the ratios should be less than unity because of the parallel Doppler shifting of the resonant wave by the parallel velocity of the ion [Fraser *et al.*, 1992]. This ULF event was selected for presentation because for each of the frequency

Frequency band (Hz)	Weighted frequency	Trace amplitude	$\Theta_{kb}$ (deg)	Percent polarization	Ellipticity (-LH/+RH)	$f/f_g$
0.10 – 0.15	0.13	0.76	66.4	86.9	-0.1	0.02
0.18 – 0.32	0.24	0.96	62.5	63.8	-0.0	0.03
0.35 – 0.47	0.41	0.56	21.5	39.5	-0.7	0.05
0.53 – 0.65	0.57	0.33	35.8	35.5	-0.3	0.08
0.69 – 0.82	0.73	0.28	82.8	88.4	0.1	0.10
0.85 – 0.95	0.90	0.20	18.1	41.9	-0.4	0.12

Table 5.1: Polarization properties of the enhanced transverse waves for several frequency bands downstream of the compressional event observed on November 7, 1998 (0841 – 0846 UT).

bands the enhancement of wave power is consistent with the physical model presented in Figure 5.1.

### 5.2.3 Case Study: August 6, 1998

Presented in Figure 5.6 is the detrended and filtered time series of the SI observed on August 6, 1998. Presented in Figure 5.7 is the power spectra change for the SI observed on August 6, 1998 where the red trace correlates to the interval prior to compression (0726 – 0731 UT) and the black trace correlates to the interval after the

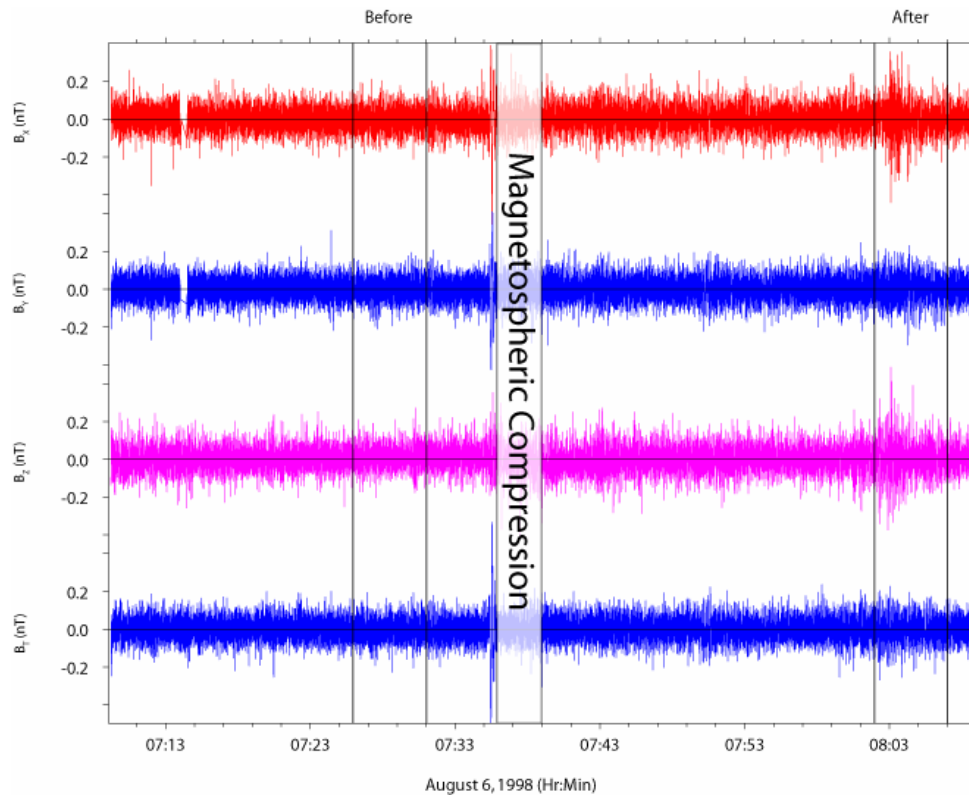


Figure 5.6: Detrended and filtered time series plot of magnetic field components observed by Polar on August 6, 1998.

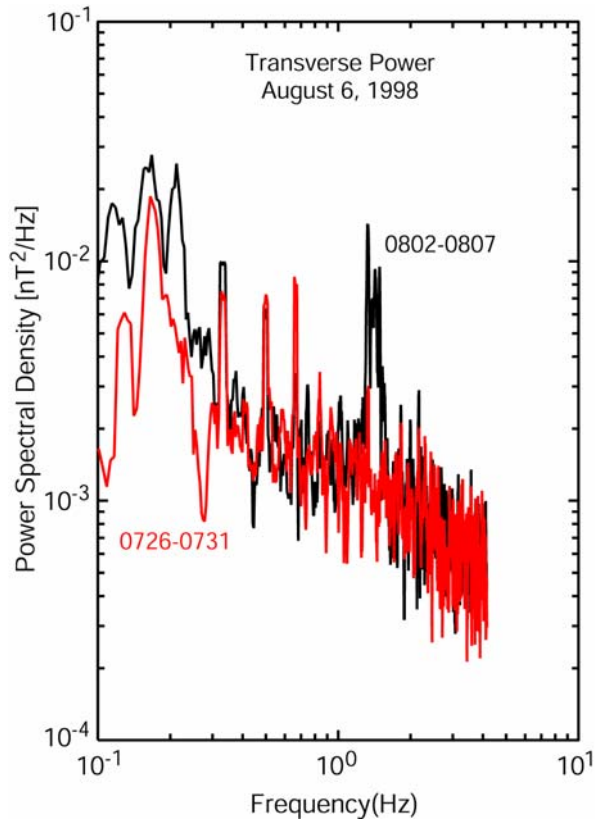


Figure 5.7: Power spectra of transverse waves before and after the SI observed on August 6, 1998.

compression (0802 – 0807 UT). *Fowler and Russell* [2001] first noticed an enhancement in the wave power across a discrete high frequency band for this event, but amplification at lower frequencies is not as dramatic. The change in polarization properties are listed in Table 5.2.

Time (UT)	Weighted frequency	$\Theta_{kb}$ (deg)	Percent polarization	Ellipticity (-LH/+RH)	$B_T$ (nT)	$f/f_g$
0716–0721	1.52	85.56	17.5	0.07	146.3	0.69
0803-0808	1.51	21.61	47.2	-0.03	198.9	0.50

Table 5.2: Polarization properties of Pc 1 frequency band on August 6, 1998 before and after magnetospheric compression is observed.

We notice that the wave generated is elliptically left-handed and the wave vector becomes more field aligned after the energy transfer. The center of the frequency band is roughly half of the ion gyrofrequency within this ambient magnetic field, and there is sufficient coherence of the wave to ensure confidence in the results. This high frequency Pc 1 enhancement is not observed elsewhere in this data pool.

#### 5.2.4 Case Study: January 27, 2000

Presented in Figure 5.8 is the detrended and filtered time series of the SI observed

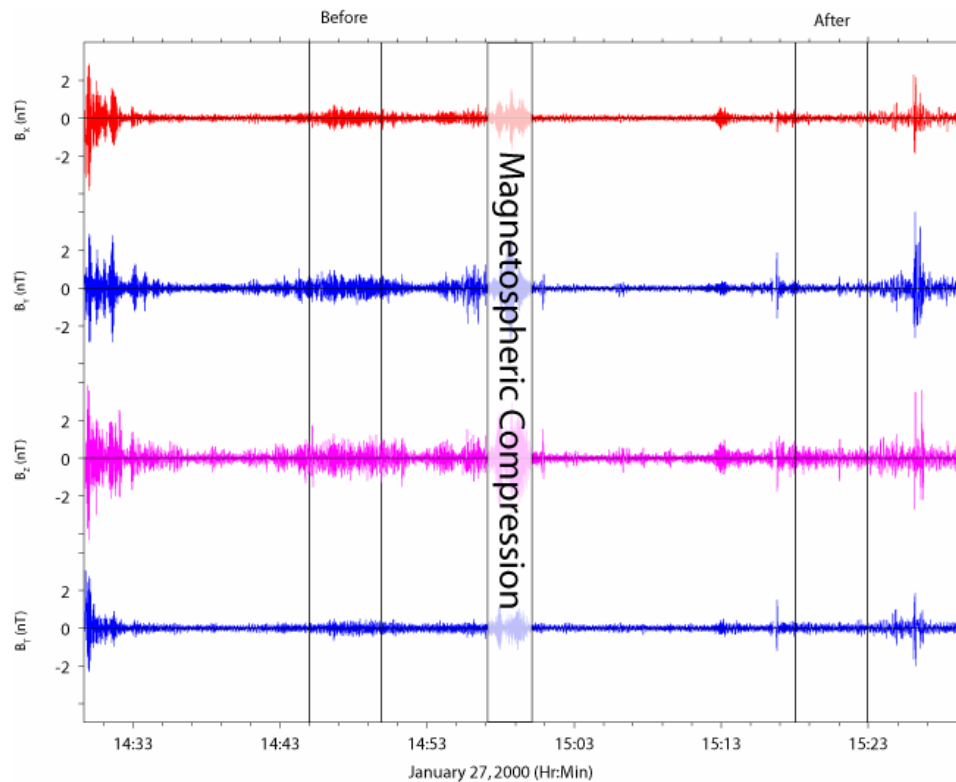


Figure 5.8: Detrended and filtered time series plot of magnetic field components observed by Polar on January 27, 2000.

on January 27, 2000. Presented in Figure 5.9 is the power spectra change for the SI observed on January 27, 2000 where the red trace correlates to the interval prior to compression (1445 – 1450 UT) and the black trace correlates to the interval after the compression (1513 – 1518 UT). There is a noticeable decrease in wave power by factors larger than 10, and across the Pc 1-2 band. This is one of three events that exhibited a post-compression decrease in wave power. *Lin and Parks [1976]* explain wave attenuation as a consequence of an influx of cold ions that reduce the temperature anisotropy. However, it is possible that Polar observations of apparent wave attenuation result from a spatial change. Prior to compression, Polar may reside in an unstable

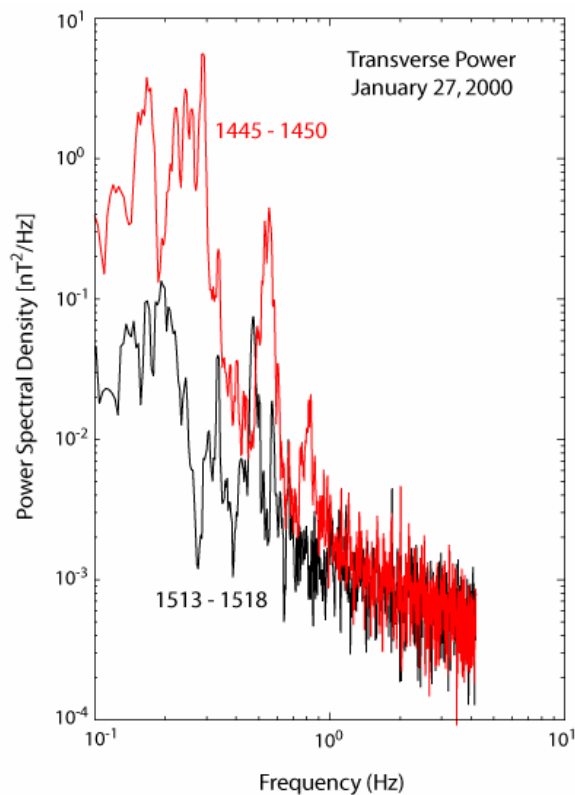


Figure 5.9: Power spectra of transverse waves before and after the SI observed on January 27, 2000.

plasma region and if it remains in this region after compression the instability is enhanced along with wave power. On the other hand, if compression repositions a stable plasma region around Polar then we will observe an apparent decrease in wave activity. The stable region is still susceptible to wave growth via the same physical mechanism, but waves relative to the pre-compression region may still have the appearance of wave attenuation. Relevant polarization properties before and after magnetospheric compression are listed in Table 5.3.

Time (UT)	Weighted frequency	Trace amplitude	$\Theta_{kb}$	Percent polarization	Ellipticity (-LH/+RH)	$B_T$ (nT)	$f/f_g$
1445-1450	0.24	0.48	19.6	86.0	-0.9	92.45	0.18
1512-1517	0.22	0.10	45.9	88.7	0.1	96.71	0.14

Table 5.3: Polarization properties of Pc 1 frequency band on January 27, 2000 before and after magnetospheric compression is observed.

### 5.2.5 Statistics of the data set

The four case studies above are representative of the physical model previously discussed. We observe similar ULF wave growth/attenuation events in 20 of 50 compressional events. We examine the wave characteristics for each of the ULF wave events by using the *Means* [1972] technique to compute the polarization properties. Presented in Table 5.4 are statistical characteristics of a post-compressional interval from each ULF wave event, or pre-compressional in the case of wave attenuation (9/28/96 and

3/20/97). Frequency intervals are selected for presentation based on the range that exhibited the largest increase (or decrease) in wave power without being dominated by spin tones. When frequency ranges exhibit similar increases in power the one selected for presentation has higher coherence.

Date	Time (UT)	Weighted frequency	$\Theta_{kb}$	Percent polarization	Ellipticity (-LH/+RH)	$B_T$ (nT)	$f/f_g$
7/28/96	1332-1337	0.12	3.48	62.2	-0.7	154.03	0.05
9/28/96*	1800-1805	0.40	18.0	74.8	-0.6	149.1	0.18
11/11/96	1553-1558	0.20	52.51	72.9	0.2	93.2	0.14
1/10/97	0121-0126	0.22	42.0	74.0	0.0	103.6	0.14
3/20/97*	2111-2116	0.22	33.0	65.7	-0.1	191.4	0.08
3/23/97	0910-0915	0.27	2.45	92.3	0.0	186.0	0.09
5/20/97	0625-0630	0.22	11.7	15.0	-0.5	325.5	0.04
9/2/97	2303-2308	0.22	43.3	67.2	0.1	154.9	0.09
11/22/97	0956-1001	0.14	68.1	24.0	-0.5	205.2	0.04
12/10/97	0548-0553	0.27	45.1	56.7	0.1	131.7	0.13
3/4/98	1216-1221	0.13	10.1	79.6	-0.3	139.9	0.06
8/10/98	0106-0111	0.13	83.5	97.9	-0.0	148.1	0.06
6/4/00	1516-1521	0.13	38.0	86.2	-0.0	691.1	0.01
6/8/00	0932-0937	0.12	29.4	46.3	-0.2	628.5	0.01
8/10/00	0508-0513	0.21	58.7	76.2	-0.1	96.4	0.15
9/6/00	1710-1715	0.14	23.8	48.4	0.1	216.8	0.04
11/10/00	0631-0636	0.13	72.7	65.4	0.1	183.8	0.05

Table 5.4: Polarization properties of Pc 1-2 frequency bands for each of the ULF wave events. Intervals selected represent the frequency band with the largest increase (or decrease) in transverse wave power and the highest coherence. Events labeled with an asterisk are the Pc 1-2 waves observed before compression, which undergo apparent attenuation.

### 5.3 Occurrence rate

We find that 20 of 50 compressional events listed in Appendix 2 are associated with the generation of Pc 1-2 waves as described by the physical model in Figure 5.1. While it is likely that magnetospheric compression is capable of generating ULF waves, it does not guarantee the occurrence. As mentioned above, previous research has suggested that local time, magnetospheric activity and SI magnitude play an important role in the enhancement of ULF waves [Kangas *et al.*, 1986]. We investigate the effect of these factors on the occurrence rate of ULF waves in our data set.

Illustrated in Figure 5.10 are the locations of the ULF events projected onto the equatorial plane in the GSM coordinate system. Illustrated in Figure 5.11 are the locations of the ULF events projected onto the noon-midnight in the GSM coordinate system. The red dots “•” correspond to the location of the three cases where a decrease in wave power was observed. Event dates listed in red correspond to  $-\Delta B$  events. We find that amplification of Pc 1-2 waves is possible in every region of the magnetosphere. Because of Polar’s orbit we observe compressional induced Pc 1-2 waves are not confined to the equatorial region. These waves may be generated locally as well as in the equatorial region. We also find seven events for which the wave power increases when the local field strength decreases. Two of these events occur in regions connected to the dayside equator where the field strength and wave growth should be enhanced despite the occurrence of  $-\Delta B$  at Polar. The remaining five events occurred when Polar was near the polar cusp. These events are consistent with Polar entering the noisy depressed field of

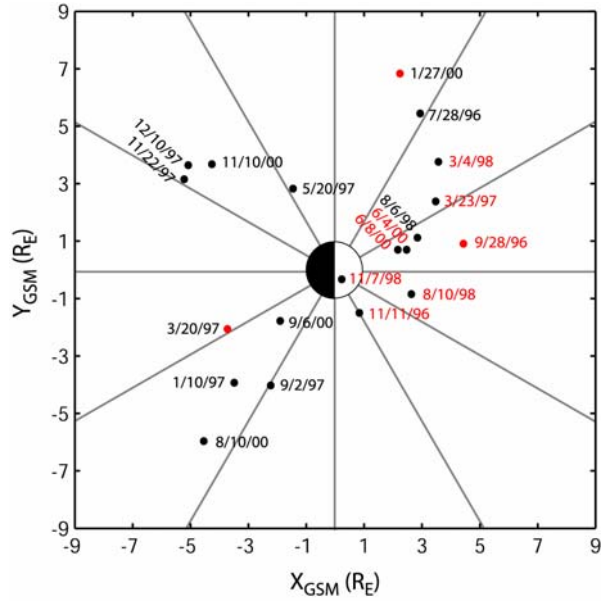


Figure 5.10: Locator plot of 20 SI events analyzed for wave activity projected onto the equatorial plane in the GSM coordinate system.

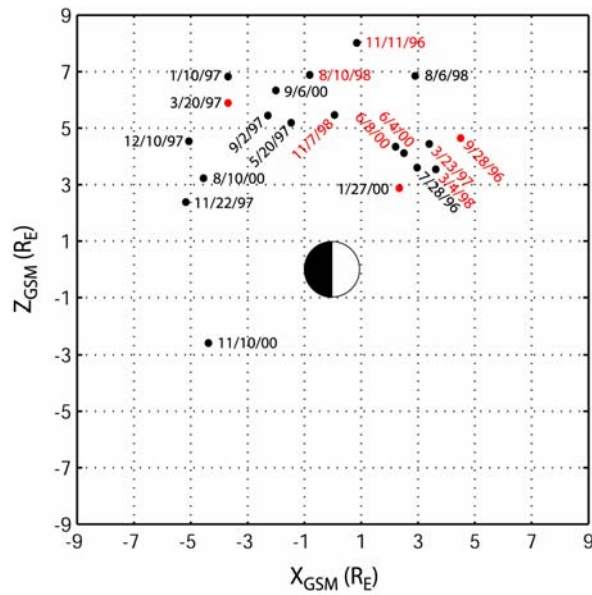


Figure 5.11: Locator plot of 20 SI events analyzed for wave activity projected onto the noon-midnight meridian in the GSM coordinate system

the cusp when the compression occurred. Of the three events that exhibited a decrease in power, one was connected to the equatorial region on the nightside where the field is expected to decrease upon compression of the magnetosphere. A second event occurred in a region where there was a local decrease in the field possibly decreasing the local growth rate. The third event was in the distant magnetosphere at low latitudes where the plasma moves large distances upon compression. Thus, the wave growth region may have moved away from Polar.

We also investigate the effect of magnetospheric activity on the occurrence rate of Pc 1-2 waves associated with SIs. We find that 20 of 50 compressional events exhibit Pc 1-2 wave activity when the transverse wave power is greater than  $10^{-2}$  nT<sup>2</sup>/Hz at the time that compression occurs. Shown in Figure 5.12 is the rate of Pc 1-2 wave growth

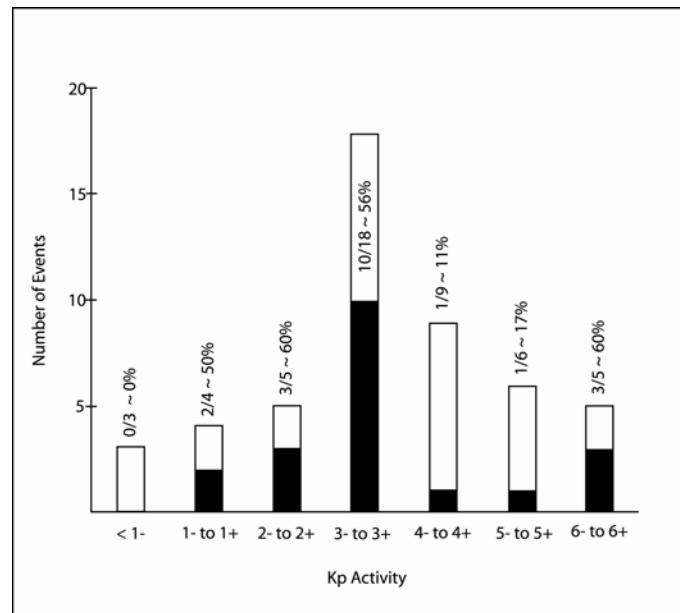


Figure 5.12: Rate of Pc 1-2 wave growth occurrence as a function of  $K_p$ .

occurrence as a function of  $K_p$ . We used the geomagnetic data from Kyoto University (<http://swdcd.db.kugi.kyoto-u.ac.jp/index.html>) to examine the  $K_p$  values associated with the compressional events. We find a quiet magnetosphere ( $K_p < 2^+$ ) associated with 5 of the 12 ULF events, and a highly active magnetosphere ( $K_p > 3^+$ ) was associated with another five cases. The remaining 10 events were associated with a moderately active magnetosphere ( $3^- \leq K_p \leq 3^+$ ). We found that 30 compressional events did not generate ULF waves, but half of these events occurred during an active magnetosphere ( $K_p > 3^+$ ). This evidence indicates that Pc 1-2 wave activity is not dependent on magnetospheric condition.

Lastly, we examine the amplitude of the SI for any correlation with ULF wave occurrence. *Kangas et al.* [1986] contend that larger amplitude SI are more likely to

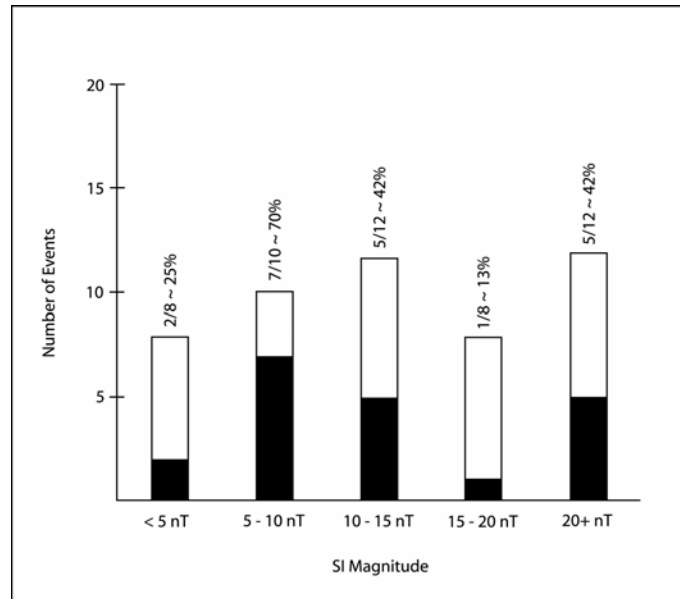


Figure 5.13: Rate of Pc 1-2 wave growth occurrence as a function of SI magnitude.

generate ULF waves. Shown in Figure 5.13 is the rate of Pc 1-2 wave growth occurrence as a function of SI magnitude. We find that 5 of 12 large SIs ( $|\Delta B| > 20$  nT) generate ULF waves. Moderate amplitude SIs ( $10 \text{ nT} < |\Delta B| < 20$  nT) generate ULF waves in only 6 of 20 cases. The occurrence rate increases for small amplitude SIs ( $5 \text{ nT} < \Delta B < 10$  nT) where we find 7 of 10 compressional events leading to ULF wave growth. Even for very small SIs ( $|\Delta B| < 5$  nT) we observe ULF waves after two of 8 compressional events. These results indicate that Pc 1-2 wave activity is possible for all SI magnitudes, especially for  $\Delta B$  values between 5 and 10 nT. However, for moderately large  $\Delta B$  values (15-20 nT) the occurrence rate is lower than the data set average (40%). Thus, we conclude that the SI magnitude does not guarantee the occurrence of Pc 1-2 wave activity.

#### **5.4 Summary and Conclusions**

We have shown that Pc 1-2 wave growth and attenuation is associated with magnetospheric compression. We observed broadband ULF wave growth in the Pc 1-2 frequencies, but there are also cases of enhancement in discrete frequency bands, including one example at high frequency (1.5 Hz). The observations of enhanced transverse wave power validate the physical model presented where Pc 1-2 wave growth as a result of magnetospheric compression. We also observed apparent wave attenuation when compression moves the plasma so that Polar resides in region more stable to wave growth than the pre-compression region.

We found that the energization of the inner magnetosphere plasma is possible when dynamic pressure fronts in the solar wind compress the magnetosphere. However, the occurrence rate of ULF wave growth does not indicate that magnetospheric compression guarantees the transfer of sufficient energy to produce instability deep within the magnetosphere. We found wave activity in 40% of our compressional events when Pc 1-2 wave power was greater than  $10^{-2}$  nT<sup>2</sup>/Hz at the time of compression. We did not find any spatial dependence for the occurrence rates of Pc 1-2 wave activity events. There does not appear to be any dependence on the magnetospheric activity since a nearly equal percentage of events occurred during quiet and active times. It is physically intuitive that larger compressional events are more capable of energizing the inner magnetosphere, but minor compressions are also capable of such an occurrence. We find that the occurrence rate of Pc 1-2 wave activity is not dependent on SI magnitude, location or magnetospheric activity. Magnetospheric compression has a 40% chance of generating a Pc 1-2 wave activity event by affecting the local plasma population. We recommend an analysis of the plasma energies with the TIMAS instrument on Polar to solve this problem, but this task is beyond the scope of this thesis.

## 5.5 References

- Anderson, B. J., R. E. Erlandson, and L. J. Zanetti, A statistical study of Pc 1-2 magnetic pulsations in the equatorial magnetosphere 1. Equatorial occurrence distributions, *J. Geophys. Res.*, 97, 3,075-3,088, 1992a.
- Anderson, B. J., R. E. Erlandson, and L. J. Zanetti, A statistical study of Pc 1-2 magnetic pulsations in the equatorial magnetosphere 2. Wave properties, *J. Geophys. Res.*, 97, 3,089-3,101, 1992b.
- Anderson, B. J., R. E. Erlandson, M. J. Engebretson, J. Alford, and R. L. Arnoldy, Source region of 0.2 to 1.0 Hz geomagnetic pulsation bursts, *Geophys. Res. Lett.*, 23, 769-772, 1996.
- Bolshakova, O. B., V. A. Troitskaya, and K. G. Ivanov, High latitude Pc 1-2 geomagnetic pulsations and their connection with location of the dayside polar cusp, *Planet. Space Sci.*, 28, 1, 1980.
- Cornwall, J. M., Cyclotron instabilities and electromagnetic emission in the ultra low frequency and very low frequency ranges, *J. Geophys. Res.*, 70, 61, 1965.
- Dyrud, L. P., M. J. Engebretson, J. L. Posch, W. J. Hughes, H. Fukunishi, R. L. Arnoldy, P. T. Newell, and R. B. Horne, Ground observations and possible source regions of two types of Pc 1-2 micropulsations at very high latitudes, *J. Geophys. Res.*, 102, 27,011-27,027, 1997.
- Engebretson, M. J., W. K. Peterson, J. L. Posch, M. R. Klatt, B. J. Anderson, C. T. Russell, H. J. Singer, R. L. Arnoldy, and H. Fukunishi, Observations of two types of Pc 1-2 pulsations in the outer dayside magnetosphere, *J. Geophys. Res.*, 107, SMP 20-1, doi:10.1029/2001JA000198, 2002.
- Fowler, G. J. and C. T. Russell, Geomagnetic field response along the Polar orbit to rapid changes in the solar wind dynamic pressure, *J. Geophys. Res.*, 106, 18,943-18956, 2001.
- Fraser, B. G., J. C. Samson, Y. D. Hu, R. L. McPherron, and C. T. Russell, Electro-magnetic ion cyclotron waves observed near the oxygen cyclotron frequency by ISEE 1 and 2, *J. Geophys. Res.*, 97, 3,063-3,074, 1992.
- Kangas, J., A. Aikio, and J. V. Olsen, Multistation correlation of ULF pulsation spectra associated with sudden impulses, *Planet. Space Sci.*, 34, 543-553, 1986.
- Korotova, G. I. and D. G. Sibeck, Generation of ULF magnetic pulsation in response to sudden variations in solar wind dynamic pressure, in *Solar wind sources of*

*magnetospheric ultra-low-frequency waves*, ed. M. J. Engebretson, K. Takahashi, M. Scholer, Geophysical Monograph Series, Vol. 81, 265-271, 1994.

Lin, C. S. and G. K. Parks, Ion cyclotron instability of drifting plasma clouds, *J. Geophys. Res.*, 81, 3919-3922, 1976.

Means, J., Use of the three-dimensional covariance matrix in analyzing the polarization properties of plane waves, *J. Geophys. Res.*, 77, 5551-5559, 1972.

Olsen, J. V. and L. C. Lee, Pc1 wave generation by sudden impulses, *Planet. Space Sci.*, 31, 295-302, 1983.

## Chapter 6. Conclusions

In this thesis we investigated the process known as magnetospheric compression, which is the physical response of the geo-magnetosphere to rapid changes in solar wind dynamic pressure. Interplanetary shock fronts and pressure pulses that travel within the solar wind interact with the magnetosphere boundary and move it Earthward. The magnetosphere responds with magnetic field perturbations to maintain the pressure balance along the boundary. Sudden impulses (SIs) are compressional signals measurable in space or on the ground as changes in the magnetic field. The breakthroughs we have made in understanding this phenomenon came from the global perspective made possible by the *in situ*, space-based observations from Polar.

There are three major results from this research. First, we establish a physical model of the global magnetospheric response, which includes depression regions where the magnetic field magnitude decreases ( $-\Delta B$ ) as a result of compression. We find these regions at high altitudes on the dayside and along the equator on the nightside. Secondly, we find that the SI rise time is dependent on the solar wind speed, which is confirmed with an MHD model. Finally, we find that magnetospheric compression can energize the inner magnetosphere, which is observed as an enhancement in transverse wave power. These findings are summarized below, along with how we approached these problems. As with any scientific research, new questions are raised, so we also discuss recommendations for future work.

## 6.1 Summary

### 6.1.1 Proposing the Potential Physical Models

We examined possible physical models that address the problem of magnetospheric compression globally. In Chapter 2 we propose three possible models that best describe the global magnetospheric response. *Araki* [1994] originally presented a physical model that describes magnetospheric response to northward perturbations, but the model is limited to the dayside equatorial region. Contrary to this model, *Fowler and Russell* [2001] observed  $-\Delta B$  in high latitude regions on the dayside away from the equator. To investigate this discrepancy we began with three steady state magnetospheric models known as T89, T96, and T01 [*Tsyganenko*, 1989, 1996, 2002a, 2002b]. We simulated a dynamic pressure front that interacts with the magnetosphere by applying a step function increase in solar wind dynamic pressure as the only input parameter. Changes in the magnetic field before and after the passage of the pressure front are used to predict the  $\Delta B$  global response. We illustrated the  $\Delta B$  global response with color contour plots along the noon-midnight meridian and orthogonal planes. All three models predicted a high altitude region on the dayside where  $\Delta B$  decreases as a result of the compression. This depression region has a volume shaped like a tear drop, which extends symmetrically several  $R_E$  away from the noon-midnight meridian and tapers off at lower altitudes near the Earth. Field perturbations generated by the compressed magnetopause current are anti-parallel to the background geo-magnetic field, which results in  $-\Delta B$ .

Only the T96 and T01 models predict an additional depression region along the nightside equator. In this region the compressed tail current generates field perturbations anti-parallel to the background field. Further, the T96 model predicts a third depression region which is concentric around the Earth. This feature is generated by the compression of the ring current. The T01 model uses only a partial ring current, so its compression generates a crescent shaped depression region which does not extend to the dayside. These are the three physical models considered for the phenomenon of magnetospheric compression.

We also investigated the effects of IMF orientation and dipole tilt on these potential models. In every case the other input parameters either shifted the location or intensified the response of the depression region, but the depression regions persisted. From this we conclude that pressure fronts traveling in the solar wind will always generate  $-\Delta B$  regions.

### *6.1.2 Choosing a Physical Model via Statistical Analysis*

We presented three possible physical models of magnetospheric compression based on a global response to a generic pressure pulse. When we compared the standardized predictions to Polar observations we found reasonable agreement on the location of the high altitude depression region. When we compared the standardized predictions to GOES observations we found reasonable agreement with the T96 and T01 models, but the T89 model does not predict any nightside  $-\Delta B$  values because it only

considers the compression of the magnetopause current. Discrepancies between the standardized models and observations are expected because there are unique parameters associated with each event. Now that we have qualitatively assessed the reasonableness of the three possible physical models, we must apply mathematical tests to verify which of these models is most appropriate. In addition, we apply the full complement of input parameters available for each model thereby ensuring the best possible replication of each *in situ* observation.

We used numerical fits between Polar and GOES observations and *in situ* model predictions from all three models. We found that the T01 model produced the most well correlated fits with both observational data sets. Regional variations were obvious with the T89 model, so we decided to test spatial variations due to local compressed currents. Thus, the T96 predictions were altered so that magnetic field contributions from the Birkeland, ring and tail currents were removed individually and jointly. Poor numerical fits would indicate the importance of the field contribution to the global compressional signal. We found that the compressed tail current was responsible for the generation of the nightside depression region and the compressed magnetopause current was responsible for the high altitude depression region. Altogether, the research in this chapter verified that the T01 model generates the best replication of the global magnetospheric response with the two separate depression regions.

Finally, we also calculated the response ratio ( $|\Delta B/\sqrt{p}| = 11.6 (\pm 2.8) \text{ nT/nPa}^{1/2}$ ) for the entire compressional event data set, which is comparable to previous research [e.g., *Siscoe et al.*, 1968; *Su and Konradi* 1975]. The magnetospheric response was also

categorized according to IMF orientation and local observation time and compared to previous research that also used these criteria to categorize ground-based data [Russell *et al.* 1994 a, b]. The results were surprisingly similar considering the ground-based data are affected by ionospheric currents. Ultimately, the response ratio provides a means by which we can parameterize the  $|\Delta B|$  response to dynamic pressure fronts in the solar wind. We also found that the response ratio is highest on the dayside during northward IMF.

### 6.1.3 SI Rise Time Dependence

In Chapter 4 we examined the dynamic aspect of the compressional signal. We began our investigation with two *in situ* Polar observations of SIs that were well replicated by an MHD model. We made additional simulations of these events after modifying the solar wind speed and particle density parameters, but without affecting the dynamic pressure. Intuitively, larger solar wind speeds will reduce the duration of interaction between the solar wind structures as they propagate quickly along the magnetosphere exterior. Thus, the magnetosphere reaches full compression sooner, which is seen as an SI with a steeper gradient. Conversely, lower solar wind speeds lead to a prolonged interaction, which is observed as a lengthy SI due to the slow compression of the magnetosphere.

In this chapter we also calculated the geoeffective length, which is defined as the distance downtail from the sub-solar point from which compressional signals continue to

be communicated to the near Earth magnetosphere [Takeuchi *et al.*, 2001]. We found a geoeffective length  $18.7 \pm 1.2 R_E$  for the entire data set. The data set was also analyzed for spatial dependence by binning the events according to the location of the observation. It was shown that the geoeffective length was much longer for nightside events ( $21.2 \pm 0.9 R_E$  and  $20.5 \pm 1.1 R_E$  for low and high altitude respectively), which is attributed to the higher sensitivity to the compression of the distant tail. The dayside events at high altitudes were found to have the shortest geoeffective length of  $11.0 \pm 0.9 R_E$ , which is consistent with previous research [Ondoh, 1963].

#### *6.1.4 Energizing the Inner Magnetosphere*

In Chapter 5 we examined the generation of ULF waves as a result of magnetospheric compression. The physical model of wave growth describes the development of temperature anisotropy when the first adiabatic constant is conserved. Particle energy is transferred into wave energy, which is observed as an increase in the transverse wave power. From our data set we observed 17 cases of wave amplification and three cases of apparent wave attenuation, which were attributed to a spatial relocation of Polar. The wave growth events do not appear to have any spatial dependence, nor is there any correlation with magnetospheric activity. We did find that the occurrence rate of wave activity increases with the magnitude of the SI, which is consistent with previous research [Kangas *et al.*, 1986]. From this research we concluded that energizing the

plasma in the inner magnetosphere to the point of ion cyclotron wave growth via compression is possible, but not guaranteed.

## **6.2 Conclusions**

From this investigation of magnetospheric compression we draw three prominent conclusions. First, we have established a new physical model of the global magnetospheric response to rapid changes in the solar wind dynamic pressure. We expect to observe  $-\Delta B$  values at high altitudes on the dayside in the vicinity of the cusp where field perturbations are anti-parallel to the background field. We also anticipate an additional depression region along the nightside equator, which is primarily generated by the compressed tail current, with contributions from the partial ring current. The second discovery in this thesis is the correlation between the solar wind speed and the rise time of the SI. Fast propagating solar wind structures will compress the magnetosphere rapidly and steepen the gradient of the SI signal, whereas slow propagating structures will prolong the interaction and extend the duration of the SI signal. Finally, we determined that magnetospheric compression is likely to energize the inner magnetosphere, thereby generating ULF waves, but the probability of occurrence is not guaranteed (33%). With these prominent discoveries we can conclude that we have successfully defined a new physical model of magnetospheric compression, and additionally answered questions about other effects associated with the phenomenon.

### 6.3 Recommendations for Future Work

The work presented here has benefited from an optimal spacecraft orbit that allowed us to investigate a magnetospheric region not previously studied. We could continue to take advantage of Polar's orbit in the coming years of the mission. Currently, the apogee of Polar's orbit is in the vicinity of equatorial plane bringing it annually near the sub-solar point. In the upcoming years, the apogee of the orbit will reach high altitudes in the southern dayside hemisphere. It would be a simple task to gather new compressional events observed in the southern hemisphere and perform the same analysis as described throughout this thesis. We initially assumed that our new physical model exhibits symmetry about the equatorial plane. However, when there is a finite tilt of the dipole to the solar wind flow this symmetry will be broken. We cannot accurately study this asymmetry without southern hemisphere data because the seasonal change of dipole tilt is tied to the annual apparent "precession" of the line of apsides from noon to midnight and back. The additional southern data would resolve the question of spatial symmetry between the northern and southern hemispheres at times of finite tilt. Further, increasing the compressional event data set would improve the robustness of the statistics.

Our second recommendation stems from the research involving ULF wave growth. We suggest using the TIMAS instrument onboard Polar to analyze the plasma energy before and after the compressional events. With this data we could resolve changes in the energy distribution of the plasma by investigating the change in

anisotropy. This would allow us to quantify the amount of energy transferred from the particles to the waves. Since we also know certain characteristics of the waves generated, we would be able to determine the ion population of the plasma. Ions (e.g., He<sup>+</sup> or O<sup>+</sup>) that gyrate around the field lines will generate ULF resonances at specific frequencies. We certainly have the ability to correlate magnetospheric compressions with the re-distribution of the ambient plasma.

## 6.4 References

- Dessler, A. J. and E. N. Parker, Hydromagnetic theory of geomagnetic storms, *J. Geophys. Res.*, 64, 2,239-2,252, 1959.
- Kangas, J., A. Aikio, and J. V. Olsen, Multistation correlation of ULF pulsation spectra associated with sudden impulses, *Planet. Space Sci.*, 34, 543-553, 1986.
- Mayaud, P. N., Analysis of storm sudden commencements (SSC) for the years 1868-1967, *J. Geophys. Res.*, 80, 111, 1975.
- Ondoh, T., Longitudinal distribution of SSC rise time, *J. Geomagnetism and Geoelectricity*, 14, 198, 1963.
- Pisharoty, P. R. and B. J. Srivastava, Rise times versus magnitudes of sudden commencements of geomagnetic storms, *J. Geophys. Res.*, 67, 2,189-2,192, 1962.
- Raeder, J., Y. L. Wang, and T. J. Fuller-Rowell, Geomagnetic storm simulation with a coupled magnetosphere-ionosphere-thermosphere model, in *Space Weather*, ed. P. Song, H. Singer, and G. Siscoe, *Geophysical Monograph Series*, Vol 125, 2001.
- Russell, C. T., M. Ginskey, and S. M. Petrinec, Sudden impulses at low-latitude stations: Steady state response for northward interplanetary magnetic field, *J Geophys. Res.*, 99, 253-261, 1994a.
- Russell, C. T., M. Ginskey, and S. M. Petrinec, Sudden impulses at low latitude stations: Steady state response for southward interplanetary magnetic field, *J. Geophys. Res.*, 99, 13,403-13,408, 1994b.
- Takeuchi, T., C. T. Russell, and T. Araki, Effect of the orientation of interplanetary shock the geomagnetic sudden commencement, *J. Geophys. Res.*, 107, doi:10.1029/2001JA900152, 2002.
- Tsyganenko, N. A., A solution of the Chapman-Ferraro problem for an ellipsoidal magnetopause, *Planet. Space Sci.*, 37, 1037-1046, 1989.
- Tsyganenko, N. A., Effects of the solar wind conditions on the global magnetospheric configuration as deduced from data-based field models, *Third International Conference on Substorms (ICS-3)*, 181-185, 1996.
- Tsyganenko, N. A., A model of the magnetosphere with a dawn-dusk asymmetry, 1. Mathematical structure, *J. Geophys. Res.*, doi:10.1029/2001JA000219, 2002a.

Tsyganenko, N. A., A model of the near magnetosphere with a dawn-dusk asymmetry, 2. Parameterization and fitting to observations, *J. Geophys. Res.*, doi:10.1029/2001JA000220, 2002b.

Siscoe, G. L., V. Formisano, and A. J. Lazarus, Relation between geomagnetic sudden impulses and solar wind pressure changes: an experimental investigation, *J. Geophys. Res.*, 73, 4869-4874, 1968.

Su, S. Y., and A. Konradi, Magnetic field depression at the Earth's surface calculated from the relationship between the size of the magnetosphere and *Dst* values, *J. Geophys. Res.*, 80, 195, 1975.

## Appendix 1: Density Intercalibration of Wind and ACE

### A.1 Introduction

The size of the magnetosphere is a function of the dynamic pressure of the solar wind, the product of the solar wind density and the square of its velocity [*Mead and Beard, 1964; Sotirelis, 1996; Sotirelis and Meng, 1999*]. Generally, solar wind velocity measurements are more accurate than density measurements. This is because velocity measurements use comparisons with a precisely controlled voltage, whereas density is determined by measuring a current over a finite energy range and an angular window may not include the entire solar wind flux. Determination of dynamic pressure in the solar wind with multiple solar wind detectors produces different results due to differences in instrument geometry and energy resolution and the different locations of the detectors combined with solar wind gradients. Differences were noted by *Fowler and Russell [2001]* when ACE and Wind observations of the plasma density and solar wind velocity to determine the size of the dynamic pressure changes that generated 13 sudden impulses (SIs) recorded by the Polar spacecraft. Discrepancies between simultaneous dynamic pressures measurements by the two spacecraft were as high as 39%. The intention of the previous work with these data sets was to develop an intercalibration that allows the plasma data to be used interchangeably when investigating SI triggers. This appendix presents an intercomparison so that error associated with dynamic pressure measurements can be estimated.

Previous intercalibrations with other solar wind monitors include IMP-8 and ISEE-3 [Russell and Petrinec, 1992; 1993; Petrinec and Russell, 1993; Richardson *et al.*, 1998], as well as SOHO and Wind [Coplan *et al.*, 2001]. Solar wind plasma flux correlation involving three spacecraft have also been calculated with IMP-8, Interball-1 and Wind [Paularena *et al.*, 1998]. Further, Maksimovic *et al.* [1998] provided a density comparison between the thermal noise receiver (TNR) and the Faraday cup detector onboard Wind yielding systematic differences. This work compares ACE and Wind plasma data sets from January 1998 to April 2000. By propagating plasma parcels between spacecraft the density measurements by Wind and ACE are investigated as a function of bulk speed and thermal speed.

## **A.2 SWEPAM instrumentation**

In Chapter 1 is a detailed description of the Solar Wind Experiment (SWE) onboard the Wind spacecraft, which consists of two Faraday cup sensors. The Solar Wind Electron Proton Alpha Monitor (SWEPAM) onboard ACE measures electron and ion distribution functions in three dimensions over all velocity space [McComas *et al.*, 1998]. The instrumentation consists of two electrostatic energy per charge ( $E/q$ ) analyzers with sets of channel electron multiplier (CEM) sensors for particle counting. The bias on the ion analyzer allows ions with a narrow range of energy per charge ( $\sim 5\%$ ) and azimuthal angular ( $3^\circ - 4.5^\circ$ ) to pass through the analyzer, which are detected by the CEM. The aperture of the sensor is oriented such that its fan-shaped field of view rotates

about the spacecraft spin axis. *McComas et al.* define the polar angle ( $\theta$ ) in the plane of the fan where  $0^\circ$  is parallel to the Sun-pointing spin-axis direction of the ACE spacecraft. The normal to the aperture is pointed  $\theta = 18.75^\circ$  away from the sunward direction. This allows SWEFAM to measure ions arriving at polar angles from  $0^\circ$  to  $\sim 65^\circ$ , which is sufficient to capture ions in the main solar wind beam ( $\theta < 25^\circ$ ). Due to the configuration of the sensors and spin the CEMs make a conical sweep with  $2.5^\circ$  polar angle resolution. SWEFAM make full 3-D plasma measurements of protons and alpha particles every 64 seconds over the energy range 260 eV/q to 36 keV/q.

### **A.3 Data Analysis**

*Fowler and Russell* [2001] concentrated on the measurements just before and after a set of interplanetary shocks. This study uses the entire coincident database from both spacecraft during the period from January 1998 to April 2001. Ten minute overlapping averages from both instruments are used to produce a time series with five minute resolution. Plasma parcels were propagated from ACE, which is close to the L1 point, to the Wind satellite at the radial solar wind velocity for each respective parcel detected by ACE. Propagated plasma parcels satisfied several criteria for selection in the data set to ensure that the parcels detected by both instruments were from the same relative plasma population. Samples are rejected when the Y-Z separation between the spacecraft is greater than  $50 R_E$  and also when the ratio of spacecraft solar wind speeds is between 0.9 and 1.1. If the velocities differ significantly, then the two spacecraft may be

measuring plasma on opposite sides of an interplanetary shock front or possibly the Earth's bow shock. To further restrict this last possibility samples were rejected whenever either spacecraft was within  $50 R_E$  of the Earth. This condition prevents sampling solar wind within the region upstream of the bow shock where solar wind properties are affected by their interaction with the upstream ions [Jurac and Richardson, 2001]. No plasma parcels are considered whenever either satellite is behind the Earth's dawn-dusk terminator to ensure that comparisons preclude magnetospheric or magnetosheath plasma. During the period from January 1998 to April 2001 this selection process consists of 90,508 samples in the comparative data set.

Displayed in Figures A.1, A.2, and A.3 are comparative plots of solar wind speed,

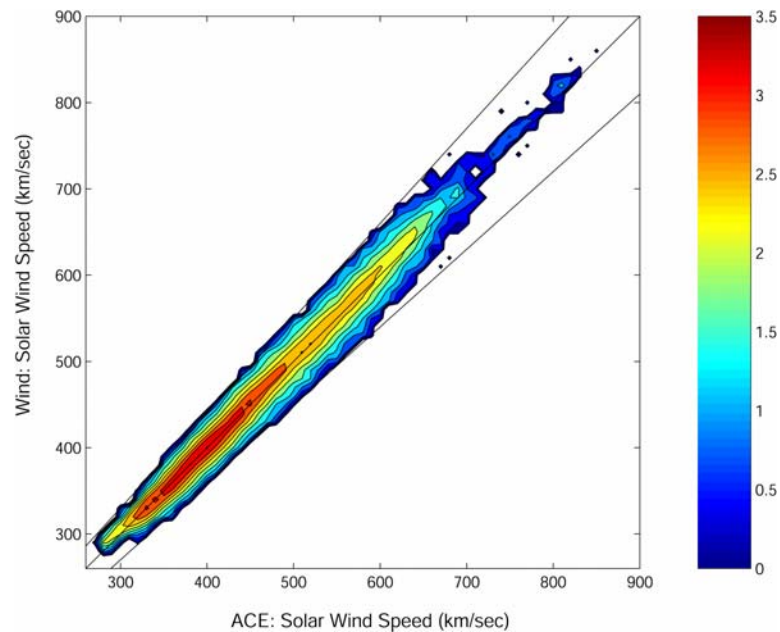


Figure A.1: Logarithmic distribution plot of ACE and Wind solar wind speed measurements. Linear constraints indicate correlation conditions placed on the data set, and the central linear plot represents unity.

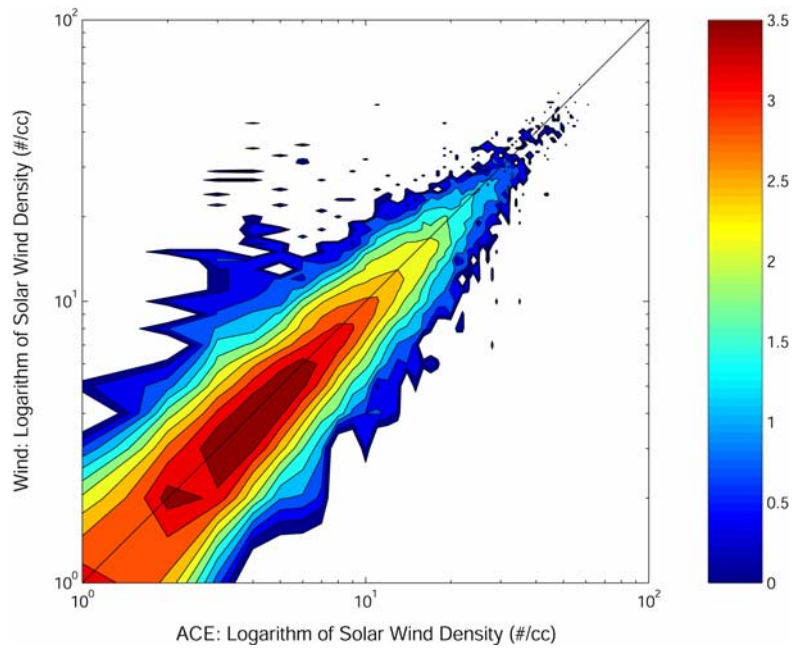


Figure A.2: Logarithmic distribution plot of ACE and Wind solar wind density measurements, which are scaled logarithmically along the abscissa. The central line represents unity of the measured quantity. The unity slope bisects the distribution function.

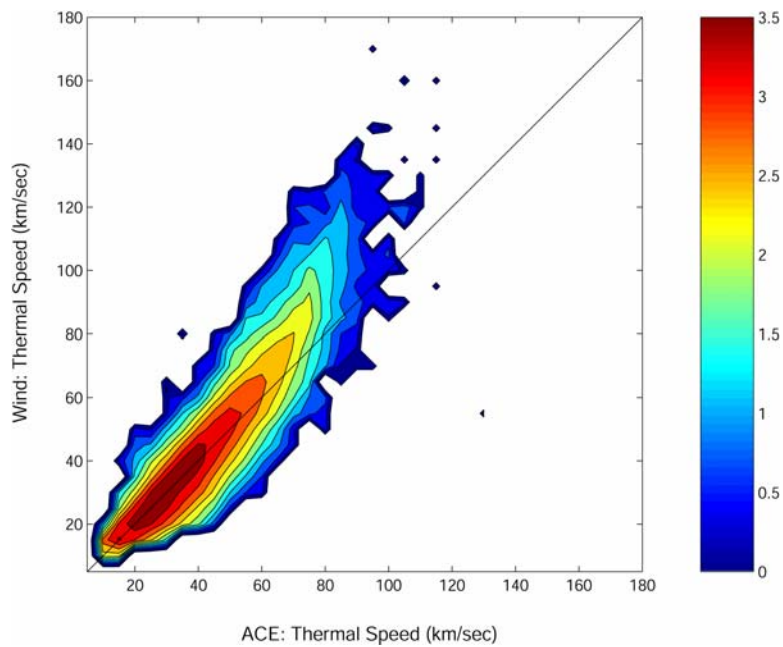


Figure A.3: Logarithmic distribution plot of ACE and Wind thermal speed measurements. ACE measures temperature in Kelvin, which is converted to thermal speed. The central line represents unity of the measured quantity. ACE measurements deviate from unity at high thermal speeds.

density and thermal speed respectively for the ACE and Wind spacecraft. The color scale for all three figures represents the logarithmic number density of the selected data set mentioned above. Figure A.1 shows the comparison between the solar wind velocities observed at the two spacecraft. The slope of unity depicted by the solid line bisects the data population which illustrates good correlation between the measurements. The outer solid lines illustrate the constraints used in the data set selection based on the ratio of the solar wind velocity, as mentioned above. Figure A.2 compares the measured densities on a logarithmic scale. Like Figure A.1 the unity slope bisects the comparative data set thus illustrating generally good agreement between spacecraft data sets. In Figure A.3 is the comparative data of the measured thermal speeds. ACE measures temperatures in Kelvin which have been converted to thermal speed as follows:

$$\text{(Eqn. A.1)} \quad v_T[\text{km/sec}] = (2kT_s/10^6 m_s)^{1/2}$$

where  $k = 1.3807 \times 10^{-23}$  J/K is the Boltzman constant,  $T_s$  is the measured temperature [K], and  $m_s = 1.6726 \times 10^{-27}$  kg is the proton mass. Good agreement is apparent for colder plasma, but as the thermal speeds increase ACE reports colder protons than Wind. This difference could be a result of the finite field of view for the electrostatic analyzer onboard ACE, which is  $80^\circ \times 10^\circ$  for ions and smaller than that of the Faraday Cup onboard Wind. The high temperature bias could also be a result of the different techniques used for the measurement of temperature. The electrostatic analyzer data onboard ACE measures the temperature as a moment analysis whereas the Faraday Cup

data onboard Wind fits the observed distribution function with an isotropic temperature (private communication Justin Kasper, 2001).

Although the median correlation seen in Figure A.2 is excellent the scatter among the 90,508 comparative density measurements seen in Figure A.4 warrants further investigation as it is not random. As shown below the ratio of the densities measured on

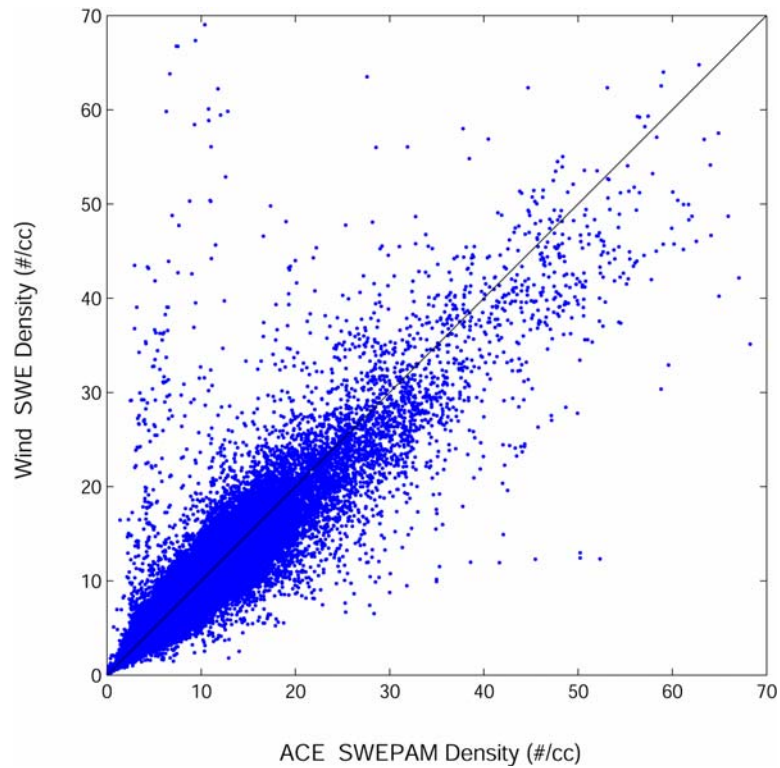


Figure A.4: Scatter plot of density measurements from the two spacecraft plotted on a linear scale.

different spacecraft is a function of other solar wind parameters. Figure A.5 shows the ratio of the Wind and ACE density measurements as a function of both solar wind speed and thermal speed. The color scale represents the ratio of proton number density

( $N_{p_{\text{Wind}}}/N_{p_{\text{ACE}}}$ ). The abscissa and ordinate of Figure A.5 are binned increments of 10 and 2 km/sec respectively for the bulk speed and thermal speed to produce the contours.

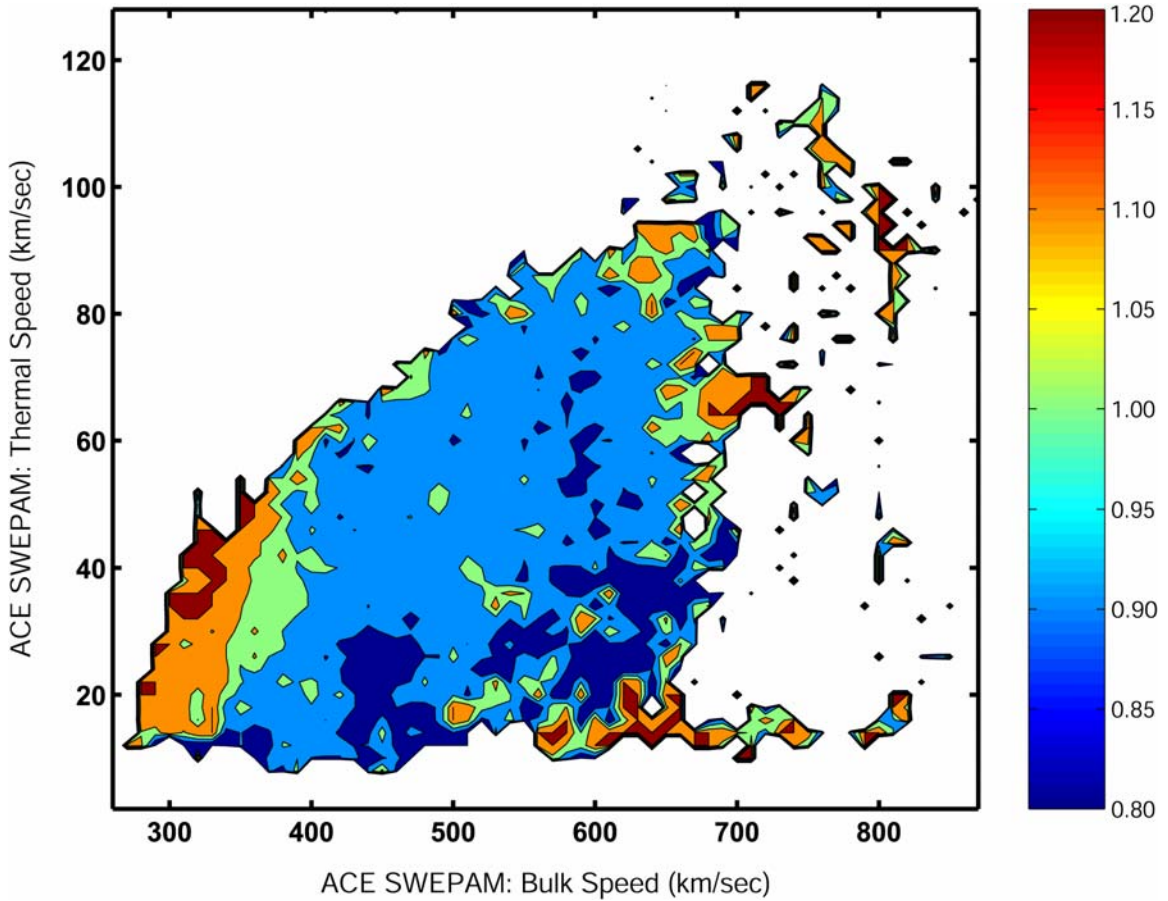


Figure A.5: Color contours of density ratios ( $N_{p_{\text{Wind}}}/N_{p_{\text{ACE}}}$ ) plotted as a function of ACE bulk and thermal speeds. Ratio values are averaged over bin sizes of 10 (km/sec) and 2 (km/sec) for bulk speed and thermal speed, respectively. Higher resolution is used for the contour plot than in Table A.1.

The majority of Figure A.5 is blue, which indicates the ratio is typically  $N_{\text{Wind}}/N_{\text{ACE}} < 1$ , but the ratio ranges from 0.8 to 1.2. The ratio is greater than one only under a small range of conditions at low bulk speeds of  $\sim 350$  km/sec and thermal speeds from  $\sim 25$ - $45$  km/sec. The ratio is controlled by the thermal and bulk speeds, which suggests a

dependence on detector geometry. Under this conditions Wind densities exceed ACE densities by ~10-15%. At low bulk speeds and the highest thermal speeds the measured Wind densities exceed ACE densities by as much as 20%. Presented in Table 1 is a numerical version of Figure A.5 with lower bin resolutions of bulk speed and thermal

ACE solar wind thermal speed (km/s)	100-110							0.93 ±0.04	0.99 ±0.10	0.93 ±0.12	1.09 ±0.12	1.18 ±0.13
	90-100						0.97 ±0.04	1.01 ±0.06	1.03 ±0.10	0.90 ±0.11	1.34 ±0.16	1.38 ±0.15
	80-90					0.98 ±0.10	0.96 ±0.14	0.94 ±0.12	0.94 ±0.11	1.03 ±0.16	1.32 ±0.19	1.27 ±0.20
	70-80				1.06 ±0.13	0.96 ±0.15	0.93 ±0.15	0.93 ±0.11	0.97 ±0.20	0.99 ±0.15	1.18 ±0.20	1.16 ±0.24
	60-70			0.94 ±0.12	0.94 ±0.10	0.95 ±0.19	0.93 ±0.13	0.90 ±0.09	0.94 ±0.11	0.98 ±0.16	1.15 ±0.12	1.00 ±0.10
	50-60	1.15 ±0.07	1.24 ±0.16	0.95 ±0.12	0.94 ±0.11	0.98 ±0.16	0.96 ±0.15	0.91 ±0.11	0.95 ±0.12	1.09 ±0.05	1.04 ±0.08	0.90 ±0.12
	40-50	1.26 ±0.11	1.13 ±0.19	1.01 ±0.21	0.94 ±0.16	0.96 ±0.11	0.95 ±0.16	0.91 ±0.15	0.86 ±0.12	0.75 ±0.08	1.09 ±0.09	1.18 ±0.15
	30-40	1.17 ±0.10	1.09 ±0.20	0.97 ±0.11	0.91 ±0.13	0.94 ±0.09	0.92 ±0.15	0.96 ±0.18	0.90 ±0.17			1.32 ±0.14
	20-30	1.15 ±0.16	1.02 ±0.16	0.96 ±0.13	0.90 ±0.16	0.97 ±0.14	0.99 ±0.14	0.97 ±0.20	1.19 ±0.29	0.99 ±0.08	1.13 ±0.18	1.22 ±0.23
	10-20	1.03 ±0.20	0.91 ±0.17	0.96 ±0.15	0.95 ±0.20	0.74 ±0.16	1.33 ±0.22	1.35 ±0.23	1.53 ±0.21	1.30 ±0.21	1.19 ±0.14	1.25 ±0.19
	300-350	350-400	400-450	450-500	500-550	550-600	600-650	650-700	700-750	750-800	800-850	

ACE solar wind bulk speed (km/s)

Table A.1: Numerical values of density ratios ( $N_{p_{\text{Wind}}}/N_{p_{\text{ACE}}}$ ). The bulk speed is binned in increments of 50 km/sec, and the thermal speed is binned in increments of 10 km/sec.

speed for brevity. The average density ratios and standard deviations have been computed for bin sizes of 50 and 10 km/sec for the bulk and thermal speeds respectively. The ratio values range from 0.74 to 1.53. There are 50 bins where ACE measures a higher density compared to 37 bins where Wind density measurements are higher, and average ratio for all the bins is 1.06. Based on the quantitative and graphical representation of the comparative number density an adjustment to density observations of  $\pm 10\%$  is an ample assessment of error, which is applied to dynamic pressure observations throughout the thesis.

Because Wind and ACE are not aligned with the solar wind direction the same plasma parcel is generally not seen at the ACE and Wind spacecraft. *Paularena et al.* [1998] investigated the effects of spacecraft separation on the flux correlation in the radial direction, as well as perpendicular to the Earth-sun line, and found no dependence for X and Y separations up to distances of 220 and 80  $R_E$  respectively. The comparative data set for Wind and ACE was binned according to spacecraft separation to determine if there was any spatial variation in the density ratio. Illustrated in Figure A.6 is a cartoon of how the spacecraft separations were binned in GSM coordinates along two cylindrical dimensions. The X-separation of the spacecraft was binned in increments of 50  $R_E$  except for when the spacecraft were 50  $R_E$  apart in which case spatial bins of 25  $R_E$  are used. Thus the spatial bin sizes are as follows: 0-25  $R_E$ , 25-50  $R_E$ , 50-100  $R_E$ , 100-150  $R_E$ , 150-200  $R_E$ , and 200+  $R_E$ . The Y-Z separation was split into two groups where  $(Y^2 + Z^2)^{1/2}$  was either greater than or less than 25  $R_E$ . Shown in Figure A.7 are the plots of density ratios as a function of solar wind bulk and thermal speeds binned according to the

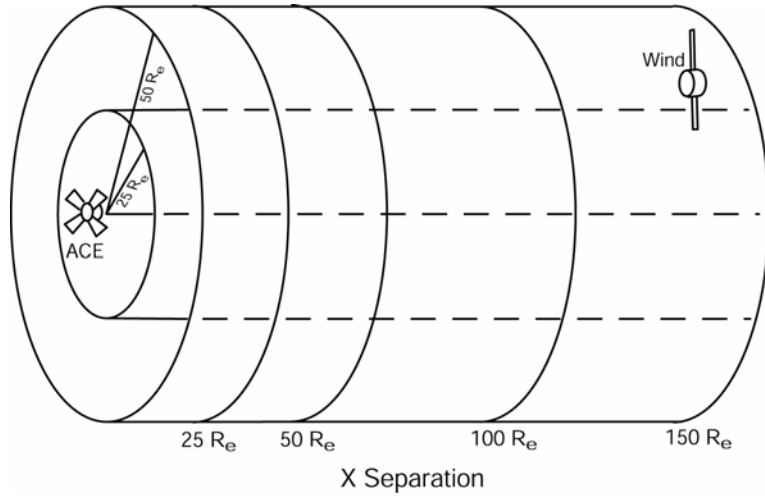


Figure A.6: Illustration of the spacecraft separation used for determining the binning used in two cylindrical dimensions.

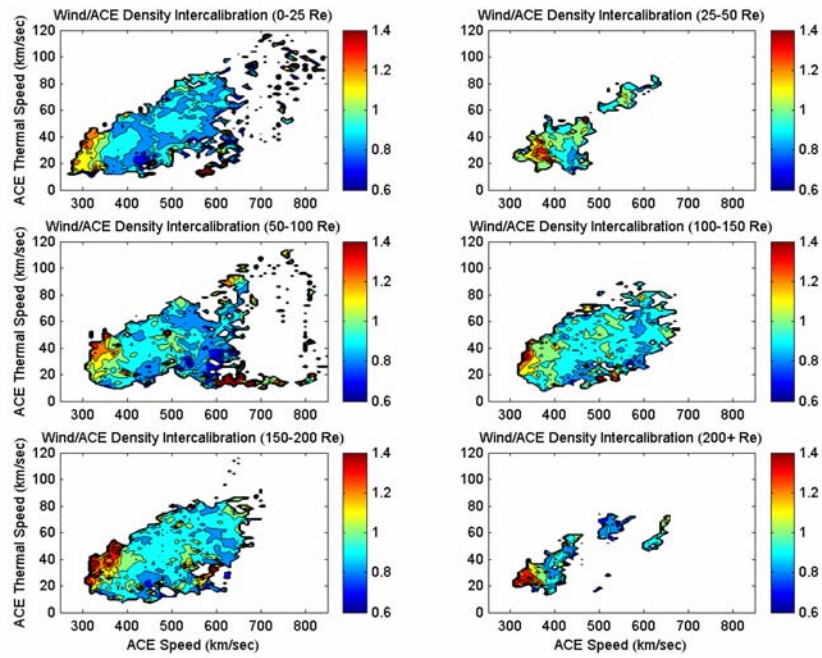


Figure A.7: Color contours of density ratios ( $N_{p_{Wind}}/N_{p_{ACE}}$ ) plotted as a function of ACE bulk speed and thermal speed. Plots are binned according to the X-separation of the ACE and Wind spacecraft, and are labeled respectively.

X-separation of the spacecraft. The same general trend as seen in Figure A.5 is also present for each of the spatial bins. However, there is a lower count rate in each bin, and the ratio value span from 0.6 to 1.4. The plots which take the Y-Z separation into account are not pictured, but they also exhibit the same general trend. These results are not surprising because differences in density measurements should be a function of bulk speed and thermal speed, not spacecraft separation.

#### **A.4 Conclusion**

A comparative data set of plasma parcels measured simultaneously by the Wind and ACE spacecraft is examined for differences in solar wind speed, number density and thermal speed. There is generally good agreement throughout the period from January 1998 to April 2001, but the density ratios depend on the bulk and thermal velocities and are only close to unity when averaged over the entire data set. The analysis does not indicate which spacecraft generates the more accurate data set, nor does it reveal the cause of variations in the density ratio. The plots presented allow one to make a consistently calibrated data set, but not an absolutely calibrated data set. It cannot be determined which spacecraft is more accurate, or if both are inaccurate, but since the spacecraft agree within roughly 10% this is the amount of error associated with density measurements presented throughout the thesis.

## A.5 References

- Coplan, M. A, F. Ipavich, J. King, K. W. Ogilvie, D. A. Roberts, and A. J. Lazarus, Correlation of solar wind parameters between SOHO and Wind, *J. Geophys. Res.*, 18,615-18,624, 2001.
- Fowler, G. J. and C. T. Russell, Geomagnetic field response along the Polar orbit to rapid changes in the solar wind dynamic pressure, *J. Geophys. Res.*, 106, 18,943-18,956, 2001.
- Jurac, S. and J. D. Richardson, The dependence of plasma and magnetic field correlations in the solar wind on geomagnetic activity, *J. Geophys. Res.*, 106, 29,195-29,205, 2001.
- Maksimovic, M., J. L. Bougeret, C. Perche, J. T. Steinberg, A. J. Lazarus, A. F. Vinas, and R. J. Fitzenreiter, Solar wind density intercomparisons on the Wind spacecraft using WAVES and SWE experiments, *Geophys. Res. Lett.*, 25, 1265-1268, 1998.
- McComas, D. J., S. J. Bame, P. Barber, W. C. Feldman, J. L. Phillips, and P. Riley, Solar wind electron, proton, alpha monitor (SWEPAM) on the Advanced Composition Explorer, *Space Sci. Rev.*, 86, 563, 1998.
- Mead, G. D. and D. B. Beard, Shape of the geomagnetic field solar wind boundary, *J. Geophys. Res.*, 69, 1169-1179, 1964.
- Ogilvie, K. W., D. J. Chornay, R. J. Fritzenreiter, F. Hunsaker, J. Keller, J. Lobell, G. Miller, J. D. Scudder, E. C. Sittler Jr., R. B. Torbert, D. Bodet, G. Needell, A. J. Lazarus, J. T. Steinberg, J. H. Tappan, A. Mavretic, and E. Gergin, SWE, a comprehensive plasma instrument for the Wind spacecraft, *Space Science Reviews*, 71, 55-77, 1995.
- Paularena, K. I., G. N. Zastenker, A. J. Lazarus, and P. A. Dalin, Solar wind plasma correlations between IMP 8, Interball-1 and Wind, *J. Geophys. Res.*, 103, 14,601-14,617, 1998.
- Petrinec, S. M. and C. T. Russell, Intercalibration of solar wind instruments during the international magnetospheric study, *J. Geophys. Res.*, 98, 18,963-18,970, 1993.
- Richardson, J. D., F. Dashevskiy, and K. I. Paularena, Solar wind plasma correlations between L1 and Earth, *J. Geophys. Res.*, 103, 14,619-14,629, 1998.
- Russell, C. T. and S. M. Petrinec, On the relative intercalibration of solar wind instruments on IMP-8 and ISEE-3, *Geophys. Res. Lett.*, 19, 961-963, 1992.
- Russell, C. T. and S. M. Petrinec, On the relative intercalibration of solar wind detectors, in *Solar Terrestrial Predictions IV, Vol. 2*, ed. J. Hruska, M. A. Shea, D. F. Smart and G. Heckman, NOAA, ERL, Boulder, Co., 1993.

Sotirelis, T., The shape and field of the magnetopause as determined from pressure balance, *J. Geophys. Res.*, 101, 15,255-15,264,1996.

Sotirelis, T. and C.-I. Meng, Magnetopause from pressure balance, *J. Geophys. Res.*, 104, 6,889-6,898, 1999.

**Appendix 2:**  
**Polar and Wind Data**

Polar spacecraft: Magnetic Field Experiment (MFE)

Date of SI Event	SI onset (UT)	GSM			Bx - GSM (nT)			By - GSM (nT)			Bz - GSM (nT)			BT - GSM (nT)		
		X	Y	Z	Before	After	Change									
4/2/1996	1025	-4.17	0.56	7.23	3.98	7.42	3.44	-6.92	-7.01	-0.09	2.31	2.08	-0.23	2.42	5.52	3.10
4/8/1996	0302	-1.15	-0.50	8.76	4.65	12.31	7.66	-1.66	1.37	3.03	4.55	3.84	-0.71	-2.33	2.94	5.27
6/18/1996	2321	1.12	2.75	7.65	21.64	39.44	17.80	-0.99	-2.49	-1.50	-11.80	-11.74	0.06	17.25	25.35	8.10
7/28/1996	1306	3.02	5.43	3.62	4.58	21.94	17.36	2.08	-3.39	-5.47	13.09	25.03	11.94	-2.85	4.44	7.29
8/22/1996	1318	1.77	2.45	-1.21	3.63	6.59	2.96	-3.98	-3.46	0.52	9.86	15.08	5.22	8.95	7.91	-1.04
9/28/1996	1828	4.44	0.95	4.54	4.45	21.24	16.79	1.79	-4.90	-6.69	-7.56	21.03	28.59	-0.51	-30.03	-29.52
11/11/1996	1527	0.87	-1.44	7.98	4.81	22.17	17.36	0.02	2.63	2.61	9.20	20.73	11.53	-7.85	-18.31	-10.46
11/13/1996	1300	-4.39	1.45	5.67	8.72	21.09	12.37	1.60	-1.38	-2.98	-0.39	0.00	0.39	6.76	16.78	10.02
1/10/1997	0104	-3.44	-3.88	6.84	0.94	11.45	10.51	-1.92	-1.82	0.10	-2.69	4.38	7.07	1.07	1.90	0.83
3/5/1997	1345	-3.00	-2.07	0.73	0.68	0.54	-0.14	-2.10	2.90	5.00	4.52	14.26	9.74	1.31	11.81	10.50
3/20/1997	2045	-3.66	-2.06	5.75	2.49	10.57	8.08	-5.70	-5.27	0.43	3.74	5.34	1.60	-1.92	4.45	6.37
3/23/1997	0903	3.54	2.36	4.40	0.45	5.45	5.00	-2.31	-0.26	2.05	-0.20	4.33	4.53	0.93	-5.66	-6.59
5/1/1997	1245	3.42	1.60	7.92	13.13	40.68	27.55	-9.25	-6.89	2.36	-12.90	-23.25	-10.35	14.96	31.10	16.14
5/15/1997	0159	-1.60	1.52	5.83	21.07	55.38	34.31	1.30	6.35	5.05	4.20	14.68	10.48	7.60	23.02	15.42
5/20/1997	0600	-1.41	2.84	5.14	5.75	24.79	19.04	1.03	1.80	0.77	-3.97	0.43	4.40	4.62	12.24	7.62
9/2/1997	2259	-2.16	-3.99	5.54	-0.41	13.16	13.57	-5.09	-2.34	2.75	6.12	11.19	5.07	-6.35	0.85	7.20
10/1/1997	0058	-3.45	-2.35	7.18	12.88	41.63	28.75	-5.97	-3.36	2.61	1.27	7.26	5.99	5.92	24.35	18.43
10/10/1997	1613	-3.28	-0.61	8.10	19.31	36.74	17.43	-3.22	-5.20	-1.98	-4.01	-7.55	-3.54	16.57	31.52	14.95
11/1/1997	0636	-1.58	0.17	8.36	23.93	44.46	20.53	1.36	0.69	-0.67	-4.42	10.45	14.87	12.65	8.42	-4.23
11/9/1997	1041	-1.34	0.53	8.03	-2.92	21.51	24.43	0.95	-2.23	-3.18	-1.88	18.97	20.85	0.97	-11.21	-12.18
11/9/1997	2255	-5.38	-0.32	6.53	16.19	37.97	21.78	0.25	0.24	-0.01	-9.08	-12.46	-3.38	18.51	38.24	19.73
11/22/1997	0950	-5.19	3.14	2.21	16.42	42.55	26.13	-3.91	1.57	5.48	-18.40	-13.42	4.98	13.47	35.32	21.85
12/10/1997	0526	-4.96	3.64	4.61	-0.17	11.45	11.62	2.53	0.52	-2.01	2.90	10.58	7.68	-2.79	3.97	6.76
1/6/1998	1416	-2.88	5.12	4.86	-2.94	18.84	21.78	-0.40	-4.00	-3.60	-5.63	4.20	9.83	1.26	11.05	9.79
2/18/1998	0843	2.47	3.00	0.40	-1.31	4.75	6.06	-10.49	-2.38	8.11	-31.48	-20.46	11.02	-32.91	-21.20	11.71
3/4/1998	1156	3.59	3.75	3.60	0.36	5.93	5.57	-2.43	-1.62	0.81	-5.98	0.93	6.91	0.81	-2.75	-3.56
4/23/1998	1825	2.50	-0.54	-1.62	4.56	14.00	9.44	2.42	-1.76	-4.18	7.57	38.47	30.90	5.18	39.62	34.44
4/30/1998	0930	-2.00	0.46	-0.56	-0.20	-15.07	-14.87	-3.92	-7.27	-3.35	14.76	28.36	13.60	13.28	15.43	2.15
5/8/1998	0951	0.99	2.38	6.75	17.75	44.20	26.45	-1.70	-16.03	-14.33	-16.46	-16.94	-0.48	17.24	31.65	14.41
6/17/1998	2137	4.01	-5.48	2.40	-0.28	4.14	4.42	0.92	2.65	1.73	1.99	6.96	4.97	1.48	3.17	1.69
6/22/1998	1558	3.99	-0.02	7.43	8.94	16.31	7.37	-6.06	-6.53	-0.47	-18.46	-22.04	-3.58	18.07	21.83	3.76
8/6/1998	0736	2.86	1.11	6.90	37.21	73.37	36.16	-4.85	-1.77	3.08	-33.00	-47.54	-14.54	26.86	38.43	11.57
8/10/1998	0047	2.77	-0.88	6.91	-8.39	23.22	31.61	-4.05	6.86	10.91	-7.01	-6.66	0.35	8.05	0.81	-7.24
8/19/1998	1846	2.87	1.13	4.54	13.32	40.50	27.18	0.90	0.95	0.05	-14.09	-13.99	0.10	4.59	-13.18	-17.77
9/24/1998	2345	-2.38	-2.72	8.13	31.75	101.63	69.88	-3.90	8.17	12.07	-15.65	0.99	16.64	29.43	77.22	47.79
10/2/1998	0726	-4.98	-0.28	7.39	6.27	34.22	27.95	-1.29	-9.76	-8.47	-3.19	1.41	4.60	6.84	27.52	20.68
10/6/1998	1633	-6.08	-0.85	5.38	-4.01	2.02	6.03	-2.19	-1.44	0.75	7.57	6.80	-0.77	-5.68	0.01	5.69
10/18/1998	1951	-3.20	-1.49	7.83	3.82	27.75	23.93	-1.76	1.53	3.29	-3.02	3.01	6.03	4.38	16.64	12.26
11/7/1998	0815	0.23	-0.32	5.42	11.95	24.06	12.11	6.33	17.13	10.80	-15.85	2.31	18.16	14.49	-6.12	-20.61
11/30/1998	0508	-5.25	2.04	6.89	7.94	22.65	14.71	5.51	8.59	3.08	-3.03	-1.04	1.99	6.08	15.23	9.15
1/13/1999	1054	0.90	0.04	-1.76	-32.60	-46.34	-13.74	-27.49	42.85	70.34	-42.47	-16.65	25.82	24.68	6.85	-17.83
2/17/1999	0710	-2.32	0.11	5.56	18.32	33.02	14.70	0.07	3.68	3.61	0.94	9.22	8.28	7.38	9.62	2.24
2/18/1999	0247	-2.39	-1.84	1.74	10.67	11.79	1.12	-4.41	-1.31	3.10	-9.29	4.82	14.11	6.80	7.87	1.07
3/10/1999	0131	0.10	-0.18	7.73	25.54	48.76	23.22	-4.25	-6.64	-2.39	-19.97	-19.05	0.92	22.65	28.70	6.05
5/18/1999	0055	4.71	-3.59	-0.77	2.62	11.03	8.41	1.35	3.36	2.01	11.86	47.72	35.86	12.15	47.58	35.43
7/12/1999	0218	2.75	-0.30	5.34	23.52	53.05	29.53	-7.80	-16.60	-8.80	-11.18	-9.49	1.69	-0.93	-13.52	-12.59
8/23/1999	1224	-1.42	-1.99	8.62	14.74	25.29	10.55	-4.27	-3.66	0.61	-15.32	-17.44	-2.12	19.37	27.55	8.18
9/22/1999	1223	-1.95	0.12	7.47	29.87	65.93	36.06	-12.65	-16.57	-3.92	-9.21	-16.58	-7.37	25.61	53.07	27.46
10/28/1999	1216	-2.92	0.95	6.22	6.59	14.05	7.46	1.18	-1.26	-2.44	-6.99	-4.49	2.50	9.19	11.75	2.56
1/27/2000	1457	2.28	6.89	2.92	2.71	5.44	2.73	5.69	16.70	11.01	24.13	50.68	26.55	12.46	24.41	11.95
2/11/2000	2353	-0.43	0.90	7.28	20.76	87.05	66.29	-3.87	9.65	13.52	-16.97	-10.37	6.60	19.64	35.48	15.84
6/4/2000	1501	2.17	0.68	4.17	-14.28	17.60	31.88	11.43	8.97	-2.46	-2.77	-7.34	-4.57	6.99	-3.35	-10.34
6/8/2000	0911	2.50	0.70	4.38	9.24	51.56	42.32	6.74	26.83	20.09	-11.86	47.42	59.28	4.15	-71.91	-76.06
6/23/2000	1304	-0.75	0.77	-1.27	9.31	-32.27	-41.58	21.09	50.85	29.76	59.07	20.44	-38.63	10.50	-9.58	-20.08
8/10/2000	0501	-4.48	-5.96	3.17	-2.21	8.70	10.91	15.50	20.19	4.69	-11.79	-7.89	3.90	7.80	19.84	12.04
9/4/2000	1333	1.57	0.61	2.56	3.63	6.81	3.18	2.74	10.64	7.90	-8.20	-8.07	0.13	5.40	-6.68	-12.08
9/6/2000	1702	-1.92	-1.84	6.41	16.91	54.06	37.15	-6.68	-3.83	2.85	8.39	16.05	7.66	3.27	22.77	19.50
10/3/2000	0055	-5.40	-1.42	5.85	22.63	38.01	15.38	2.67	3.81	1.14	-12.72	-10.33	2.39	25.92	38.41	12.49
10/5/2000	0327	-8.48	-0.21	4.12	22.85	46.80	23.95	3.64	2.82	-0.82	-0.40	-5.17	-4.77	22.98	47.17	24.19
10/12/2000	2229	-4.50	-0.98	5.53	-0.17	17.11	17.28	0.48	1.83	1.35	-2.16	0.70	2.86	1.03	13.88	12.85
11/10/2000	0629	-4.19	3.64	-2.66	-33.11	-60.48	-27.37	32.32	23.94	-8.38	-43.77	-14.13	29.64	22.37	48.93	26.56
11/28/2000	0532	-3.23	1.34	4.35	36.31	52.36	16.05	0.74	1.81	1.07	-10.07	-5.20	4.87	30.41	36.56	6.15

Observations listed in red were also examined *in situ* with GOES 8 & GOES 9  
 Observations listed in blue were also examined *in situ* with GOES 8  
 Observations listed in green were also examined *in situ* with GOES 8 & GOES 10  
 Observations listed in black were also examined *in situ* with GOES 8 & GOES 9

Wind spacecraft: Solar Wind Experiment (SWE)

Date of Compression	Time (UT)	Wind Location (GSM)			X Velocity (km/sec)			Y Velocity (km/sec)			Z Velocity (km/sec)			SW Velocity			Particle Density (cm <sup>-3</sup> )			Dynamic Pressure (nPa)			Thermal Velocity (km/sec)		
		X	Y	Z	Up	Down	Change	Up	Down	Change	Up	Down	Change	Up	Down	Change	Up	Down	Change	Up	Down	Change	Up	Down	Change
4/21/1996	1007	71.00	-4.26	0.15	-331.15	-10.21	-341.36	-3.05	-3.17	-0.12	2.57	17.36	14.79	331.17	341.82	10.64	12.52	19.27	6.75	2.30	3.77	1.47	19.75	20.95	1.20
4/6/1996	0241	82.97	23.68	9.80	-282.30	-10.68	-292.98	-19.87	-39.30	-19.43	-16.96	0.51	17.49	283.51	295.60	12.10	10.64	11.48	11.48	2.16	4.03	1.87	16.73	19.17	2.44
6/18/1996	2235	205.18	21.99	-9.84	-397.89	-428.23	-30.34	-21.23	-20.01	1.22	-17.12	-15.31	1.81	396.82	428.97	30.15	10.64	15.63	4.99	2.62	4.82	10.99	27.08	32.41	5.33
7/28/1996	1214	179.23	13.47	-10.30	-306.55	-335.26	-28.71	-12.01	-16.25	-4.84	10.99	8.82	-1.91	306.98	335.78	28.79	19.54	12.39	3.93	0.84	1.97	1.03	40.33	21.26	-4.07
8/22/1996	1306	50.26	-17.52	5.55	-358.90	-381.57	-32.67	-5.41	-15.24	-8.83	16.74	9.08	-7.92	359.33	381.98	22.65	4.36	8.05	3.69	3.08	1.94	1.37	17.19	31.26	14.07
9/28/1996	1818	78.95	-18.56	3.61	-469.23	-491.22	-21.99	-22.73	-8.29	14.56	5.12	-9.44	470.01	491.32	21.31	3.24	10.75	7.51	2.40	3.34	3.14	1.40	37.36	23.38	-13.98
11/11/1996	1511	65.31	18.76	0.06	-346.72	-363.02	-16.30	-5.69	-4.48	1.21	6.46	3.94	-2.52	346.83	363.07	16.24	11.16	20.99	9.83	2.25	4.34	2.38	18.18	19.91	1.73
11/13/1996	1249	39.84	-24.44	-6.50	-371.48	-388.25	-16.03	-9.31	15.46	6.15	6.01	14.76	8.75	371.59	388.84	17.25	10.24	25.74	15.50	1.55	4.31	4.15	25.57	25.91	0.34
11/10/1997	0051	85.01	-55.12	-22.44	-377.48	-411.55	-34.07	-8.19	-11.42	-3.23	13.87	-18.79	-32.66	377.82	412.14	34.31	6.50	15.42	8.92	1.55	4.36	2.91	23.14	34.21	11.07
3/20/1997	1254	222.15	20.35	-0.82	-318.28	-358.16	-39.88	-7.87	-20.19	-12.32	-13.32	-8.80	4.52	318.66	358.84	40.18	8.53	20.27	11.74	1.45	4.36	2.91	23.14	34.21	11.07
3/20/1997	1941	228.29	12.52	16.10	-303.97	-319.10	-15.13	-5.25	-18.99	-13.74	-1.10	9.20	13.30	304.04	319.80	15.75	18.50	32.56	14.06	2.86	5.57	2.71	15.79	19.06	3.27
3/23/1997	0822	228.83	14.57	13.84	-355.54	-366.73	-11.19	0.84	-14.23	-15.07	-14.51	11.48	25.99	355.64	367.19	11.35	5.18	9.06	3.84	1.10	2.04	0.94	26.79	33.13	6.34
5/15/1997	1202	214.98	-4.86	23.41	-337.91	-360.29	-22.38	7.90	-12.20	-20.10	-4.44	28.66	33.10	338.03	361.63	23.60	11.82	24.66	12.84	2.26	5.40	3.14	27.19	36.46	9.27
5/20/1997	0510	170.83	-3.76	17.48	-318.13	-389.74	-71.61	-6.22	-32.56	-23.34	-26.81	-55.27	-26.86	319.39	394.76	75.37	19.10	42.10	23.00	3.26	10.97	7.71	23.39	32.30	8.91
9/21/1997	2237	72.67	32.54	-5.05	-299.76	-327.73	-27.97	-0.72	-13.05	-12.33	-6.43	-0.20	-13.84	299.83	328.62	28.79	9.22	22.03	12.81	1.39	3.99	2.60	20.70	37.91	17.21
10/10/1997	0056	-10.08	-20.92	2.08	-303.01	-347.89	-30.89	-10.66	-11.51	9.15	15.35	-16.80	-34.15	322.27	461.09	138.82	20.05	34.82	14.77	3.48	12.41	8.53	89.43	41.73	-47.70
10/10/1997	0614	76.81	-32.04	14.32	-408.16	-438.16	-29.96	1.60	5.62	4.02	8.06	19.09	11.03	408.26	438.61	30.35	12.56	21.11	8.55	3.90	6.90	3.30	17.36	21.65	4.49
11/10/1997	0053	140.81	-28.97	37.33	-362.65	-377.38	-14.74	-7.06	0.23	7.31	0.24	-44.72	-44.96	352.72	380.03	17.76	7.76	15.73	7.47	1.71	3.68	1.97	17.22	21.06	3.84
11/20/1997	2222	160.90	-1.19	34.45	-388.02	-395.36	-27.56	-5.33	0.58	-4.46	8.46	12.94	366.09	395.67	27.58	10.61	22.79	11.38	10.61	2.45	5.37	3.52	21.30	28.04	6.74
12/20/1997	0932	205.87	1.16	31.45	-346.61	-333.01	-86.00	-14.62	-33.95	-10.63	-21.16	16.45	-20.26	341.36	354.43	71.69	11.55	27.66	16.13	1.58	2.82	1.54	23.89	38.48	14.59
1/15/1998	1336	205.87	20.27	5.23	-305.73	-368.44	-62.71	-3.20	32.38	35.88	13.26	-14.52	-12.24	308.32	354.43	64.11	11.55	27.66	16.13	1.58	2.82	1.54	23.89	38.48	14.59
2/16/1998	0748	234.89	-2.46	-33.03	-375.55	-405.29	-29.74	-16.00	-30.64	-31.20	-31.20	-27.22	3.98	377.16	407.31	30.17	17.63	26.49	7.85	4.30	7.09	2.89	28.81	33.82	5.01
3/4/1998	1191	234.89	-2.46	-33.03	-375.55	-405.29	-29.74	-16.00	-30.64	-31.20	-31.20	-27.22	3.98	377.16	407.31	30.17	17.63	26.49	7.85	4.30	7.09	2.89	28.81	33.82	5.01
4/23/1998	1727	220.17	-13.32	18.61	-323.94	-368.42	-44.48	-16.10	-35.50	-19.40	-6.09	-21.25	-15.16	324.36	370.36	45.98	14.40	38.11	23.71	2.53	8.75	6.22	27.45	34.69	7.24
4/30/1998	0841	211.16	8.58	29.77	-316.62	-368.42	-47.61	-5.81	-40.97	-55.16	-13.92	11.51	25.43	316.98	368.48	52.50	11.93	38.98	27.05	2.00	8.90	6.90	27.45	34.69	7.24
5/9/1998	0920	211.16	8.58	29.77	-316.62	-368.42	-47.61	-5.81	-40.97	-55.16	-13.92	11.51	25.43	316.98	368.48	52.50	11.93	38.98	27.05	2.00	8.90	6.90	27.45	34.69	7.24
6/17/1998	2111	126.12	57.96	25.92	-315.35	-328.10	-12.75	41.40	-42.97	1.57	-6.05	2.97	9.02	551.25	621.28	70.03	5.37	8.33	2.86	2.75	5.38	2.63	86.00	102.34	16.34
6/22/1998	1535	95.23	66.44	2.77	-391.90	-401.36	-9.45	-7.94	-11.59	-3.65	3.90	6.31	2.41	392.00	401.57	9.57	6.80	7.47	1.67	1.49	2.02	0.53	32.16	35.94	3.78
8/6/1998	0715	92.11	6.86	-6.14	-372.08	-425.01	-52.92	-19.05	-6.75	12.30	5.15	23.21	18.06	372.61	425.70	53.08	10.57	20.50	9.93	2.45	6.20	3.75	17.32	23.59	6.27
8/10/1998	0830	77.75	19.12	-4.79	-396.51	-446.07	-49.56	-8.20	-40.05	-45.25	7.85	52.37	44.52	396.62	450.92	54.29	4.54	9.94	1.40	1.20	2.02	0.82	18.38	26.61	7.79
8/19/1998	1840	53.88	-36.63	6.34	-274.61	-315.46	-40.85	-8.40	-32.68	-24.28	1.66	9.47	7.81	274.74	317.29	42.55	8.34	18.72	10.38	1.05	3.15	2.10	18.82	26.61	7.79
9/24/1998	2318	183.44	13.02	-8.98	-434.91	-613.30	-178.39	21.90	-66.74	-88.64	19.44	-52.58	-72.02	435.89	619.16	183.26	8.00	21.32	13.32	2.54	13.71	11.17	55.48	118.29	62.81
10/2/1998	0705	173.25	14.43	-10.72	-521.63	-695.63	-174.00	24.06	-34.71	10.65	15.24	-39.48	-54.72	522.41	697.61	30.14	6.02	10.71	4.69	1.15	2.43	1.28	59.29	144.10	84.81
10/6/1998	1544	162.42	17.83	-8.22	-337.45	-386.61	-29.16	-18.29	-19.98	-1.69	14.37	30.21	15.84	338.25	386.39	30.14	6.02	10.71	4.69	1.15	2.43	1.28	59.29	144.10	84.81
10/8/1998	1928	101.14	32.30	-1.94	-328.41	-346.68	-206.25	11.68	6.22	-5.46	-9.56	-56.17	-46.81	328.76	357.64	208.88	17.23	29.68	12.45	3.11	5.72	2.47	20.36	28.08	7.72
11/20/1998	0506	80.82	-26.30	23.84	-441.74	-456.86	-151.12	-8.62	-21.87	-13.25	2.51	-47.54	-50.05	441.83	459.85	18.02	5.47	16.36	8.55	1.56	4.03	3.05	41.54	57.15	15.61
11/31/1999	1046	26.03	-60.06	-19.27	-343.42	-406.28	-59.60	-32.62	-58.27	-25.65	10.03	26.36	16.33	344.30	390.21	45.90	10.20	22.44	12.24	2.02	5.71	3.69	25.68	32.64	6.96
2/17/1999	0245	-13.01	-59.45	-37.66	-459.15	-503.24	-44.09	-19.72	-23.66	-3.94	-6.43	-13.44	-7.01	459.62	503.98	44.36	5.94	10.66	4.72	2.10	4.53	2.43	23.45	29.11	5.66
3/10/1999	0132	-8.23	-17.30	-36.82	-410.42	-460.64	-50.22	6.22	-5.21	-11.43	-23.76	-15.03	8.73	385.01	460.91	49.76	7.35	13.00	5.65	0.98	7.54	6.56	33.79	42.44	8.65
5/18/1999	0031	104.61	-25.14	-20.98	-340.80	-403.51	-62.71	-17.76	-34.31	-16.55	5.46	-1.77	-7.23	341.31	404.97	63.66	9.86	28.09	18.23	1.92	7.71	5.79	22.09	27.47	5.38
7/12/1999	0121	201.69	-18.19	3.97	-304.39	-314.66	-10.27	-18.75	0.38	19.13	12.67	-9.98	-22.65	305.23	314.82	9.59	12.96	28.25	15.29	2.02	4.6				

Wind spacecraft: Magnetic Field Instrument (MFI)																
Date Event	Time Shock	Wind Location (GSM)			X Magnetic Field (nT)			Y Magnetic Field (nT)			Z Magnetic Field (nT)			Total Magnetic Field Magnitude(nT)		
		X	Y	Z	Up	Down	dBx	Up	Down	dBz	Up	Down	dBz	Up	Down	dBT
4/2/1996	1007	71.00	-4.26	0.15	2.64	4.61	1.97	0.09	-0.88	-0.97	0.52	1.24	0.72	2.70	4.89	2.19
4/8/1996	0241	82.97	23.68	9.80	-3.87	-6.42	-2.55	2.82	5.16	2.34	3.12	3.51	0.39	5.75	8.96	3.21
6/18/1996	2235	205.18	21.99	-9.84	-2.04	-1.12	0.92	-6.17	-9.02	-2.85	-3.39	-5.21	-1.82	7.40	10.72	3.32
7/28/1996	1214	179.23	13.47	-10.30	-1.71	0.50	2.21	1.33	1.00	-0.33	0.21	-4.48	-4.69	2.20	4.97	2.77
8/22/1996	1306	50.26	-17.92	5.55	-2.89	-2.60	0.29	0.69	3.42	2.73	-1.55	-2.84	-1.29	3.38	5.23	1.85
9/28/1996	1818	78.95	-18.56	3.61	-2.14	-0.11	2.03	3.15	-1.25	-4.40	0.02	0.43	0.41	3.90	1.91	-1.99
11/11/1996	1511	65.31	18.76	0.06	-1.13	-1.22	-0.09	0.78	1.49	0.71	1.19	-0.19	-1.38	1.82	2.41	0.59
11/13/1996	1249	39.84	24.67	-6.50	0.97	-1.15	-2.12	2.38	1.55	-0.83	-1.93	-1.53	0.40	3.48	2.77	-0.71
1/10/1997	0051	85.01	-55.12	-22.44	-2.16	-4.77	-2.61	0.54	1.59	1.05	0.44	4.87	4.43	2.31	8.06	5.75
3/5/1997	1254	222.15	20.35	-0.82	3.86	3.49	-0.37	-1.15	-3.47	-2.32	1.93	4.38	2.45	4.51	6.71	2.20
3/20/1997	1941	228.29	12.52	16.10	0.80	0.94	0.14	1.56	2.63	1.07	2.28	3.13	0.85	2.88	4.21	1.33
3/23/1997	0822	228.83	14.57	13.84	0.74	2.32	1.58	-1.51	-2.82	-1.31	-1.23	-0.65	0.58	2.20	3.84	1.64
5/1/1997	1202	214.99	-4.86	23.41	1.63	3.11	1.48	0.32	-3.07	-3.39	-0.28	-0.72	-0.44	2.04	5.13	3.09
5/15/1997	0114	190.83	-3.76	17.48	-2.74	-6.95	-4.21	6.68	16.38	9.70	0.50	1.73	1.23	7.26	18.81	11.55
5/20/1997	0510	175.83	4.95	14.98	-2.15	-3.87	-1.72	1.17	1.85	0.68	-1.26	-0.24	1.02	3.35	4.67	1.32
9/2/1997	2237	72.67	32.54	-5.05	-1.96	-3.40	-1.44	-0.17	2.39	2.56	3.06	5.67	2.61	3.98	7.61	3.63
10/1/1997	0056	-10.08	-20.92	2.08	-5.36	0.94	6.30	-2.46	-6.09	-3.63	2.07	-0.92	-2.99	6.39	8.50	2.11
10/10/1997	1557	76.81	-32.04	14.32												
11/1/1997	0614	93.62	-52.89	32.65	-2.07	-4.45	-2.38	5.12	6.67	1.55	1.72	4.66	2.94	5.80	9.31	3.51
11/9/1997	1003	140.81	-29.57	37.93	-3.64	-7.24	-3.60	1.24	0.15	-1.09	0.54	2.62	2.08	3.96	7.89	3.93
11/9/1997	2222	142.97	-40.59	24.26	2.41	0.38	-2.03	0.18	-0.79	-0.97	-4.16	-7.63	-3.47	4.96	8.13	3.17
11/22/1997	0912	180.90	-5.19	32.44	-1.33	-4.79	-3.46	5.31	10.11	4.80	-0.79	-6.45	-5.66	5.75	15.22	9.47
12/10/1997	0432	206.80	11.86	21.62	1.69	2.30	0.61	-6.19	-14.79	-8.60	0.21	-5.05	-5.26	6.81	16.00	9.19
1/6/1998	1328	227.07	20.27	-5.23	-0.62	0.94	1.56	-6.46	-3.06	3.40	0.40	-6.20	-6.60	6.61	10.86	4.25
2/18/1998	0748	235.89	-2.46	-33.03	8.56	7.60	-0.96	-12.70	-19.46	-6.76	-2.71	-3.09	-0.38	15.59	21.21	5.62
3/4/1998	1101	234.66	-11.80	-30.47	2.14	1.84	-0.30	-0.23	0.35	0.58	-2.04	-5.09	-3.05	3.07	5.77	2.70
4/23/1998	1727	220.17	-13.32	16.61	-3.09	-3.94	-0.85	2.58	6.27	3.69	0.96	3.43	2.47	4.21	8.32	4.11
4/30/1998	0841	216.92	-2.02	25.04	0.74	3.49	2.75	0.23	-2.10	-2.33	1.08	1.12	0.04	1.59	4.90	3.31
5/8/1998	0920	211.16	8.58	29.77	1.87	1.18	-0.69	-4.37	-9.39	-5.02	1.25	3.27	2.02	7.17	11.77	4.60
6/17/1998	2111	126.12	57.96	25.92	-0.82	-1.73	-0.91	2.80	3.40	0.60	2.86	3.72	0.86	4.15	5.38	1.23
6/22/1998	1535	95.23	66.44	2.77	2.61	2.60	-0.01	-4.73	-5.93	-1.20	-0.08	-1.81	-1.73	5.50	7.40	1.90
8/6/1998	0715	92.11	6.86	-6.14	-0.60	-2.20	-1.60	5.52	9.33	3.81	-8.81	-15.34	-6.53	10.49	18.16	7.67
8/10/1998	0030	77.75	19.12	-4.79	-4.38	-7.81	-3.43	1.59	7.20	5.61	0.82	-0.63	-1.45	4.85	10.83	5.98
8/19/1998	1840	53.88	-36.63	6.34	-2.60	-2.76	-0.16	0.00	2.21	2.21	-2.49	-6.91	-4.42	3.74	7.99	4.25
9/24/1998	2318	183.44	13.02	-8.98	-6.44	-15.70	-9.26	13.10	35.11	22.01	0.42	8.23	7.81	14.69	39.76	25.07
10/2/1998	0705	173.25	14.43	-10.72	1.81	-5.47	-7.28	-3.27	-14.89	-11.62	2.12	0.20	-1.92	6.83	16.64	9.81
10/6/1998	1544	162.42	17.83	-8.22	3.21	4.17	0.96	-1.54	-2.23	-0.69	1.98	5.90	3.92	4.12	7.73	3.61
10/18/1998	1928	101.14	32.30	-1.94	4.56	10.37	5.81	-2.11	-1.84	0.27	0.81	-3.82	-4.63	5.10	11.29	6.19
11/7/1998	0758	80.82	15.42	2.10	-3.83	-5.69	-1.86	2.51	7.07	4.56	-0.13	1.66	1.79	6.12	10.71	4.59
11/30/1998	0506	24.03	-26.30	23.84	-3.69	1.20	4.89	-0.36	-5.10	-4.74	-2.60	-7.95	-5.35	4.79	9.77	4.98
1/13/1999	1046	28.68	-60.06	-19.27	1.69	-0.42	-2.11	-3.36	-4.52	-1.16	-3.18	-7.09	-3.91	5.39	9.68	4.29
2/17/1999	0712	-13.01	-59.45	-37.66	-0.78	0.62	1.40	6.72	11.30	4.58	-0.44	-1.46	-1.02	6.91	11.61	4.70
2/18/1999	0245	-9.19	-44.39	-48.81	-4.69	-5.45	-0.76	2.70	12.61	9.91	4.76	13.96	9.20	7.42	20.02	12.60
3/10/1999	0132	-8.23	-17.30	-36.72	-0.49	-2.67	-2.18	-0.34	-3.56	-3.22	-4.15	-6.14	-1.99	4.33	8.87	4.54
5/18/1999	0031	104.61	-25.14	-20.98	-5.18	-5.94	-0.76	2.17	6.13	3.96	0.87	1.87	1.00	5.75	8.89	3.14
7/12/1999	0121	201.69	-18.19	3.97	-2.70	1.00	3.70	-4.09	-4.53	-0.44	-2.97	-8.78	-5.81	5.79	10.45	4.66
8/23/1999	1209	64.32	-17.50	6.14	-4.36	-4.53	-0.17	2.18	1.58	-0.60	-6.43	-10.35	-3.92	8.09	11.51	3.42
9/22/1999	1208	83.21	-6.04	5.53	-3.45	10.81	14.26	-9.74	1.13	10.87	-4.06	8.26	12.32	11.56	16.06	4.50
10/28/1999	1212	28.43	2.95	16.84	-3.47	-1.89	1.58	2.27	3.99	1.72	4.83	7.17	2.34	6.77	9.75	2.98
1/27/2000	1502	-4.05	-48.13	37.20	13.03	14.85	1.82	-1.17	-2.22	-1.05	6.33	14.20	7.87	14.59	20.83	6.24
2/1/2000	2332	131.91	-6.48	6.76	2.43	10.37	7.94	-4.70	-17.11	-12.41	-4.06	-9.62	-5.56	6.73	22.45	15.72
6/4/2000	1449	56.68	-52.05	-7.76	2.92	1.21	-1.71	-2.20	-1.99	0.21	3.02	11.09	8.07	5.04	11.46	6.42
6/8/2000	0904	40.72	-26.63	-2.10	-4.63	-7.28	-2.65	1.43	13.70	12.27	1.87	6.07	4.20	6.94	21.84	14.90
6/23/2000	1257	39.13	-46.83	3.74	5.64	14.16	8.52	-4.73	-8.92	-4.19	-1.53	-4.65	-3.12	8.19	18.51	10.32
8/10/2000	0511	-21.99	-59.68	13.94	-2.26	-6.27	-4.01	4.96	8.46	3.50	-3.72	-2.59	1.13	6.73	11.37	4.64
9/4/2000	1312	19.44	-164.62	87.24	-2.46	-4.40	-1.94	-0.90	-1.35	-0.45	-3.16	-4.98	-1.82	4.28	7.07	2.79
9/6/2000	1702	23.29	-186.36	63.96	-7.13	-11.22	-4.09	5.49	15.89	10.40	0.67	4.28	3.61	9.16	20.17	11.01
10/3/2000	0101	32.79	-244.99	59.02	-2.62	-4.92	-2.30	2.83	7.60	4.77	-3.73	-4.39	-0.66	5.93	10.37	4.44
10/5/2000	0328	32.08	-237.19	81.15	-2.46	-4.23	-1.77	-2.30	-8.68	-6.38	-5.49	-15.65	-10.16	6.48	18.56	12.08
10/12/2000	2232	31.32	-234.97	47.25	-2.06	-1.39	0.67	5.01	13.53	8.52	2.48	10.67	8.19	6.15	17.63	11.48
11/10/2000	0618	83.55	-77.97	37.82	4.53	12.17	7.64	-3.58	-6.10	-2.52	7.98	14.96	6.98	10.79	22.84	12.05
11/28/2000	0527	69.07	109.95	-26.44	4.04	8.08	4.04	2.44	7.48	5.04	-2.72	-5.16	-2.44	5.66	12.76	7.10

Observations listed in red were also examined *in situ* with GOES 8 & GOES 9  
Observations listed in blue were also examined *in situ* with GOES 8  
Observations listed in green were also examined *in situ* with GOES 8 & GOES 10  
Observations listed in black were also examined *in situ* with GOES 8 & GOES 9